ÇUKUROVA UNIVERSITY
INSTITUTE OF NATURAL AND APPLIED SCIENCES

PhD THESIS

Alparslan TOPCU

CHARACTERISATION OF PEM FUEL CELL COLD START PROCESS

DEPARTMENT OF AUTOMOTIVE ENGINEERING

ADANA-2023

ABSTRACT

PhD THESIS

CHARACTERISATION OF PEM FUEL CELL COLD START PROCESS

Alparslan TOPCU

ÇUKUROVA UNIVERSITY
INSTITUTE OF NATURAL AND APPLIED SCIENCES
DEPARTMENT OF AUTOMOTIVE ENGINEERING

Supervisor : Prof. Dr. Kadir AYDIN
Co-Supervisor : Prof. Dr. Selahattin ÇELİK
Year: 2023, Pages: 193
Jury : Prof. Dr. Kadir AYDIN
: Assoc. Prof. Dr. Gökhan TÜCCAR
: Asst. Prof. Dr. Tayfun ÖZGÜR
: Asst. Prof. Dr. Nazım KURTULMUŞ
: Asst. Prof. Dr. Erdi TOSUN

Water droplets formed in PEM fuel cell operating conditions freeze at sub-zero temperatures and cause start-up failure. In this thesis, a quick, effective, and low energy-consuming coolant heating method has been developed by characterizing the cold start process of the PEM fuel cell. The effects of the components in the experimental setup on the cold start performance were investigated in the range of -10 and -30 ℃. The fuel cell and the external heating system were operated simultaneously and a current was drawn from the cell during the tests. Stack temperature was followed from five different symmetrical places and temperature-voltage-current profiles were plotted. In the preliminary tests at -10 ℃, ethanol as the working fluid, double-sided heating type, and full power pump operation were specified as the parameters that provide the quickest heating. The effect of the heater and pump operating durations under the same energy consumption level were compared and no significant difference was noted at this temperature. However, it is found that long pump operation at extreme conditions (-15 and -30℃ range) is essential for a successful cold start process and it provides a more homogeneous and smooth temperature transition. PEM fuel cell was operated successfully in all conditions thanks to the external heating mechanism, and the cell temperature was increased above zero in 20, 40, and 53 seconds, respectively, in cold start tests at -10, -20, and 30 ℃.

Keywords: PEM fuel cell, cold start, assisted, starter technique, experimental.

ÖZ

DOKTORA TEZİ

PEM YAKIT PİLİ SOĞUK ÇALIŞTIRMA PROSESİNİN KARAKTERİZASYONU

Alparslan TOPCU

ÇUKUROVA ÜNİVERSİTESİ
FEN BİLİMLERİ ENSTİTÜSÜ
OTOMOTİV MÜHENDİSLİĞİ ANABİLİM DALI

Danışman : Prof. Dr. Kadir AYDIN
Eş-Danışman : Prof. Dr. Selahattin ÇELİK
Yıl: 2023, Sayfa: 193
Jüri : Prof. Dr. Kadir AYDIN
: Doç. Dr. Gökhan TÜCCAR
: Dr. Öğr. Üyesi Tayfun ÖZGÜR
: Dr. Öğr. Üyesi Nazım KURTULMUŞ
: Dr. Öğr. Üyesi Erdi TOSUN

PEM yakıt pili çalışma koşullarında meydana gelen su partikülleri, sıfırın altındaki sıcaklıklarda donmakta ve başlatma hatasına neden olmaktadır. Bu tez çalışmasında, PEM yakıt pilinin soğuk çalıştırma prosesi karakterize edilerek, hızlı, etkili ve az enerji tüketen soğutucu ısıtma tekniğine dayalı bir başlatma yöntemi geliştirilmiştir. Kurulan düzenekteki bileşenlerin soğuk çalıştırma performansına etkisi, aynı enerji tüketim seviyelerinde -10 ile -30 ℃ aralığında yapılan soğuk başlatma testleri ile araştırılmıştır. Testlerde, yakıt hücresi ile harici ısıtma sistemi aynı anda çalıştırılmış ve hücreden akım çekilmiştir. Stak sıcaklığı beş farklı simetrik noktadan takip edilmiş olup, sıcaklık-voltaj-akım profilleri çizdirilmiştir. -10 ℃'deki ön testlerde çalışma sıvısı olarak etanol, çift taraflı ısıtma tipi ve tam güç pompa çalışması en hızlı ısıtmayı sağlayan parametreler olarak belirlenmiştir. Bu sıcaklıkta, aynı enerji tüketim seviyesinde ısıtıcı ve pompa çalışma sürelerinin etkisi karşılaştırılmış ve belirgin bir fark ortaya konulmamıştır. Ancak daha zorlu çalışma sıcaklıklarında (-15 ile -30 ℃ aralığında) uzun pompa çalışmasının, başarılı soğuk çalıştırma prosesi için elzem olduğu ve daha homojen bir sıcaklık profili sağladığı anlaşılmıştır. Harici ısıtma düzeneği sayesinde PEM yakıt pili her koşulda başarılı bir şekilde çalıştırılmış olup, -10, -20 ve 30 ℃'deki testlerde hücre sıcaklığı sırasıyla 20, 40 ve 53 saniye içinde sıfırın üstüne çıkarılmıştır.

Anahtar Kelimeler: PEM yakıt pili, soğuk çalıştırma, yardımlı, başlatma tekniği, deneysel.

EXTENDED ABSTRACT

Fuel cells, which stand out with their zero-emission characteristics and are extremely clean and silent energy conversion technologies, have recently been preferred as energy generators in many industries. The most common and most advanced fuel cell type is PEM fuel cell called proton exchange membrane or polymer electrolyte membrane fuel cell. PEM fuel cells, which are preferred commercially in many applications, especially in the automotive and aerospace industries, have some fundamental features such as low-temperature operation, fast start-up, and high power density. On the other hand, some chronic problems could not be overcome until now, such as the expense and dependence of the platinum material used as an accelerator for the reactions in the catalyst component, and the flooding issue that occurs with the formation of water molecules on the cathode side.

Another important issue that needs to be solved and improved in the PEM fuel cell is the cold start problem, which is the main scope of this thesis. The cold start problem originates from the difficulties in starting the PEM fuel cell at sub-zero temperatures. The problem derives from the freezing of formed water molecules in the cell when the ambient temperature drops below zero after the fuel cell is shut down. Water particles prevent the reaching of fresh gas and novel reactions in the active area by freezing in each layer of the MEA, especially on the catalyst layer. In this case, the cell cannot raise its temperature above zero since sufficient reaction and heat production cannot be provided on the cell surface, then the new water molecules formed freeze and the active area is completely cut off from the reactions and therefore the cell becomes unable to generate electricity. This situation, which is called cold start failure in the literature, is one of the most significant handicaps to the further commercialization of PEM fuel cells.

So far, many scientific studies and patents have been contributed to provide a solution to the cold start problem. Some institutions follow these studies and developments and set technical targets periodically. The American Department of

Energy (DOE, USA) is one of these institutions, and some technical targets regarding cold starting have been set and developments in this direction have been followed since 2005. The cold start problem has been developed with assisted and unassisted techniques in the literature. Unassisted techniques aim to improve cold start capability by optimizing the components and operating conditions in the fuel cell system. Assisted techniques, on the other hand, include providing heat to the cell from an external source and increasing the cell temperature above zero as soon as possible. From the perspective of these two methods, it is understood that a much easier and faster cold start operation can be achieved with assisted techniques. Because it is not possible for a PEM fuel cell that raises its temperature above zero thanks to its physical characteristics (no matter what size it is) under extreme conditions. Therefore, an external heat source is required to overcome the existing issue. This energy to be provided from auxiliary sources such as batteries, electric heaters, exothermic reactions, and catalytic H_2/O_2 reactions can help to increase the stack temperature quickly.

In this thesis study, the coolant heating method which raises the temperature of the single-cell stack from sub-zero temperatures by heating coolant using an electrical heater is adopted. The main advantages of this method can be highlighted as providing a fairly homogeneous temperature profile and not causing any stress in the cell. In some approaches, an increase in temperature is provided with the help of electricity supplied to the cell. However, these applications cause stress in the cell and lead to degradation and a decrease in cell durability. In this context, considering the mentioned issue, there is no effect or contact with the cell in the assigned method, and it can be said that the damage to the membrane is at a minimum level.

Thanks to the established experimental setup, the constant mass working fluid (mostly ethanol) was kept in an instant electric heater and upon the start of the cold start test; on the one hand, it was heated by an electric heater, on the other hand, it was circulated bilaterally through the channels machined to the backside of the bipolar plates to warm-up the single-cell stack. At the same time, the reactions

occurring in the cell by sending gas to the cell also contributed to the increase in temperature. Cold start tests were carried out at temperatures of -10, -15, -20, -25, and -30 ℃ by keeping the whole system in a conditioning cabinet, and the effects of some operating parameters were investigated and compared. In the cold start process, the stack temperature can be increased with various applications, but the applied method also should have a low energy consumption level which is another significant target. The most energy-consumed components in the experimental bench are the heater and the pump that provides the fluid cycle. It is seen that the energy consumption by the heater operating for 1 second is equal to the energy consumption by the pump operating for 22.5 seconds when the heater power (1800 W) used is compared with the power of the pump (12V-DC liquid pump – maximum 80 W). The strengths and capabilities of these approaches have been demonstrated by low-temperature tests under the same energy consumption levels. This characterization has been achieved as a result of temperature monitoring by connecting thermocouples to the five holes machined in the mid-section of the cathode bipolar plate cell. Thanks to these symmetrical channels, temperature changes in the cell were recorded throughout the test. Synchronically, reactant and oxidant gases were supplied to the inside of the cell, and the current was drawn during tests. Each test was maintained for ten minutes, and temperature, cell voltage, and current values were followed. No significant difference was observed in the tests at -10 and -15 ℃ when the effects of long heater operation and long pump operation were compared. However, the positive effect of long pump operation on cell performance and homogeneous temperature distribution has been demonstrated when the operating temperature drops further (-20, -25, and -30 ℃). The long heater start-up operation increased the maximum temperature reached by the cell. However, sharp decreases were experienced in the temperatures and this situation affects the fuel cell stabilization negatively since the pump was operated for a shorter time in this process. In the other procedure, the cell temperature could rise to a certain level, but a homogeneous temperature decrease profile was achieved by providing a long pump

circulation. This method did not cause any negative effects on cell performance. In all tests conducted at -10 ℃ (except for the unassisted operation of the cell), the temperature rose above zero within 20 seconds. In tests at -20 ℃, a rise to above zero was achieved in about 40 seconds, while at -30 ℃ the same goal was achieved in around 53 seconds. On the contrary, as the starting temperature decreases, the maximum temperature values that the cell can reach also decrease. While the cell temperature increased up to 30 ℃ in tests at -10 ℃, a maximum temperature of 10 ℃ was reached in tests under the same conditions at -30 ℃. The maximum temperature and cell current values reached in all tests are at different levels, and all results are presented in detail.

Another important point observed in the light of experimental studies is the fact that there must be no water particles in the cell before starting the cold start test, that is, a dry membrane must be used. Successful operations cannot be reached by shutdown the PEM fuel cell after operating for a while and restarting after drops below zero. The water particles in the cell freeze in the channels, and membrane layers; therefore ice covers the active area and prevents the fresh gas from reaching the active area. This easily leads to a cold start failure. The stack was decomposed after each test and the water in the MEA and flow channels was removed to provide tests under the same operating conditions and to prevent this failure, and then the next test was started.

GENİŞLETİLMİŞ ÖZET

Sıfır emisyon karakteristiği ile ön plana çıkan, son derece temiz ve sessiz enerji dönüşüm teknolojileri olan yakıt pilleri, son zamanlarda birçok endüstride enerji üreteci olarak tercih edilmektedir. Yakıt pili tipleri içinde en yaygını ve en gelişmiş olanı, proton değişim membranlı veya polimer elektrolit membranlı yakıt pili olarak adlandırılan PEM yakıt pilleridir. Ticari olarak otomotiv ve havacılık sektörleri başta olmak üzere birçok endüstride tercih edilen PEM yakıt pilleri, düşük sıcaklıkta çalışma, hızlı başlatma ve yüksek güç yoğunluğu gibi bazı temel avantajlara sahiptir. Öte yandan, katalizör kısmında reaksiyonları hızlandırıcı olarak kullanılan platin malzemesinin pahalı olması ve buna bağımlı olunması, katot tarafında su moleküllerinin oluşmasıyla meydana gelen taşma olayları gibi bu zamana kadar aşılamayan bazı kronik problemleri de mevcuttur.

PEM yakıt pilinde çözülmesi ve geliştirilmesi gereken diğer bir önemli olay ise, bu tezde çalışılan ana tema olan soğuk çalıştırma veya soğukta çalıştırma problemidir. Soğuk çalıştırma problemi, PEM yakıt pilinin sıfırın altındaki sıcaklıklarda çalıştırılmasındaki güçlüklerden türemiştir. Bu problemi meydana getiren durum ise, yakıt pili normal çalışma koşullarında oluşan su moleküllerinin yakıt pili durdurulduktan (kapatıldıktan) sonra ortam sıcaklığının sıfırın altına düşmesiyle donmasıdır. Su partikülleri gaz akış alanlarında, membranın her katmanında ve bilhassa katalizör yüzeyde donarak aktif alana taze gazın ulaşmasını ve yeni reaksiyonları engeller. Bu durumda hücre yüzeyinde yeterli reaksiyon ve ısı üretimi sağlanamadığı için, hücre kendi sıcaklığını sıfırın üstüne çıkaramaz ve oluşan yeni su molekülleri de donarak, aktif alan tamamen reaksiyonlardan kesilir ve hücre elektrik üretemez hale gelir. Literatürde soğuk çalıştırma hatası olarak adlandırılan bu durum, PEM yakıt pillerinin tamamen ticarileşmesinin önündeki en büyük engellerden biridir.

Soğuk çalıştırma problemine çözüm sunmak amacıyla bu zamana kadar çok sayıda bilimsel çalışma ve patent ile katkıda bulunulmuştur. Yapılan bu çalışma ve

gelişmeleri takip eden ve periyodik zamanlarla teknik hedefler belirleyen bazı kurumlar bulunmaktadır. Amerikan Enerji Departmanı (Department of Energy, USA) bu kurumların başında gelmektedir ve 2005 yılından bu yana soğuk çalıştırma ile ilgili bazı teknik hedefler belirlenmiş ve bu doğrultuda yapılan gelişmeler takip edilmiştir. Literatürdeki çözüm metotlarına bakılırsa, soğuk çalıştırma sorunu yardımlı ve yardımsız tekniklerle geliştirilmiştir. Yardımsız teknikler, yakıt pili sistemindeki bileşenlerin ve çalışma koşullarının optimize edilmesiyle soğuk çalıştırma yeteneğinin geliştirilmesini amaçlamaktadır. Yardımlı teknikler ise, hücreye harici bir kaynaktan ısı sağlanması ve hücre sıcaklığının en kısa sürede sıfırın üstüne çıkarılmasını kapsamaktadır. Bu iki metot açısından bakılacak olursa, yardımlı teknikler ile çok daha kolay ve hızlı bir soğuk çalıştırma operasyonu sağlanacağı anlaşılabilir. Çünkü PEM yakıt pilinin (hangi stak boyutlarında olursa olsun) ekstrem şartlarda kendi kendine sıcaklığını sıfırın üstüne çıkarması mümkün değildir. Bunun için harici bir ısı kaynağına ihtiyaç duyulur. Batarya, elektrikli ısıtıcı, ekzotermik reaksiyonlar, katalitik H_2/O_2 reaksiyonu gibi yardımcı kaynaklardan sağlanacak olan enerji, stak sıcaklığının hızlı bir şekilde yükseltilmesine yardımcı olabilir.

Bu tez çalışmasında, elektrikli ısıtıcı kullanılarak ısıtılan bir soğutucu akışkanın, sıfırın altındaki sıcaklıklardan tekli yakıt pili stağının sıcaklığını yükseltmesi metodu benimsenmiştir. Bu yöntemin avantajları oldukça homojen sıcaklık profili sağlaması ve hücrede bir strese neden olmaması olarak öne çıkarılabilir. Bazı metotlarda hücreye elektrik verilmesi sonucu sıcaklık artışı sağlanmaktadır. Ancak bu ve buna benzer durumlar hücrede gerilmeye yol açmakta ve hücre ömrünün azalmasına ve bozunmasına neden olmaktadır. Bu bağlamda seçilen yöntemde hücreye hiçbir etki ve temas olmadığını düşünecek olursak, membrana verilen zararın minimumda olduğu söylenebilir.

Tez kapsamında kurulan deneysel düzenekte çalışma sıvısı (çoğunlukla etanol) sabit bir kütlede elektrikli ısıtıcı içinde tutulmuş ve soğuk çalıştırma testinin başlatılmasıyla birlikte, bir yandan elektrik enerjisiyle ısınırken, diğer yandan tekli

yakıt pili hücresinin bipolar plakalarının arka (sırt) kısmına açılan kanallardan çift taraflı dolaşarak stağı ısıtmıştır. Ayrıca hücreye de gaz gönderilerek hücre içinde meydana gelen reaksiyonlar da sıcaklık artışına katkıda bulunmuştur. Tüm sistem bir şartlandırma kabini içinde muhafaza edilmek suretiyle, -10, -15, -20, -25 ve -30 °C sıcaklıklarda soğuk çalıştırma testleri gerçekleştirilmiş ve bazı parametrelerin etkisi karşılaştırılmıştır. Soğuk çalıştırma operasyonunda çeşitli uygulamalar ile stak sıcaklığı yükseltilebilir, ancak uygulanan yöntemin az enerji tüketmesi de hedefler arasındadır. Kurulan düzenekte en fazla enerji tüketen bileşenler ısıtıcı ve akışkan çevrimini sağlayan pompadır. Kullanılan ısıtıcı gücü (1800 W) ile pompanın (12V-DC sıvı pompası – maksimum 80 W) gücü mukayese edildiğinde ısıtıcının 1 saniye çalışması sonucu harcadığı enerjinin, pompanın 22,5 saniye çalışması ile harcadığı enerjiye eşit olduğu görülmektedir. Bu iki durumdan hangisinin daha avantajlı olduğu düşük sıcaklık testleriyle, aynı enerji tüketim seviyelerinde ortaya koyulmuştur. Bu karakterizasyon, tekli hücrenin katot bipolar plakasının orta kısımlarına açılan beş deliğe termokupllar bağlanması ile sıcaklık takibi sağlanması sonucu sağlanmıştır. Simetrik açılan bu kanallar sayesinde hücrede meydana gelen sıcaklık değişimleri test boyunca kayıt altına alınmıştır. Testlerin başlatılmasıyla birlikte hücreye de gaz gönderilerek akım çekilmiştir. Her bir test on dakika sürdürülmüş, beş farklı noktadan sıcaklık kaydı ve hücre akım ve voltaj değerleri takip edilmiştir. Uzun süre ısıtıcı çalıştırılması ve uzun süre pompa çalıştırılması durumlarının etkisi karşılaştırıldığında, -10 ve -15 °C'deki testlerde arada belirgin bir fark gözlenmemiştir. Ancak çalıştırma sıcaklığı daha da düştüğünde (-20, -25 ve -30 °C) uzun pompa çalıştırmanın hücre performansı ve homojen sıcaklık dağılımına olumlu etkisi ortaya koyulmuştur. Uzun ısıtıcı çalıştırma operasyonu, hücrenin ulaştığı maksimum sıcaklığı daha da artırmıştır. Ancak bu proseste pompa daha kısa süre çalıştırıldığı için sıcaklık değerlerinde ani düşmeler yaşanmış ve bu durum yakıt pili stabilizasyonunu bozmuştur. Diğer yöntemde ise, kısa süreli ısıtıcı çalışması ile hücre sıcaklığı belirli bir seviyeye kadar çıkabilmiş, ancak ısıtıcının kapatılması ve uzun pompa sirkülasyonu sağlanması ile daha yumuşak bir sıcaklık düşüş profili

sağlanmıştır. Bu durum hücre performansında bir olumsuzluğa sebebiyet vermemiştir. -10 ℃'de yapılan tüm testlerde (hücrenin yardımsız çalışması hariç) sıcaklık, 20 saniye içinde sıfırın üstüne yükselmiştir. -20 ℃'deki testlerde 40 saniyeye yakın bir sürede sıfırın üstüne yükselme sağlanırken, -30 ℃'de 53 saniye civarında aynı amaca ulaşılmıştır. Bu duruma ters orantılı olarak, çalıştırma sıcaklığı düştükçe hücrenin ulaşabileceği maksimum sıcaklık değerleri de düşmüştür. -10 ℃'deki testlerde hücre sıcaklığı 30 ℃'ye kadar yükselirken, -30 ℃'deki aynı şartlar altındaki testlerde maksimum 10 ℃ sıcaklığa erişilmiştir. Tüm testlerde ulaşılan maksimum sıcaklık ve hücre akım değerleri farklı seviyelerde olup, tüm sonuçlar detaylı bir şekilde sunulmuştur.

Tez kapsamında yapılan deneysel çalışmalar ışığında gözlemlenen diğer önemli bir husus ise, soğuk çalıştırma testine başlamadan önce hücrede su partikülü bulunmamasının hayati olduğu, yani kuru membran kullanılması gerektiği gerçeğidir. PEM yakıt pili bir süre çalıştırıldıktan sonra kapatılması ve sıfırın altına düştükten sonra tekrar çalıştırılması ile başarılı sonuç elde edilemez. Hücre içindeki su parçacıkları kanallarda ve membran tabakalarında donarak, aktif alanı buz kaplamakta ve taze gazın aktif alana ulaşmasını engellemektedir. Bu durum kolayca soğuk çalıştırma hatasına yol açmaktadır. Bu durumun önüne geçmek ve testleri aynı şartlar altında test etmek için, yapılan her testten sonra stak bozulmuş ve membran ve akış kanallarındaki suyun yüzeyden uzaklaştırılması sağlandıktan sonra diğer teste başlanmıştır.

ACKNOWLEDGMENTS

I would like to present my gratitude to my supervisor Prof. Dr. Kadir Aydın for his unlimited support, deep understanding, profound experience, and providing a flexible research platform at each stage of the thesis.

I am also thankful to my co-supervisor Prof. Dr. Selahattin Çelik for his deep experience on the scope of the thesis, help with the thesis content, precious recommendations, and guidance during the experimental tests. In addition, I would like to thank T. Nejat Veziroğlu Clean Energy Research Center (Niğde Ömer Halisdemir University, Niğde, Turkey) and also the researcher and my friend Mikail Yağız from there for their valuable contribute to my experimental studies.

I would like to thank Muhammet Yıldırımcan for his help in the experimental establishment stage, and Ahmet Özkan Kocamanoğlu, my close friend from the high school years, for his unlimited support on the numerical calculations.

I would also acknowledge the financial support of the Scientific Research Project Unit of Çukurova University (Project No: FDK-2020-12750).

I am much obliged to dear my father Selami and my mother Cemile for their unrequited love, emotional support, and put importance on my education both academically and socially throughout my life. I also dedicate this study to them as a little gift for their endless efforts.

Dear my wife, best friend, and colleague Merve. You shared all trouble and stress with me through the work. I'm thankful for all your sacrifice, insightfulness, and patience. Also thank you so much for giving me two children and making me the happiest man in the world.

All my world and my happiness my son Kerem Alp and my daughter Leyla. You have been my source of joy throughout the thesis study. I hope this work will inspire you in the future. I wish you all the best…

CONTENTS **PAGE**

LIST OF TABLES **PAGE**

LIST OF FIGURES **PAGE**

NOMENCLATURE

A	:	Ampere
AA	:	Active area
AFC	:	Alkaline fuel cell
A/cm^2	:	Ampere per centimetre square (current density)
A_c	:	Cross-sectional area
bhp	:	Brake horsepower
BP	:	Bipolar plate
C	:	Current
CD	:	Current density
CL	:	Catalyst layer
cm^2	:	centimetre square
c_p	:	Specific heat capacity
CT	:	Cell temperature
CV	:	Cell voltage
D	:	Diameter
DC	:	Direct current
DI	:	Deionized
DMFC	:	Direct methanol fuel cell
DOE	:	Department of Energy
DSC	:	Differential scanning calorimetry
D_h	:	Hydraulic diameter
ECSA	:	Electrochemical surface area
EIS	:	Electrochemical impedance spectroscopy
E-spun CL	:	Electrospun catalyst layer
f	:	Darcy friction factor
FC	:	Fuel cell

FCH JU	:	Fuel Cells and Hydrogen Joint Undertaking, Europe
FCV	:	Fuel cell vehicle
F/T	:	Freeze/thaw
g	:	Gravity
GDL	:	Gas diffusion layer
g/cm^3	:	gram per centimetre cube (density)
H_2	:	Hydrogen gas
h_L	:	Head loss
I/C ratio	:	Ionomer/carbon ratio
I/V curve	:	Current/Voltage (polarization) curve
h	:	hour
HFR	:	High-frequency resistance
HOR	:	Hydrogen oxidation reaction
J	:	Joule
k	:	Thermal conductivity
K	:	Kelvin
kW	:	kilowatt
K_L	:	Loss coefficient
L	:	Litre
L	:	Duct length
Lpm	:	Litre per minute
L_h	:	Entry length
MEA	:	Membrane electrode assembly
m	:	meter
mA	:	milliampere
MCFC	:	Molten carbonate fuel cell
min	:	minute
ml	:	millilitre

mm	:	millimetre
MOST	:	National Reform Commission, China
MPL	:	Micro-porous layer
NEDO	:	New Energy and Ind. Tech. Dev. Org., Japan
Nu	:	Nusselt number
NTU	:	Number of transfer units
N_2	:	Nitrogen gas
OAC	:	Open anode channels
OCC	:	Open cathode channels
ORR	:	Oxygen reduction reaction
O_2	:	Oxygen
Pa	:	Pascal
PAA	:	Polyacrylic acid
PAFC	:	Phosphoric acid fuel cell
PCB	:	Printed circuit board
PCM	:	Phase change material
PEMFC	:	Proton exchange membrane fuel cell
PEN	:	Positive/electrolyte/negative
PPS	:	Polyphenylene sulfide
Pr	:	Prandtl number
psi	:	pounds per square inch
Pt/C	:	Platinum/Carbon ratio
PTFE	:	Polytetrafluoroethylene
Re	:	Reynolds number
RH	:	Relative humidity
s	:	second
sccm	:	Standard cubic centimetres per minute
SEM	:	Scanning electron microscopy

SLPM	:	Standard litre per minute
SS	:	Stainless steel
TEC	:	Thermal expansion coefficient
TEM	:	Transmission electron microscope
T_b	:	Bulk mean fluid temperature
T_e	:	Exit temperature
T_i	:	Inlet temperature
T_m	:	Mean temperature
T_s	:	Surface temperature
USA	:	United States of America
v	:	Kinematic viscosity
V	:	Voltage
V_{avg}	:	Mean velocity
W	:	Watt
Wh	:	Watthour
wt%	:	percentage in weight
W/kg	:	Watt/kilogram
µm	:	micrometre
μ	:	Dynamic viscosity
ρ	:	Density
ε	:	Equivalent roughness
ε/D	:	Relative roughness
η_{pump}	:	Pump efficiency
$\dot{m}$	:	Mass flow rate
$\dot{Q}$	:	Heat transfer ratio
$\dot{V}$	:	Volume flow rate
$\dot{W}_{pump}$	:	Pumping power
ΔP_L	:	Local pressure drop

ΔT_{avg}	:	Arithmetic mean temperature difference
ΔT_{lm}	:	Log mean temperature difference
℃	:	Celsius degree
%	:	percentage
~	:	approximately

1. INTRODUCTION

Energy demand is increasing worldwide year by year. Due to the harmful effects of fossil sources, researchers focused on clean and alternative energy sources for many years (Gomez et al., 2015; Darıcık et al., 2019; Topcu et al., 2019). Fuel cell technology has gained attention in the last two decades owing to its high efficiency, silent operation, and low pollution (Koçak et al., 2019; Topcu et al., 2018). Fuel cell (FC) is an efficient electrochemical energy transformation device that can convert the chemical energy of fuel into electricity without combustion (Sulaiman et al., 2019). Positive electrode/electrolyte/negative electrode (PEN) structure called membrane electrolyte assembly (MEA) which consists of main part (so to say the heart of the system) of the FC system (Sørensen, 2012). Although operating logic is the same for FC types, MEA type, operating temperatures, specifications, and range of materials vary depending on each specific type of FC. Sealing materials, gas distribution plates, current collector plates, and end (compression) plates are the main components of the FC stack as well as MEA (Kumar et al., 2004). The main fuel cell types and their specifications are presented in Table 1.1. They are named according to their electrolyte type (material) in general. However, that may classify by the operating temperature such as low-temperature, intermediate-temperature, or high-temperature FCs. In addition, many different and novel FC types are derived in recent years as well as presented FC types in Table 1.1. The main examples are; direct ethanol FC (Singh and Mahapatra, 2023), alkaline anion exchange membrane FC (Wang et al., 2022), microbial FC (Limbergen et al., 2022), direct borohydride FC (Ertürk et al., 2022), direct formic acid FC (Jałowiecka et al., 2022), microfluidic FC (Ma et al., 2023).

PEM (proton exchange membrane or polymer electrolyte membrane) fuel cell is one of the most developed fuel cell types and has the potential for applications in transportation (Liu et al., 2014; Nandjou et al., 2016), military (Gencoglu and Ural, 2009; Sankar et al., 2018), stationary (Gencoglu and Ural, 2009; Ozden et al.,

2019), portable (Paul et al., 2017; Sankar et al., 2018), submarines (Leo et al., 2010; Rivaloro et al., 2020), unmanned aerial vehicles (Gong et al., 2017; Cao et al., 2019) and space shuttles (Leo et al., 2010).

Table 1.1. Main fuel cell types and their specifications (Irshad et al., 2016)

Fuel Cell	**Operating Temperature (ºC)**	**Fuel Type**	**Electrolyte Type**	**Application Industries**
PEM	40-80	H_2	Polymer	Portable, mobile, automotive, military, aviation, stationary
AFC	40-200	H_2	KOH	Mobile, space, military
DMFC	60-130	Methanol	Polymer	Mobile, portable
PAFC	200	H_2	Phosphoric acid	Stationary
MCFC	550-650	CH_4, H_2, CO	Molten carbonate	Stationary, CHP
SOFC	600-1000	CH_4, H_2, CO	Ceramic	Stationary, military, CHP, co-generation

Figure 1.1. Some FCV manufacturers and their FCV models; a) Toyota Mirai, b) Honda Clarity, c) Mercedes-Benz GLC F-CELL, d) Hyundai ix35 FCEV (Website, 2023a)

The most promising PEMFC applications are experienced in the automotive and aviation industries up to the present. Some examples in automotive and other application industries are demonstrated in Figures 1.1 and 1.2, respectively.

Figure 1.2. FC applications on transportation; a) train, b) sport car, c) bus, d) passenger plane, e) motorcycle, f) UAV, g) heavy-duty truck, h) passenger van, i) marine, j) tractor, k) forklift, l) medium-duty truck

Hydrogen as a reactant and air as an oxidant sends to the anode and cathode sides of the PEM fuel cell, respectively. That device operates at 60-70 °C temperatures silently and has outstanding virtues such as high-power density at low temperatures, fast start-up, system robustness, and zero-emission (Li et al., 2005). Typical PEMFC stack components are illustrated in Figure 1.3 (left). A short stack consists of MEA, gaskets, bipolar plates, current collector plates, and end plates - from the inside out- (Qiu et al., 2019). And MEA details are presented in Figure 1.3 (right). An MEA comprises of polymer membrane (~50 μm thickness), catalyst layers, micro-porous layers (MPLs, if available), and gas diffusion layers (GDLs, ~400 μm), typically.

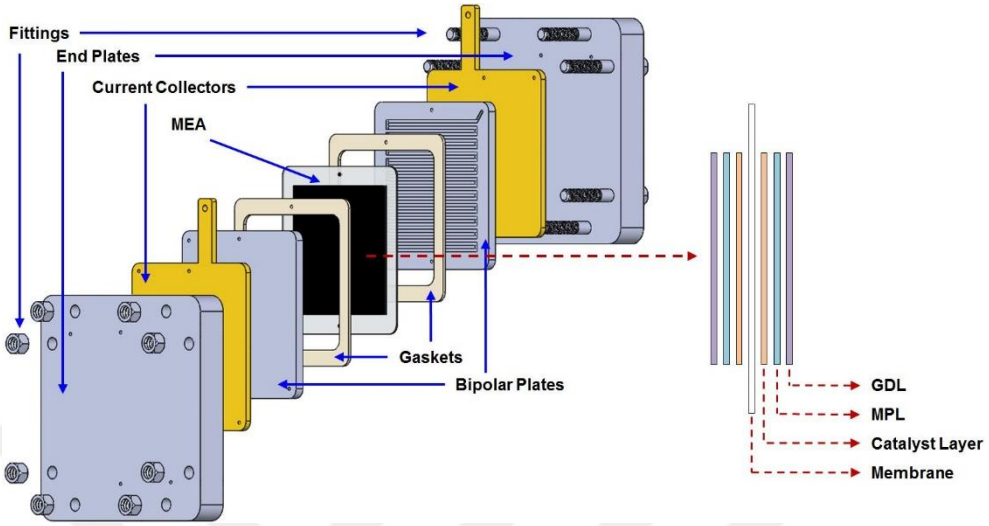

Figure 1.3. Single-cell components of PEMFC (left), details of MEA (right)

In the PEMFC operating system, hydrogen gas (H_2) and air distribute to the flow channels of bipolar plates. H_2 is diffused by GDL and delivered to the catalyst layer. H_2 molecules reduce and electrons separate when H_2 arrived at the catalyst surface. This catalytic reaction occurs on the anode side and is called the hydrogen oxidation reaction (HOR) (Barbir, 2005). Polymer electrolyte allows hydrogen ion passing to the cathode side but do not let electron transfer. Herein, electrons convey to the cathode side through the external manifold and complete the circuit. At the same time, oxygen molecules (from the air) react with the protons at the cathode side, and this reaction is called the oxygen reduction reaction (ORR) (Chippar and Ju, 2012; Jo et al., 2015). Heat occurs thanks to exothermic H_2-½O_2 reaction and this waste heat is very important to the survivability and continuity of FC operation (Ko et al., 2012; Gwak et al., 2015; Mohamed and Kamil, 2016).

1.1. Commercialization and Main Challenges

PEM fuel cells prefer in many industries owing to their high-power density and fast start-up specifications. Toyota motor corporation introduced into the market the first mass-produced hydrogen fuel cell vehicle (FCV) model of the world ‘Mirai’

in 2014 (Xu and Xu, 2018). Honda (Clarity model) and Hyundai (Nexo model) corporations released their FCV models to the market in the later years in response to this commercial move of Toyota (Website, 2023b). Over 45 hydrogen gas stations in the U.S. and over 60 in Germany provide service with the commercialization of FCVs (Wang et al., 2020a). Although investments are growing year by year, the number of hydrogen gas stations is insufficient around the world. Even though PEMFCs have passed the demonstration phase and reached commercialization, still advances are needed to handle the remaining challenges associated with cost and durability (Amamou et al., 2016; Mohamed et al., 2016). Percentage distributions of cost allocation and weight estimation of the PEMFC stack are pointed out in Figure 1.4. MEA components which are membranes, catalysts, and GDLs, comprise markedly a great part of cost breakdown as understood in Figure 1.4-a (Website, 2016a). If mass production of all stack components considers, percentage values of catalysts and bipolar plates increase while membranes and GDLs decrease (Wang et al., 2020a). Cost-saving studies on MEA components will contribute to cut down stack expenditure. Besides, bipolar plates, end plates, and fasteners constitute virtually 90% of stack weight as seen in Figure 1.4-b (Kahraman et al., 2014; Evangelisti et al., 2017). Conceiving that the bipolar plates and end (compression) plates are usually made of metal-based materials, the quantiles of components can acceptable ordinarily (Öztürk et al., 2018). Therefore, studies on reducing the weight of bipolar plates are very critical in order to obtain lightweight stack construction, at the same time (Koçak et al., 2019).

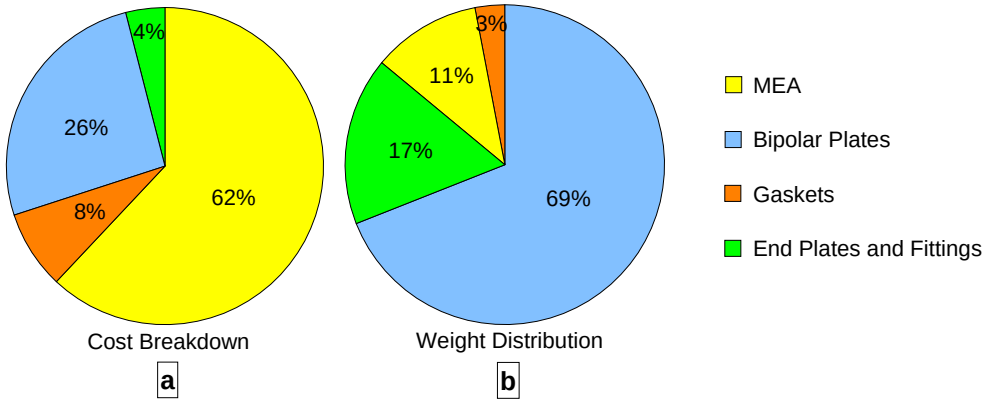

Figure 1.4. PEMFC stack; a) cost estimation (Website, 2016a), b) weight distribution (Kahraman et al., 2014; Evangelisti et al., 2017)

1.2. Cold Start Phenomenon

PEMFCs perform at 60-70 °C operating temperatures, normally. Nonetheless, it should start and operate at subfreezing temperatures, too (Mench, 2008; Du et al., 2014). Some countries have cold weather conditions and FCV should satisfy those expectations. Cold start capability is one of the remaining challenges for PEMFC commercialization in sub-zero conditions (Meng, 2008; Gwak et al., 2014; Zhou et al., 2014; Tang et al., 2017). Water is formed byproduct of H_2-½O_2 reactions at normal operating conditions of PEMFC. Produced water particles remove from the reaction areas during operation thanks to flow channels. If the drainage process does not carry out successfully, this circumstance brings about the cathode flooding problem which is another important challenge for PEMFCs (Öztürk et al., 2017; Öner et al., 2020). Moreover, if water particles do not evacuate from the stack completely, droplets can freeze under subzero temperatures after the system shutdown and lead to start-up failure (Amamou et al., 2018; Huo et al., 2019; Pan et al., 2020). This phenomenon is known as ‘cold start’ which means start-up at subzero temperatures. Cold start term was mentioned in early studies by Penner et al. (1995), and Appleby (1995). Numerous publications and patents were contributed to enhance the cold start ability of the PEMFC system up to the present. Bibliometric

analysis has been performed on publications in the last 15 years that investigated the cold start characteristics or process of PEMFCs. Data was obtained using Web of Science, and "cold start" or "subzero temperatures" and "PEM fuel cells" terms were used as keywords to search articles. In addition, only titles, abstracts, or keywords of Science Citations Indexed articles were considered. Bibliometric analysis of the publications was presented by years and regional distributions in Figure 1.5-a and Figure 1.5-b, respectively. Therefore, it is understood that the popularity of the topic has been improving especially in recent years and from all over the world.

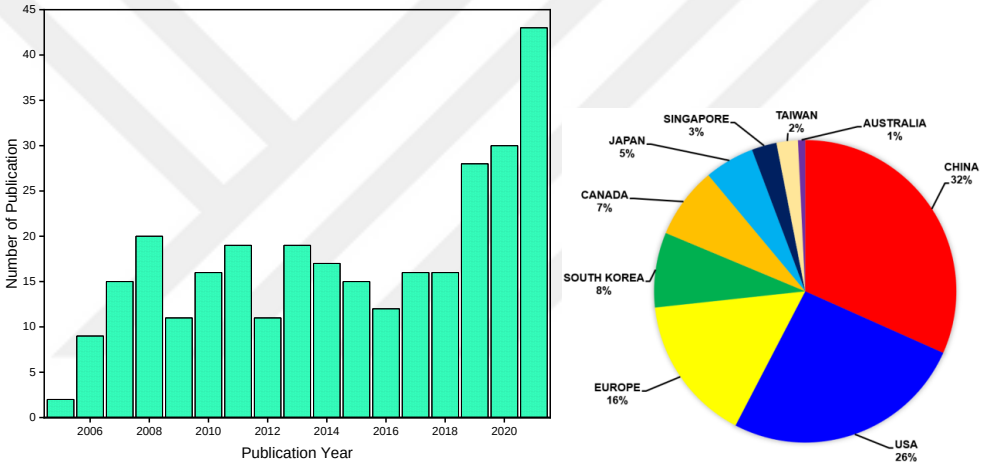

Figure 1.5. Bibliometric analysis of the publications; a) Article numbers by years, b) Regional distribution of articles

1.3. Technical Targets

Cold start aptitude of PEMFC has been investigated and developed for decades. Therefore, some technical roadmaps are needed to follow the existing situation, improvements, and next targets. U.S. Department of Energy (DOE) institution specifies fuel cell roadmaps, periodically. In 2005, cold start-up time was aimed at -20 °C ambient temperature in 60 seconds (Website, 2005). Unassisted cold start, energy efficiency, and cold start-up time to 50% of rated power targets were listed in the next roadmaps (Website, 2014; Website, 2017). DOE technical targets

related to cold start characteristics for 2020 were pointed out in Table 1.2 (Website, 2021).

Table 1.2. 2020 Cold start related technical targets for PEMFC-powered transportation systems by different institutions (operating on direct hydrogen)

Characteristic	Unit	DOE	FCH JU	MOST	NEDO
Cold start-up time	s	30	30	-	30
Cold start-up temperature (unassisted)	°C	-30	-25	-30	-40
Cold start-up temperature (assisted)	°C	-40	-40	-	-
Start-up/shutdown durability	cycle	5000	-	-	-
Start-up and shutdown energy (from -20 °C)	MJ	<5	-	-	-

Cold start temperature set to -30 and -40 °C for the unassisted and assisted starter techniques, respectively. These magnitudes are ultimate values, at the same time. In addition, start-up/shutdown energy (from -20 °C ambient temperature) must below 5 MJ as shown in Table 1.2. This target is highly sensational and intriguing for future studies. Other institutions in various regions of the world adjust targets apart from DOE. These institutions are European Fuel Cell and Hydrogen Technology Platform (FCH JU) in Europe (Website, 2022), MOST in China (Website, 2016b), New Energy and Industrial Technology Development Organization (NEDO) in Japan (Website, 2010). All characteristics were shown and compared in Table 1.2. In addition, all roadmaps include durability, cost, and power-derived characteristics, however, only cold start related specifications were presented in this review. Moreover, comprehensive details on technical targets and test protocols are available in reviews of Chen et al. (2018) and Wang et al. (2018).

1.4. Cold Start Mechanism

Occurred water droplets accumulate in the gas diffusion layer and catalyst layer after a system shutdown, usually. Residual water can also pile up in the flow channels, but the water discharging process from flow channels is easier than gas diffusion and catalyst layers by purging gas. Therefore, unevacuable particles turn into ice form after shutdown and gas purge processes under subzero temperatures. If water freezes and ice blocks cover all catalyst surfaces under subzero temperatures without any purging after shutdown, it brings about start-up failure (Zhu et al., 2019a). Because the catalyst surface is unavailable for the reactions and electricity generation cannot carry out. In this case, stack temperature should rise above zero, ice blocks melt and gas sending process starts after the catalyst layer is convenient for reactions (Huo et al., 2017). On the other hand, waste heat gains with the exothermic H_2/O_2 reactions in the cell. When cold start begins, gases reach the catalyst layer thanks to flow channels. Owing to reactions heat generate as well as novel water droplets. If generated heat overcomes existing ice blocks and improves cell temperatures, cold start gets through successful. In the case of created heat capacity cannot come through threshold value, originated novel water dribbles freeze, too, and overspread to the whole catalyst face. This causes cold start failure (Xie et al., 2018). Consequently, as there are many parameters affecting the cold start mechanism, a successful cold start is plausible with the optimization of these parameters.

1.5. Aim of the Thesis

This thesis study aims to improve the cold start capability of the PEM fuel cell with the help of waste heat from an external power source. The coolant heating method, as an auxiliary power supply, raises the temperature of the single-cell stack from sub-zero temperatures by heating coolant using an electrical heater is adopted. The main advantages of this method can be highlighted as providing a fairly homogeneous temperature profile and not causing any stress in the cell. Because an

increase in temperature is provided with the help of electricity supplied to the cell in some approaches. However, these applications cause stress in the cell and lead to degradation and a decrease in cell durability. In this context, considering the mentioned issue, there is no effect or contact with the cell in the assigned method, and it can be said that the damage to the membrane is at a minimum level.

It is aimed to increase the stack temperature above zero at minimum time and consume minimum energy thanks to the established experimental setup at operating temperatures of -10, -15, -20, -25, and -30 ℃. The setup includes an environmental chamber to reach cold start temperatures and the heater, the pump, and the single-cell stack placed into it. Therefore, ensuring a quick, safe, and homogeneous temperature distributor heating mechanism is aimed at the scope of the thesis.

1.6. Organization of the Thesis

The thesis is organized by sub-sections of the previous studies, materials and methods, the experimental bench and case studies, the results and discussion, and the conclusion. In Section 2, the cold start-related previous studies are presented in detail. All applied methods are investigated and explained with figures. Cold start strategies are demonstrated separately, and academic studies are supported by patent applications.

In Section 3, all materials and methods are explained used in the experimental setup. The specifications of the MEA, conditioning cabinet, fuel cell test station, external heating mechanism, thermocouple installation, production details and materials of the stack, etc. Detailed information is provided to explain the functions and production techniques of the materials used in this section.

In Section 4, experimental bench and cold start cases are presented. The details on the experimental installation, conducted experiments and conditions, and case studies at different cold start temperatures are given. In this section, the details of the performed experiments are examined such as operating conditions of the

external heating mechanism and the fuel cell stack, gas flow rates, current drawn ratios, etc.

In section 5, experimental findings are presented. Temperature following the tests, current, and voltage levels are illustrated. Temperature data is converted to pictorial format using a series of mathematical approaches. The case studies are evaluated and compared. The reason for failed cold start studies, was then, discussed. Finally, fluid flow and heat transfer analyses were performed theoretically, and the findings were validated with the experimental data.

2. PREVIOUS STUDIES

Many kinds of research on the cold start issue were performed and the topic was investigated in terms of various aspects. First of all, the pioneer studies should be presented. In this direction, Pesaran et al. (2005) prepared a milestone report which includes journal articles and patents on freeze and rapid startup investigation of PEM fuel cells as an earlier review. Meng and Ruan (2011) and Guo et al. (2017) reviewed numerical studies on the cold start of PEM fuel cells. Experimental studies were tendered briefly by Mohamad (2013). Wan et al. (2014) exhibited the impacts of water freezing on stack components and presented experimental and numerical studies and strategies in their review. Amamou et al. (2016) classified cold start strategies into sub-groups and reviewed solutions at startup and shutdown of the fuel cell. Xu and Xu (2018), and Liu and Xu (2020) published progress reviews. Xu and Xu (2018) introduced the fundamentals of gas purge for enhancing cold start performance and reviewed gas purge strategies in the literature. Liu and Xu (2020) presented self and auxiliary heating strategies and influence factors of cold start. Luo and Jiao prepared one of the most comprehensive and detailed cold start review (2018). They focused on transport phenomena in cold start in conjunction with experimental and numerical studies in the literature.

On the other hand, some reviews included cold start issues as subtitles that are not related directly to the cold start topic. For instance, Kandlikar and Lu (2009) reviewed the research needs in combined water and thermal management within PEMFC and evaluated the mechanisms under normal and cold start conditions.

Jiao and Li (2011) published a comprehensive review of the water transport mechanism of PEM fuel cells. Also, experimental and numerical cold start studies were demonstrated, too. Dafalla and Jiang (2018) reported stresses and their impacts on PEMFC. Cold start theme was given as one of the stresses related to subheadings. Chen et al. (2019) reviewed the reactant starvation of PEMFC and mentioned briefly cold start. Wang et al. (2020a) published comprehensive research on the

technological status and materials of PEMFC. Cold start scope was pointed out as one of the fundamental issues for the commercialization of PEM fuel cells. Ren et al. (2020) handled degradation mechanisms of PEMFC under automotive operating conditions. The cold start process was discussed under startup-shutdown conditions of degradation species. In another review, subfreezing operation logic and thermal management in the cold start were presented by Chen et al. (2021). Rice (2021) reviewed the water-fill capacity of the membranes and its effect on the cold start performance of the PEMFC. The cold start topic was mentioned in other reviews (Wang et al., 2020b; Li et al., 2021b; Liu et al., 2021b; Pan et al., 2021; Wang et al., 2021; Madheswaran et al., 2022; Song et al., 2022; Xu et al., 2022).

The main strategies and classification of the cold start were demonstrated in this thesis study, first. Experimental studies are divided into sub-groups according to their energy source type, and each sub-group has exhibited experimental details. In addition, the methods that have been studied well and needed improvement in the literature were revealed by classifying the experimental studies.

2.1. Strategies and Classification of Cold Start

Research and studies can group as experimental, numerical, analytical, or theoretical in the most common aspects. Each group can divide sub-groups and sub-research areas in itself. Therefore, cold start research can categorize as experimental and numerical studies. But, the classification of cold start depends on not only research type but also strategies and energy source types. Pesaran et al. (2005) drew a cold start strategies chart and classified cold start issues with two subtitles: Keep-warm during dwelling and thawing & heat-up at the start. Amamou et al. (2016) plotted a cold start strategies chart, similarly. They created shutdown and cold start-up sub-groups in addition to thaw at the start and keep warm strategies.

Also, cold start studies can classify as “unassisted” and “assisted” techniques according to their energy source type. Because of the requirement of self (internal) or assisted (external) energy sources in the cold start-up process, the FC stack should

cope with this problem by one of them. Correlatively, cold start targets are defined as unassisted and assisted in the DOE documents (Website, 2014; Website, 2017). Besides, Luo and Jiao (2018) analysed assisted start-ups as a subheading of the optimization part of their review.

2.1.1. Keep Warm Strategy

The keep warm strategy is aimed to keep stack temperature above zero. Keep warm mechanism step in after FC system shutdown and stack temperature decrease and draw close to zero. Accordingly, the cold start problem solves, and material degradation inhibits since the system condition is not sub-zero temperatures (Pesaran, 2005; Oszcipok et al., 2006a). Many researchers are interiorized the keep warm strategy owing to its benefits below:

- The stack has been kept at the operating temperature and is always ready to start through the keep warm strategy.
- Damages of freeze/thaw cycles prevent since the stack temperature is above zero.
- Much more plausible for the short parking periods.
- Don’t require extra stack components and auxiliary equipment usually and therefore, does not cause the mass and volume increase in the system.

Keep warm strategy solution categories were illustrated in Figure 2.1.

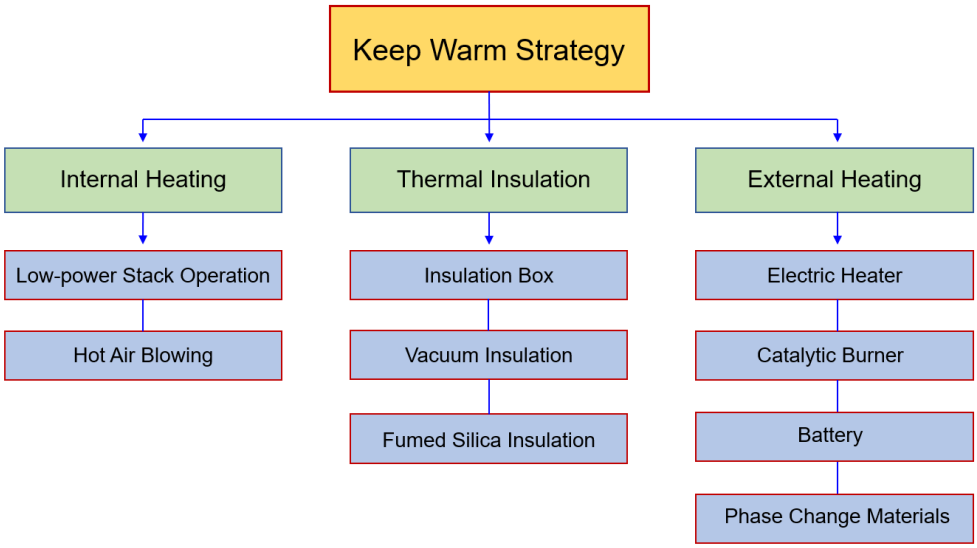

Figure 2.1. Keep warm strategy solution categories

Oszcipok et al. (2006a) developed a passive cold start model to keep warm the FC stack. In this method, the FC stack is heated by its thermal losses during operation. The method was found useful for medium power (5 kW) and automotive (85 kW) applications. However, the active cold start is needed for portable (30 W) applications because of the weak heat generation of low-power FC stacks. In another keep warm strategy study, a passive thermal management strategy was established by Sasmito et al. (2013) using phase change materials (PCM) and insulators. PEMFC stack, PCM thermal storage, and thermal insulator components were modelled with some boundary conditions such as natural convection and heat transfer. PCM was used as a passive heat source to keep the stack warm and insulator support as well as heat loss minimize. Insulator materials are very beneficial to keep warm the stack and decrease heat loss. The insulation method was used for this reason in other studies in existing literature (Sun et al., 2008; Li et al., 2011; Li et al., 2019; Pistono and Rice, 2020). In addition, a lot of patents were made that adopt the keep warm strategy (Assarabowski et al., 2004; Birk, 2004; Wheat, 2004; Bradean et al., 2006; Richards and Lin, 2007; Hayashi et al., 2009).

On the other hand, the keep warm strategy necessitates energy continuously to keep warm the stack. It leads to over energy consumption for long parking times. In the case of thermal insulation materials usage, stack volume, and weight increase. These are major drawbacks of the keep warm strategy. These disadvantages make the strategy inefficient and reduce its reliability and sustainability.

2.1.2. Thaw at Start Strategy

Thaw at start strategy does not require energy consumption during power off or parking. The goal of this strategy is to provide rapid energy and increase the temperature to proceed with electrochemical reactions in the cell. The keep warm strategy does not allow the freeze components, but the stack is frozen position in thaw at start strategy, initially. Therefore, the system needs quick energy to overcome ice accumulation and successful cold start operation (Pesaran, 2005; Sundaresan and Moore, 2005). Less energy consumption than the keep warm strategy and suitability for long parking times or power-off modes are the main advantages of thaw at start strategy (Sundaresan and Moore, 2005; Amamou et al., 2016). Many different methods and approaches can apply to fast start-up. Fundamental solution categories of thaw at start strategy are presented in Figure 2.2. Herein, the author was considered and inspired by Pesaran et al. (2005) and Amamou et al. (2016) investigations while creating ‘Keep warm’ and ‘Thaw at start’ solution charts.

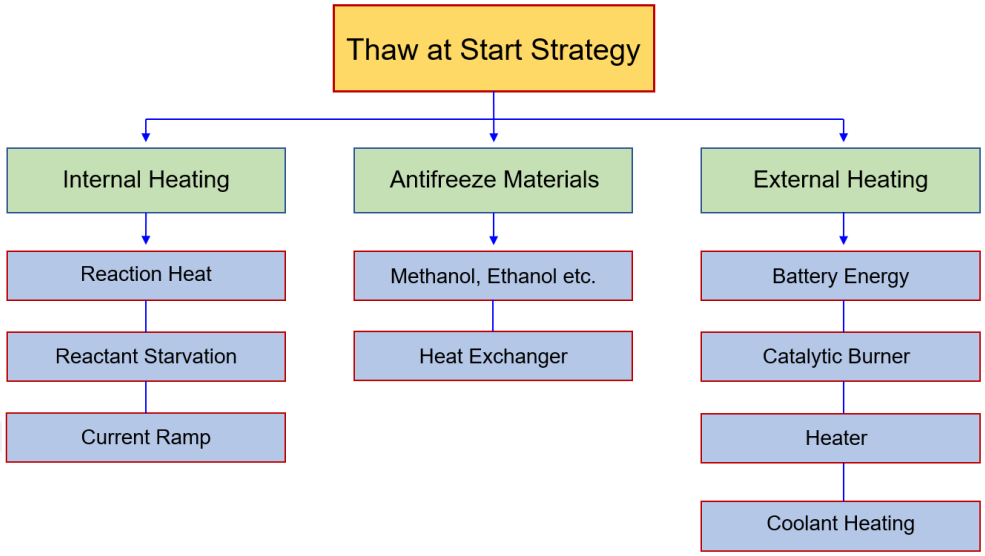

Figure 2.2. Thaw at start strategy solution categories

Sundaresan and Moore (2005a) installed a thermal model and evaluated some strategies and internal heating methods (2005b). Cho et al. (2004) considered methanol, ethanol, ethylene glycol, and isopropanol fluids as candidates for antifreeze solutions and prepared aqueous solutions with different proportions. 30% methanol or 35% glycol solution was found the best antifreeze solution for PEMFC cold start applications. In addition, they tested the gas-purging method at shutdown by dry nitrogen and oxygen. A detailed parametric study was carried out by Khandelwal et al. (2007) to investigate cold start characteristics. They concluded that catalytic heating, coolant circulation, or anti-freeze solutions are extremely effective to achieve a rapid cold start. The current ramp method is used as one of the internal heating mechanisms. The ramping current density can generate more heat and accelerates the warm-up process. Jiang et al. (2010) proposed a current-ramp strategy for rapid cold start. They touched on low initial current density (50 mA/cm^2) is not suitable for a successful cold start with any current-ramping rate. But 100 mA/cm^2 initial current density or intermediate ramping rate is enough for a successful cold start from -30 °C.

Besides, different techniques were used in some patent studies as examples of the thaw at start strategy. Wilkinson et al. (2001) proposed an inert liquid solution while Abe et al. (2004) used hot air blowing. Reiser (2004) benefited from wire heating to warm the stack and used the battery as an electric energy source. Rock and Plant (2004) generated heat thanks to catalytic hydrogen combusting and supplied gas with latent heat to warm-up the cell. Roberts et al. (2009) proposed a coolant heating method to improve cold start capability.

In the overall conclusion, both cold start strategies have virtues and drawbacks. Even though the keep warm strategy prevents material degradation and keeps the stack ready to start, it becomes unsustainable due to consuming energy continuously. On the other hand, the thaw at start strategy demands instantaneous and rapid warm-up energy to solve ice accumulation and increase cell temperature for the pursuance of electrochemical reactions. Amamou et al. (2016) classified and described cold strategies in their review study. They concluded the compensations and downsides of these strategies in detail and indicated that the keep warm strategy is more effective for a short parking time, but parking time cannot be predicted. Additionally, FCV should start within 30 seconds from -20 °C according to DOE targets (Website, 2014; Website, 2017). Hence, it can be concluded that DOE adopted rapid cold start techniques.

FC stack can cope with the cold start problem with assisted or unassisted techniques. Much feasible and rapid cold start can achieve with the assisted techniques. Because warm-up the stack with the auxiliary and various equipment is easier than self-heating. For this purpose, DOE set the assisted cold start temperature at -40 °C while unassisted is -30 °C (Website, 2021). Therefore, the experimental studies are reported into two main groups: assisted and unassisted cold start. Then, an energy consumption study is prepared due to the DOE required <5 MJ energy for the cold start application. Thus, experimental studies were tabulated to show similar and distinctive features of the approaches and prepare a guide on experimental investigation techniques for this special topic.

2.2. Assisted Cold Start

Assisted cold start techniques can accelerate the heating of the stack with assorted approaches and contribute to the cold start time. Many patents and articles published that can be considered as assisted cold start. Experimental assisted studies are demonstrated in Table 2.1. The main assist type is given with the reference and references are listed according to publish year and assist type. Test equipment, cold start test temperatures, FC test conditions, obtained values, and observations are presented as well as a schematic of the study in detail. Hence, experimental conditions are presented all together and allowed to make a comparison within the studies thanks to this table. Experimental details are given under subheadings.

2.2.1. Catalytic H_2/O_2 Reaction

Exothermic H_2/O_2 reactions gain heat to the FC system (Mohamed and Kamil, 2016). Reactions can carry out at subzero temperatures and this useful heat can contribute to the cold start process. Sun et al. (2008) researched the effect of the catalytic H_2/O_2 reaction on cold start performance. They employed two different single cells which have 4 cm^2 and 128 cm^2 active area and an FC stack which has 245 cm^2 active area with 10 cells, in their tests. The stack was kept for 6 h to fully freeze after the water removal process and also polystyrene foam insulation was applied to the single-cell stack. Cell temperature was followed by the thermal couple placed on the cathode end plate. Flow channels were considered microchannel reactors and H_2 and O_2 gases were supplied to the cathode side with different concentrations (at 0, 15, and 40% H_2 concentrations). As a result, they observed that the FC temperature increased rapidly by controlling the gas flow rate. Oszcipok et al. (2006a) compared the energy consumption of catalytic burner and electric heating methods. In another catalytic reaction study, Guo et al. (2019) compared the fuel consumption of the traditional catalytic reaction and the catalytic reaction using exhaust gas. They used 5 cell FC stack (each cell has 270 cm^2 active area) and a single-cell stack (312 cm^2 active area) on their tests and placed thermocouples in the

middle of the cathode side of each cell to follow the cell temperature (at -20, -25, -30, -35 °C cold start temperatures). In addition, they used a water pump and electric load (660 W powered) in their experimental setup as seen in Table 2.1. When considering the conventional catalytic reaction, air/H_2 mixture (5/20 L/min flow rate) was introduced to the anode side of FC and discharged from the anode tail. In other respects, the air-H_2 mix was supplied into the anode, and the exhausted gas was passed to the cathode (or air-H_2 mix was supplied into the cathode, and the exhausted gas was passed to the anode) in the catalytic reaction method using exhaust gas. When evaluating the conventional catalytic reaction assisted cold start, the method was found feasible and the short stack with metallic bipolar plate successfully operated after 82 s under the 5/20 L/min air/H_2 condition (at -20 °C cold start temperature). On the other hand, the exhaust gas utilization method significantly reduced cold start time and fuel consumption. A successful cold start was achieved in 16 s with 5/20 L/min air/H_2 condition (at -20 °C cold start temperature). Moreover, fuel consumption and cold start-up time findings of traditional catalytic reactions and the exhaust gas utilization methods were supported with tables and graphs. Several patents related to this approach have been made in addition to experimental research (Fuller and Wheeler, 2000; Rock and Plant, 2002; Gebhardt et al., 2003; Resnick et al., 2004; Rock and Plant, 2004; Korytnikov et al., 2005; Richard et al., 2006; Doctor et al., 2008; Korytnikov, 2012).

Herein, researchers should be careful with the upper and lower explosion limits of H_2 when considering the catalytic reactions to accelerate the cold start speed. Veser (2001) designed a microreactor and carried out experimental and theoretical investigations on H_2 oxidation. It was reported that the explosion limit depends not only on the reaction temperature and pressure but also on the reactor dimension. It is understood from this point that H_2/O_2 catalytic reactions can occur in an explosion-free range.

Table 2.1. Summary of assisted experimental cold start studies and details (sorted by published date and main assist type

Reference and Main Assist Type	Cold Start Temperatures and Test Equipment	FC Test Conditions	Schematic (Configuration)	Obtained Values and Figures	Major Observations
Sun et al. (2008) *(Catalytic H_2/O_2 reaction)*	-20 °C (6 h keep for fully freeze stack) Climate chamber Polystyrene foam insulation Hygrometer	First single cell test: 4 cm^2 active area (silvered end plates, parallel flow channels) 28 cm^2 AA (metal current collector) FC stack: 10 cells with 245 cm^2 AA	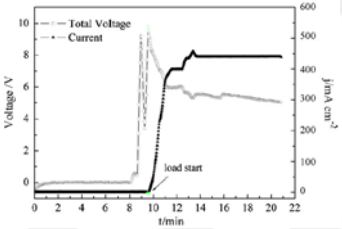	I-V curves Cyclic voltammetry graphs CT-T graphs Relative humidity (RH) measurements	Heat generated rate was proportional to the gas flow rate in the case of cell active area and H_2 concentration were constant.
Guo et al. (2019) *(Catalytic H_2/O_2 reaction)*	-20, -25, -30, -35 °C Environment chamber Electric load (660 W) Water pump Dry nitrogen purge	FC stack tests: 5 cells, each cell has 270 cm^2 AA SS 316L BPs Single cell tests: 312 cm^2 active area composite bipolar plates, graphite parallel flow channels	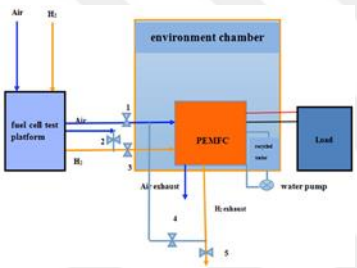	Cell temperature is measured by the thermocouples placed in the middle of cathode side of each cell. Polarization curves CT-T graphs	Hydrogen (20 L/min) and air (5 L/min) were sent to the anode channel. Exhaust gas sent to the cathode side and heat was used to warm the stack.
St-Pierre et al. (2005) *(Reactant starvation, methanol combustion, different coolants)*	-5, -15, -20 -23 °C Ethylene glycol / water, FC-40, FC-70, FC-77 coolants Dry gas purge system	FC stack test: 10-cell DMFC stack, 0.4 – 2 M methanol was supplied from fuel inlet stream Dry gas purged at shutdown (hot and cold)	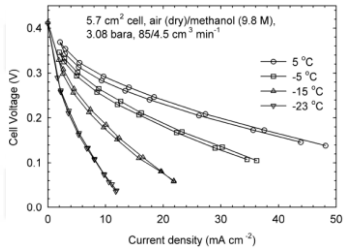	CV-CD graphs CT-T graphs CV-T graphs Coolant temp. – oxidant sto. graph I-V curves CV – freeze / thaw cycle graph	Different parameters and cold start strategies were evaluated. Water/ethylene and various solutions were tried. Reactant starvation considered.

Li et al. (2011) *(Coolant heating and heat storage layer)*	-20 °C Climate chamber Coolant pump Vacuum insulation plate (20 mm thickness) Electric heater (3.6 kW and 4.8 kW powered) 7.5 litres coolant volume	FC stack test: 128 cells stack (10 kW, graphite bipolar plates)		Stack temperature was measured with 16 thermocouples which are installed along cathode channels of stack. CT-T graphs	The lower heat conductivity coefficient of the heat storage material has lower effect on stack temperature. 4.8 kW powered electric heater warmed the stack above 0 °C in 199 s.
Henao et al. (2012) *(Electric heater, coolant heating)*	-20 °C Electric heater (700 W) Battery	FC stack test: 23 cells stack (500 W)		Power and heat flow – time graphs CT-T graphs Real time estimation graph	2 scenarios were implemented. 0.304 MJ and 0.317 MJ energy consumed in these scenarios. Energy management system was computed needed time to heating stack.
Zhan et al. (2018) *(Electric heater, coolant heating, different components heating)*	-10 and -20 °C Heat exchanger Electric heater (2 kW powered heater used, 5 LPM and 20 °C coolant circulated) Environmental chamber	FC stack test: 10 cells, each cell has 280 cm^2 active area (2 kW), 150 cells stack (30 kW) Stainless steel end plates Epoxy resin insulating plates		CT-T graphs Current density – time graphs Polarization curves	Optimal preheating method was determined as stack preheating by air and end plates (in the case of its temperature above -5 °C) Coolant heating method fast and effective, but it is time and energy consume.

Pistono and Rice (2020) *(Coolant heating, isothermal water fill)*	-20 °C Coated balsa wood insulation Kapton heat pads (electric load) Pressure film Coolant circulation	Single cell tests: 16 cm^2 Parallel coolant channels were machined to back of bipolar plate Coolant circulated at 80 °C (60% ethylene glycol/40% water) H_2 (0.5 slpm) air (0.75 slpm)	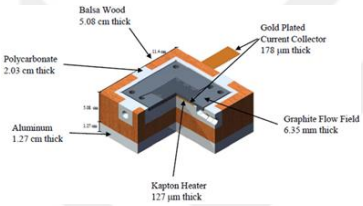	CV – CD graphs Graph of water uptake of insulation materials Pressure distribution on compression paper Polarization curves CV-T graphs	Galvanostatic start (600 mA/cm^2) showed maximum hydration of membrane within less 2 min. Isothermal water fill test has the highest water fill capacity.
Oszcipok et al. (2006a) *(Catalytic burner, electric heating foil)*	-20 °C Catalytic burner (10.7 W) Electric heating foil (11.3 W) Pump Water separator Climatic chamber	FC stack test: (30 W portable stack, 5 kW medium power applications, and 85 kW automotive applications) Whole stack parameters were given as Tables in manuscript H_2 (1.5), air (2) stoichiometry	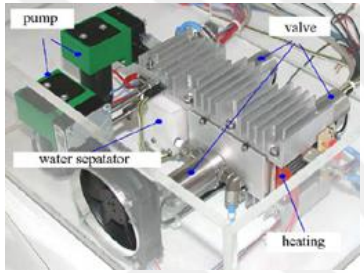	Energy consumption comparison graph I-V curves CT-T graphs CV-T graphs	Energy consumption values were obtained and compared for different cold-start methods. Electric heating assisted method was found more effective than catalytic burner.
Li et al. (2019) *(Local heating the cathode)*	-10, -20 °C (FC anode and cathode purged by nitrogen for 1h at 25 °C before cooling and 3h frozen at -10 °C) Electric load	Single cell tests: 25 cm^2 (straight channels, 1 mm width) Whole main parameters were given as table in manuscript	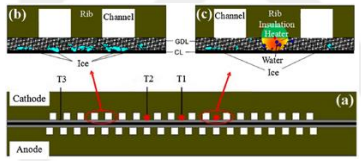	Cathode GDL surface temperature is measured by K-type thermocouples. CT-T graphs CV-T graphs I-V curves Impedance-time graphs	A local-heating was supplied by wire heaters which placed under ridges of cathode bipolar plate. The best cold start performance was obtained with one wire heating at constant heating power density.

Cho et al. (2004) *(Methanol or ethylene glycol as antifreeze)*	-10, -20 °C External humidifier Dry nitrogen and oxygen purge (350 mL/min for 20 min) Methanol, ethanol, ethylene glycol, isopropanol antifreeze solutions	Single cell test: 25 cm^2 AA H_2 (1.5), air (3) stoichiometry 1 atm operating pressure Power densities obtained at 0.6 V Performance tests performed at 80 °C		CV – thermal cycle graphs CD – thermal cycle graphs EIS graphs	Methanol, ethanol, ethylene glycol, and isopropanol solutions were evaluated as antifreeze solution for cold start. 30% methanol or 35% ethylene glycol purge-solution was found as the best way to prevent performance degradation reduces.
Knorr et al. (2019) *(Methanol as antifreeze)*	-10 °C Cooling circulator Silicon oil coolant 40% methanol-60% water solution as antifreeze agent Dry N_2 purge (500 ml/min, for 5 min)	Single cell tests: Graphite plates (5-channel serpentine flow field) Commercial 7-layer MEA (5x5 cm^2 AA)		EIS Cyclic voltammetry graphs CT-T graphs CV-T graphs SEM images	40% methanol - 60% water solution was selected as antifreeze agent. Above 80 F/T cycle was performed to show suitability of agent for tests. Performance losses were observed at high power densities, especially. Methanol should remove from the cell before start to reach nominal power.

Herein, Sun et al. (2008) and Guo et al. (2019) considered the reaction and reactor conditions (H_2 concentration and flow channel dimensions ~ *as microreactor*) and explosion probability in their studies. The catalytic reaction method can be an outstanding approach to ensure quick cold startup. Because this way is not required extra equipment and contributed to the protection of stack weight and volume. The method should easy applicable and practical especially for automotive and transportation applications, at the same time. Flow channels act as microreactors and H_2 and O_2 gases should supply from the same inlet to ensure catalytic reactions and gain useful heat. Since the inlet and outlet points of the PEMFC stack are constant, the researchers should focus and figure out in their studies how this method can practical. Not requiring extra equipment is one of the optimum features of this system. Therefore, the stack can operate with its kit without increasing the stack volume and weight. Herein, the energy and cost-effectiveness of the catalytic reaction should research and compare with the other assisted methods both thermodynamically and economically. Because the catalytic reaction approach can cope with the energy requirements of the DOE (< 5 MJ) (Website, 2021), easily.

2.2.2. Coolant Heating

The coolant heating method has some advantages such as heating source flexibility, use of different coolants, not requiring extra accessories, and flexible heating intensity. St-Pierre et al. (2005) carried out a study that researched a lot of cold start parameters. Firstly, they evaluated different heat sources by considering the reactant starvation and the methanol combustion. Reactant starvation can be a way to supply useful heat to the survival of the stack at subzero conditions and can create by the controlled change of stoichiometry (St-Pierre et al., 2005; Amamou et al., 2016). The starvation occurs with the decreasing of stoichiometry at constant current (Colbow et al., 2002) or increasing the current density at constant stoichiometry (Roberts et al., 2001), and thus the cell voltage decreases in either event. After the reactant starvation method, they operated a 10-cell DMFC stack (at

room temperature) with 0.4 or 1.5 molar (M) methanol fuel stream (St-Pierre et al., 2005), and observed the temperature increase to approximately 50 °C (with 1.5 M). Also, it was noted that the heat losses (natural convection, etc.) should be considered during startup. They applied a purging method using dry hot (85 °C) and cold (10 °C) gas at shutdown to the prevention of material degradation. In addition, water-ethylene glycol solution (50/50%), and perfluorocarbons were evaluated as a coolant and determined their physical specifications. Cold start test conditions were presented in Table 2.1 related to this research. Li et al. (2011) constituted an experimental setup to investigate the cold start ability of coolant heating and insulating materials using 120 cells 10 kW powered stack. 16 thermocouples were placed cathode channel of the stack, symmetrically. 20 mm thickness polystyrene insulators were used as a heat storage layer. Insulator succeeded to keep the stack above zero for more than 24h after shutdown at 80 °C. It was pointed out that the lower coefficient of heat conductivity of the heat storage material has a weak effect on temperature protection. They tested the coolant heating method at -20 °C cold start temperature using 7.5 liters of coolant, and an electric heater to heat the coolant. The coolant was heated to 40 and 50 °C at initial conditions. In addition, the electric heater was operated at 2.4, 3.6, and 4.8 kW powers, and investigated the effect of heater power on cold start time, too. The quickest warm-up was ensured with 50 °C coolant circulating and a 4.8 kW-powered heater, as expected. However, the energy and cost-effectiveness of the approach should evaluate when considering the coolant heating method. Therefore, the coolant heating method needs optimization in terms of energy consumption vs. heating capacity, cost-effectiveness, and also availability of the coolant. Henao et al. (2012) used 23 cells 500 W-powered stack in their experiments as presented in Table 2.1. They created a closed-loop circuit and heated the coolant (water) with 700 W of electric power. The initial stack temperature was set to -20 °C and two scenarios were implemented: The first one, the heating system operated at maximum power (700 W), and the second one their proposed time-optimal strategy. As a result, they determined 0.304 and 0.317 MJ energy

consumption during implemented scenarios, respectively. Giving the determined findings as MJ in this study makes it possible that the comparison feasibility with other similar studies. Moreover, it is necessary to remain and expand the research taking into account the energy requirements of DOE (Website, 2021) (max. 5 MJ from -20 °C).

Zhan et al. (2018) evaluated different preheating methods with five case studies for the cold start problem. They used two different stacks in their studies which first one is 10 cells 2 kW-powered, and the second one 150 cells 30 kW-powered stacks. They purged the stack with dry air after each shutdown and decreased the humidity of the outlet gas to 20-30% levels. Their preheating methods included five case studies. In case 1 (-10 °C cold start temperature), they heated dry air at 58 slpm and 30 °C temperature and introduced it into the stack. In case 2, the coolant (water and anti-freezing additives) was heated from -10 to 20 °C for 350 s by a 2 kW-powered heater, and preheated (20 °C) coolant entered the stack (-10 °C) at a 5 lpm flow rate. They heated the end plates using 250 W heating sheets and evaluated end plate and dry air heating methods together, in case 3 (-10 °C cold start temperature). In cases 4 and 5, the operation process of case 3 was repeated at -20 °C cold start temperature. Moreover, they analyzed the energy consumption of the cold starter strategies and determined the heat transfer rates of each heating method, also. The coolant heating method was pointed out not only as a fast and effective approach but also consumed time and excessive energy. In addition, the stack heating by air and end plates method was noted as the optimal preheating method. Zhan et al. (2018) study included experimental details and energy-related calculations and a very good guideway for the researchers.

Pistono and Rice (2020) constituted a test fixture (16 cm^2 active area), and insulated with coated balsa wood. They machined the coolant (60% ethylene glycol/40% water) channels (triple serpentine) into the backside of BPs and warm-up (80 °C) the coolant with Kapton heat pads (electric load). They tested cold start fixtures at -20 °C under galvanostatic and potentiostatic conditions and reported that

the heating coolant with double pads was more effective than single pad heating. Also, the potentiostatic start-up (0.1 V) was found more useful. There are several patents related to the coolant heating approach (Fuller and Wheeler, 2000; Doctor et al., 2003; Couch and Sribnik, 2004; Lin, 2006; Skiba, 2006; Lin, 2009; Roberts et al., 2009).

Indeed, the coolant heating method is pretty useful and practical in terms of carried energy density, uniform heat distribution, and short start-up time (Zhang and Kandlikar, 2012). One advantage of this way is that not required extra equipment and coolant can be heat-up from any energy source such as a battery (Henao et al., 2012), electric heater (Li et al., 2011; Zhan et al., 2018), heat pad (Pistono and Rice, 2020), and also the waste heat of engine (in hybrid applications which both FCV and internal combustion engine). However, this heating source flexibility brings along some problems such as over-energy consumption, fixture complexity, etc. Thus, an energy management system or energy consumption optimization should consider to find out the cost and energy efficiency of the proposed coolant heating method. When carrying out this, the same energy units may be preferred for comparison with another study. In this regard, Joule or MJ units assigned by DOE (Website, 2021) can consider as shutdown and startup energy units (<5 MJ) for the cold start.

Start-up time decreases in the case of liquid cooling or heating system preferred since the specific heat capacities and heat transfer rates of liquids are pretty much higher than gases (Incropera et al., 2006; Ramezanizadeh et al., 2019; Quoc and Shabani, 2020). In the PEMFC system, deionized water is used as a coolant in general, and the water cooling system is the most preferred cooling strategy, especially in high-power stacks (Zhang et al., 2012). Besides, nanofluid adoptions in PEMFCs as alternative coolants were reviewed by Zakaria et al. (2015) and Bargal et al. (2020). On the other hand, the ethylene glycol/water mixture is the most widely used coolant at subzero operations (Zhang et al. 2012). Moreover, there are different coolants apart from ethylene glycol/water favorable to the cold start process, and these coolants which exist in the literature were presented in Table 2.2. In addition,

patents were made and various materials including glycerol, propylene glycol, and ethylene glycol were mixed with deionized water in different percentages by volume (Mohapatra, 2006; Maes and Lievens, 2007). These mixtures were evaluated in terms of electrical conductivity. Because the coolant should insulator to inhibit current leakage through the coolant loop and performance degradation in the stack (Zhang et al., 2012).

Table 2.2. Properties of coolants used in PEMFCs

Coolant	**Melting point (°C)**	**Boiling point (°C)**	**Density ($g.cm^{-3}$)**	**Specific heat capacity ($J.g^{-1}.°C^{-1}$)**	**Ref.**
Water	0	100	1	4.2	St. Pierre et al. (2005)
Water/ethylene glycol (50/50%)	-36	110	1.05	3.47	Cho et al. (2004), St. Pierre et al. (2005)
Perfluorotributylamine	-57	155	1.87	1.1	St. Pierre et al. (2005)
Perfluorotriamylamine	-25	215	1.93	1.1	St. Pierre et al. (2005)
Perfluorocyclicether	-110	97	1.78	1.1	St. Pierre et al. (2005)
Kerosenic hydrocarbon	-35	85	-	2.5	Elhamid et al. (2004)

In this circumstance, a coolant optimization idea can be speculated. Because the viscosity, electrical conductivity (or resistivity), specific heat capacity properties of each coolant are different. Therefore, cold start characteristics, capacity, and ability of each coolant will be different. Thus, the effectiveness of the coolant heating

method should improve considering the cost and energy optimization of the coolant and its application style. Furthermore, heater and pump powers which are required for the heating and circulation of the coolant should incorporate in energy calculations.

2.2.3. Electric Heating

Fast response time, flexible power control, and multiplicity of employment way superiorities are the primal benefits of the electric heating method on the complicated strategies. Two active heating methods were compared which are catalytic burner and electric heating foil by Oszcipok et al. (2006a). They used a 30 W-powered stack which has a 30 cm^2 cell active area, and compared the energy efficiencies of catalytic burner plate (10.7 W) and electric foil (11.3 W) at -20 °C. The electric heating foil which was heated by the battery was placed into the bipolar plate. It was reported that the electric foil (4.5 Wh consumption) assisted cold start is more effective than the catalytic burner (above 20 Wh consumption) when the stack reached 0 °C. Li et al. constituted an experimental setup and investigated the effects of MPL hydrophobicity (Li et al., 2019), clamping stress (Li et al., 2019a), and local heating method (Li et al., 2019b) on the cold start performance of PEMFC. Their third study (Li et al., 2019b) is a guide specifically for the electric heating method. They used a 25 cm^2 active area single stack and placed heating wires (0.15 mm in diameter, CrNi material) into the cathode bipolar plate ribs to heat the GDL locally. For this purpose, the BP rib width was set to 2 mm, and wire heating holes (3 holes at the center of the active area) were fulfilled with heat insulation material. Therefore, local heating of the stack was ensured, and the performances of one-wire heating and three-wire heating methods were compared. Cold start tests were carried out at -10 °C (at 47.0, 52.2, and 60.6 W/kg heating power densities), and -20 °C (at 365.0 and 438.0 W/kg heating power densities). H_2 and air were cooled until test temperature before passing into the stack thanks to cooling coils placed into the conditioning cabinet. Their single-cell stack design and experimental details were

demonstrated in Figure 2.3 and Table 2.1, respectively. One-wire heating was found better than three-wire heating at constant heating power density. Also, successful cold starts were achieved at -10 and -20 °C with higher heating power densities.

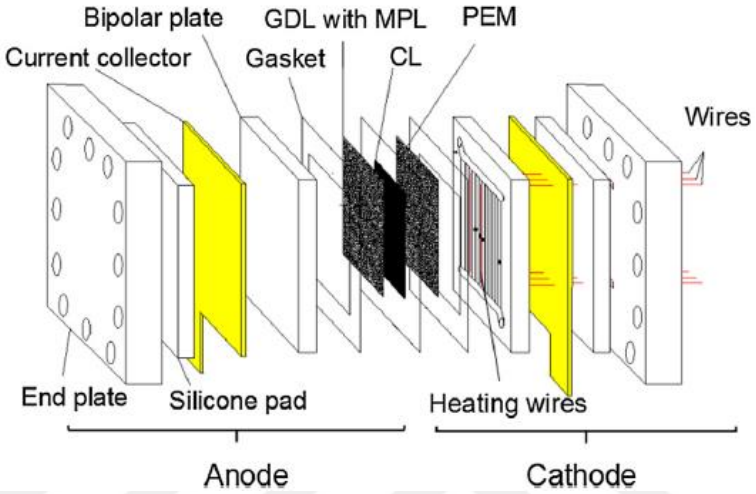

Figure 2.3. Single-cell design for local heating by heating wires (Li et al., 2019b)

A patent (Matsuoka, 2006) was made with similar operation logic by Li et al., 2019b. Other patents related to the electric heating method are presented in Reiser, 2004; Matsuoka, 2006 and Ryu et al., 2012. The battery is used as a power supply in the electric heating method usually. Indeed, other assisted methods use electricity to heat the stack as a primary supply. Because other methods use electricity with the intention of supplying energy to run another source. For instance, the stack warm-up is thanks to coolant although electricity uses to drive the pump and heater in the coolant heating method. On the other hand, the electric heating method requires an external power supply that increases the total weight and volume of the system. Besides, the approach needs insulator materials to hinder the short circuit that can cause leakage of electricity and performance degradation.

2.2.4. Antifreeze Agent

Antifreeze agent application to the anode and the cathode sides is another assisted cold start approach and it is similar to the keep warm strategy logically.

Because antifreeze matter which has low freezing point supplies to the flow channels, and water freeze avoids, in this method. Correlatively, the keep warm strategy aims that keeps the stack above zero, and therefore both procedures maintain similar perspectives.

Cho et al. (2004) compared gas purging and solution purging methods at subfreezing temperatures (-20 °C) and they evaluated the water solutions of methanol (30%), ethanol (30%), ethylene glycol (35%), and isopropanol (47%) as antifreeze matters. They used a 25 cm^2 active area single cell stack in their tests, and fed dry N_2 and O_2 gases to the stack at 350 ml/min for 20 min in the gas purging method. Ethanol and isopropanol solutions were disqualified due to bringing about a noticeable swell in membrane thickness. Ethylene glycol and methanol antifreeze were removed from the cell by supplying the H_2 and O_2 gases to the anode and the cathode, respectively. The performance degradation rate was reduced with the solution purging method, and it was reported that the solution method (several seconds) was more effective than gas purging (20 min). A similar but more comprehensive study was carried out by Knorr et al. (2019). They assessed methanol-water solution (40% methanol) and compared it with conventional dry gas purging using single-cell stack (25 cm^2 AA commercial 7-layer MEA, 5-channel serpentine flow field graphite BP). Besides, their test equipment has a silicon oil coolant system. The cell was cooled to 40 °C using dry N_2 (500 ml/min to the anode and 1000 ml/min to the cathode) for 5 min after operation and shutdown at 80 °C according to dry gas purging protocol. On the other hand, the cell was cooled to 20 °C using dry N_2 (500 ml/min to the anode and the cathode) for 5 min, and the antifreeze was filled the anode and cathode sides in compliance with the antifreeze protocol. The antifreeze was removed by N_2 purging and flushing DI water (5-10 min). F/T cycles were performed 94 times in the range of -10 and +20 °C. The antifreeze application reduced performance degradation as compared to the gas purging method. Afterward, they performed a cold start analysis considering the three different operating modes at -10 °C. Firstly, the cold start test was carried out

in DMFC mode since methanol is available in the cell, but this mode was found unsuitable, and significant activation losses were observed due to methanol oxidation and methanol cross-over. Secondly, cold start tests were applied in PEMFC mode and the antifreeze was removed by N_2 purging and the anode and the cathode were fed with 226 ml/min dry H_2 and 624 ml/min dry air, in this mode. In the third mode, they carried out the same protocol as the second mode without removing the antifreeze. They reported that the residual methanol reduced the power density and it should be removed from the cell to reach nominal power.

Antifreeze implementation can be an alternative solution for cold start operations by virtue of low-cost, practicality, and easily applicable. However, antifreeze solutions (especially alcohol-based) may damage the stack materials (swell the membrane and reduce durability), cause performance degradation, and cold start failure. Besides, research on this approach is limited availability. Hence, the method needs to improve considering the damage and durability characteristics of the MEA.

2.2.5. Energy Consumption Units for Assisted Cold Start

Start-up and shutdown energy consumption limits were assigned as 5 MJ (from -20 °C) for the cold start process in 2020 (ultimate) targets of the DOE (Website, 2021) (80 kW FC systems operating on direct H_2). Other institutions which are FCH JU (Website, 2022), MOST (Website, 2016b), and NEDO (Website, 2010) did not determine a specific energy limit for the cold start yet. Cold start time (from -20 °C) which is set to 30 seconds can be achieved with various assisted methods as mentioned above. However, the energy consumption of the applied approach is as crucial as the cold start time. Because the consumed energy amounts of each technique are different to heat the stack, and thus energy balance and optimization researches are vital in terms of cost and energy efficiency of the methodology. Consumed energy amounts were given with various units in many of the studies presented above as seen in Table 2.3.

Table 2.3. Energy consumption units of the assisted methods

Assisted Cold Start Method	Manner of Application	Energy Consumption Unit	Ref.
Electric heating	11.3 W electric heating foil	Wh	Oszcipok et al. (2006a)
Catalytic burner	10.7 W catalytic H_2 burner	Wh	Oszcipok et al. (2006a)
Catalytic reaction	H_2 and O_2 fed	ml	Sun et al. (2008)
Coolant heating	2.4 and 4.8 kW electric heater	kW	Li et al. (2011)
Gas heating	Dry N_2 and O_2 at 350 ml/min for 20 min	ml	Cho et al. (2004)
Coolant heating	700 W electric heater	MJ	Henao et al. (2012)
Gas heating	Dry air at 58 slpm for 1850 s	slpm	Zhan et al. (2018)
Coolant heating	5 lpm flow rate and 2 kW heater	kW	Zhan et al. (2018)
Electric heating	250 W heating sheets for 180 s	W	Zhan et al. (2018)
Gas/Coolant/ Electric heating	All cases were presented in a Table with kJ unit	kJ	Zhan et al. (2018)
Catalytic reaction	H_2 and air fed	J	Guo et al. (2019)
Antifreeze agent	N_2 purging, DI water flush, H_2, and O_2 fed	ml	Knorr et al. (2019)
Electric heating	Wire heating with different heating power densities	W/kg	Li et al. (2019)

Some preferred consumption units are Wh (Oszcipok, 2006a), ml (Cho et al., 2004; Sun et al., 2008; Zhan et al., 2018; Knorr et al., 2019), W (Li et al., 2011; Zhan et al., 2018), J (Henao et al., 2012; Zhan et al., 2018; Guo et al., 2019), and W/kg (Li et al., 2019b). ml or slpm units were used frequently when evaluating the gas heating or catalytic reaction and catalytic burner (Cho et al., 2004; Sun et al., 2008; Zhan et al., 2018; Knorr et al., 2019). On the other hand, W or J units were

chosen when conducted coolant or electric heating methods (Oszcipok, 2006a; Li et al., 2011; Henao et al., 2012; Zhan et al., 2018; Guo et al., 2019). The use of similar units is pretty substantial to the comparability and intelligibility of the proposed techniques. Hereby, the prominent or drawback sides of the approaches can be disclosed with the checking of energy consumption levels. Zhan et al. (2018) compared energy consumption amounts of different preheating methods using only kJ units although they researched air heating, coolant heating, and electric heating methods together. In other respects, an electric heater was used to warm-up the coolant at the aforementioned time (Li et al., 2011). Here, Wh unit can be achieved considering the electric heater power and operated duration, and therefore can be comparable to research by Oszcipok (2006a). Nonetheless, a complete and drastic comparison is not possible among the consumption of the methods. Because some studies were carried out using single-cell (Cho et al., 2004; St. Pierre et al., 2005; Sun et al., 2008; Knorr et al., 2019; Li et al., 2019b; Pistono and Rice, 2020) or low-power stack (Oszcipok, 2006a; Henao et al., 2012; Guo et al., 2019) while the others were conducted at the stack level (middle or high power) (Oszcipok, 2006a; Li et al., 2011; Zhan et al., 2018). Undoubtedly, the energy requirement levels of the single-cell and the stack are different and incomparable. At this point, it may be more beneficial to use comparative units such as W/kg to eliminate this confusion (Li et al., 2019b).

2.3. Unassisted Cold Start

Indeed, PEMFC stacks are assembled for normal operating conditions (65-75 °C). Cold start requirements appeared later. Thus, researchers and engineers focused on normal operating conditions to achieve better performance at first, naturally. But, after reaching a certain contentedness in this regard, start-up ability from the subfreezing temperature had come into prominence towards the end of the 1990s. Developments accelerated with improvements and optimizations on material and approach for cold start capability. The ultimate unassisted cold start temperature

was assigned as -30 °C by DOE (Website, 2021). Surely, reaching these temperature levels is easier with the assisted approaches. Nevertheless, assisted cold start requires several outfits in many situations although it is much fast and feasible. Therefore, self-heating (unassisted) operation achievements are crucial for the weight, volume, energy, and cost-effective FC stack.

Unassisted cold start can achieve by the optimizations of the stack components and the operating conditions. Researchers, first, developed the stack material and controlled its convenience for the cold start process. And, the optimum operating conditions of the modified material were tested to ensure maximum benefits for the cold start. In this case, it should not be forgotten that the advances in materials should not increase the stress level of the components, lead to material degradation, and a decrease in performance.

2.3.1. Optimization of the Stack Components

The main components of the PEMFC stack and MEA structure details are illustrated in the previous section in Figure 1.3. The characteristics and performance of each component have effects on the cold start behaviour, separately. Nonetheless, a successful cold start can not be possible through the optimization of all components. Made effort to reach an optimized stack structure for the cold start can result in different concerns such as durability, degradation, and a decrease in performance at normal operating conditions. For instance, using insulator materials can provide an advantage in the cold start capability (Sun et al., 2008; Li et al., 2011; Sasmito et al., 2013; Li et al., 2019). At the same time, this employment will increase the cooling load of the system at normal conditions due to its conservative structure. As understood, it is not possible that the full optimization considers the whole elements of the stack. Thus, each component should scrutinize itself. Studies on the optimization of stack components are summarized in Table 2.5. Experimental details, test conditions, and findings of each component are presented and discussed in subsections.

2.3.2. MEA Components

Although the MEA is one of the main FC components, it also consists of many layers. The MEA elements have been shown in Figure 1-b. An MEA comprises a polymer membrane, anode, and cathode catalyst layers, micro-porous layers, and gas diffusion layers. The MEA productivity is vital for the stack power and the FC performance is known with the capability of the MEA, commonly. Therefore, a successful self-cold start can achieve through the improvement of the MEA components.

2.3.3. Membrane

Oszcipok et al. (2006b) investigated the effect of the thickness and humidification level of the membrane on cold start ability. It was stated the membrane should not be too dry. Also, they could not determine the influence of membrane thickness clearly because their performed statistical regression analysis is not allowed to reveal this due to the high GDL porosity.

The effect of the water absorption capacity and initial hydration level of the membrane was investigated by Nicotera et al. (2009) and Mishler et al. (2013), respectively.

Table 2.4. Summary of material optimization cold start studies and details (sorted by published date and main assist type)

Reference and Main Assist Type	Cold Start Temperatures and Test Equipment	FC Test Conditions	Schematic (Configuration)	Obtained Values and Figures	Major Observations
Oszcipok et al. (2006b) (*Membrane thickness, different GDL types, effect of gas flow rate, humidification level of membrane*)	-10, -20 °C Test bench is controlled by LabView Climatic chamber 18, 25, 35 µm membrane thicknesses GDL (190 µm thickness),MPL, OAC, OCC GDL	Single cell tests: 46 cm^2 Graphite BP Titanium end plates Plastic cooling plates Styrodur isolation material 220 H_2 and 600 ml/min air	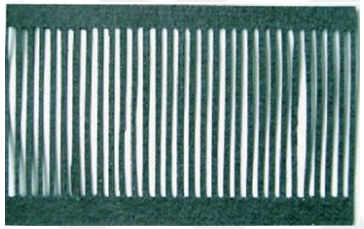	Cell impedance Current curves – at different operating conditions CD – GDL type graphs CT - V graphs Waste heat – V graphs	The gas flow rate and humidification level of the membrane were experienced. It was reported that the membrane should not be too dry, and a high air flow rate is needed.
Nicotera et al. (2009) (*Membrane water absorb capacity*)	-50 °C Nafion-based membranes Thermal cycles in the range of -50 to 25 °C DSC NMR	Filler-free Nafion membrane Nafion/SiO_2 and Nafion/$Zr(HPO_4)_2$ composite membranes	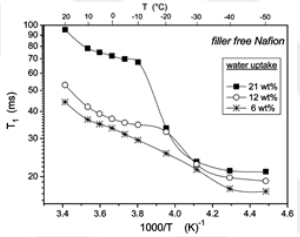	DSC graphs Arhenius plot NMR graphs	The membranes were found still active to proton delivery at -50 °C. Lower water uptakes (~10 wt%) can eliminate the limitation of the transport.
Mishler et al. (2013) (*Various membranes, initial hydration level, catalyst thickness, ionomer-carbon ratio)*	-10, -20 °C Coolant used to reduce the temperature to sub-zero Nafion (NR211, NR212) Dry nitrogen purge at 1 L/min for 2 min.	50 cm^2 AA Operate at 0.02, 0.04, 0.08 A/cm^2 current densities 500 sccm dry H_2 and air stoichiometry 25 psi back pressure	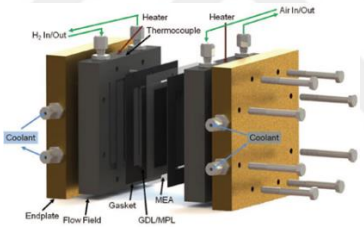	I-V curves CV-T graphs Coulombs transfer – current density graphs HFR-T graphs	A better hydrated membrane (50% vs. 100% RH) performed better conductivity.

Thompson et al. (2008) *(CL water storage capacity)*	-8, -10 °C Impedance spectrum record with 50 sccm H_2 to the anode and 50 sccm N_2 to the cathode	50 cm^2 AA 25 µm Nafion membrane 50/50 sccm H_2/O_2 0.01, 0.05, and 0.1 A/cm^2 CDs	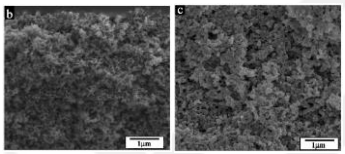	CV-time graphs Cryo-SEM images Charge stored – CD graphs	The charge storage utilization is controlled by CD and is less dependent on initial water content or electrode thickness.
Miao et al. (2010) *SiO_2 addition to the CL)*	-8, -10 °C 8 cold start cycles 30 ml/min H_2 and O_2	4 cm^2 AA SiO_2-doped MEA Nafion 212 membrane	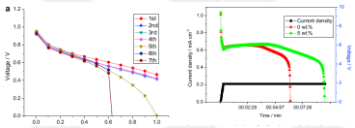	CV-CD graphs CV-time graphs CD-time graphs Impedance measurements ECA vs. cold start cycle graph	Results proved the cold start process was strongly related to the cathode water storage capacity.
Nandy et al. (2010) *(CL thickness – pore volume study)*	-10, -20, -30 °C Both sides were purged with dry N_2 for 2 min 400 mL/min H_2 900 mL/min air 40 and 100 mA/cm^2 start-up current densities	Catalyst-coated membranes (CCM) were made by spray-depositing catalyst ink onto Nafion 2012 40% Pt/C Different CL thicknesses 5 cm^2 AA Graphite BP	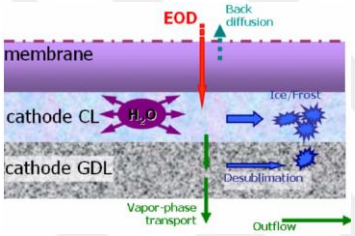	CV-time graphs Ice fraction – time graphs Water content – time graphs CT-time graphs	CL thickness (pore volume) effect on cold start performance was explored. Thick (above 20 µm) CL is required for a successful start from -30 °C.
Liu et al. (2021a) *(Electrospun catalyst layer)*	-10, -20 °C 1000 sccm N_2 purge 140 sccm H_2 330 sccm air 25 cm^2 AA Graphite BP with serpentine FF Nafion 211 membrane	E-spun ink: 4.7% Pt/C 14.1% DI water 23.5% Isopropanol 56.3% Nafion 1.4% PAA	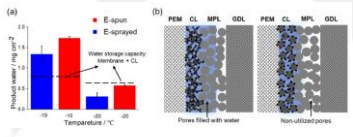	SEM TEM I-V curves CV-time graphs	E-spun CL exhibited a better cold start capability in terms of more condensed product water due to the longer survival time.

Han et al. (2011) *(GDL study)*	-10 °C 5-cell stack Thermocouples were placed to macro-porous substrate side of GDL and cathode BPs 1.5/2 H_2 and air stoichiometry 1500 mA/cm^2	426 µm thickness GDL Pt loading 0.4 mg/cm^2 cathode Metallic BP with parallel FF by stamping process FF depth 1.7 mm and 1.3 mm for anode and cathode 0.8 mm FF width		SEM images I-V curves CV - time graphs CV-CD graphs HFR-cycle graphs Pressure measure EDX spectra	Effect of anisotropic bending stiffness of the carbon fiber-felt GDL on the degradation behavior of PEMFC under temperature cycling between -10 and 1°C investigated.
Hirakata et al. (2013) *(GDL study)*	-5, -10 °C 0.05 A/cm^2 Single-cell was tested Humidified N_2 purge Dry H_2 and dry air with unknown flow rates	Nafion 211 membrane NRE 212 membrane 100 ml/min H_2, 150 ml/min N_2 to the anode and cathode		CV-CD graphs CV - time graphs Pressure measure CT - time graphs Resistance - time graphs	The effect of pore diameter of the GDL was investigated. Both cells failed to start up at −10 °C, and no differences in the performance of both cells were observed.
Dursch et al. (2013) *(GDL study)*	1, 2.5, 5, 10, and 25 K/min heating rates 20 mL/min N_2 purge	TGP-H-060carbon paper GDL 20% and 85% liquid-water saturations were studied.		DSC analysis Capillary-pressure saturation measurements	Ice-melting endotherms and ice-melting times as functions of heating rate in a fuel-cell (GDL) using non-isothermal DSC determined. Large pore diameters do not alter the equilibrium melting temperature of ice within GDLs.

Wang et al. (2019) *(MPL study)*	-4.2, -10 °C 1000 sccm N_2 purged to the anode and cathode for 1.5 h 95 sccm H_2, 226 sccm air flux 0.04 A/cm^2 operating current density	Hybrid MPL structure 5x5 cm2 AA Nafion 212 SGL 29BC MPL 10 mm thick cathode BP 1 Nm assembly torque		SEM images I-V curves CV - time graphs Cell Resistance – time graphs CT - time graphs Pressure drop – time graphs	Hydrophilic/hydrophobic stripes were arrayed alternately in plane direction of MPL. Liquid move to hydrophilic area occurred by liquid exclusion of hydrophobic
Rajbongshi et al. (2020) *(MPL study)*	-5,-8,-10,-15, -20 °C Small performance decay after the 6th freeze/thaw cycle 120 ml/min H_2, 220 ml/min O_2	Pt/C (40%) Pt loading 0.5 mg/cm^2 Nafion 115 membrane MPL coated carbon paper 4.4 cm^2 AA		I-V curves CT - time graphs Freeze/thaw – temperatures cycles CV - time graphs CD – CV graphs EIS graphs Cycle – ECSA FE-SEM images	Studied performance decay of MEA in freeze/thaw and sequential cold start cycle. The performance degradation may be due to the loss of hydrophobicity of MPL coated GDL.
Li et al. (2021a) *(MPL study)*	-10, -15 °C 40 mA/cm^2 constant CD in cold start tests 300 sccm N_2 purge to anode and cathode 100 sccm H_2, 150 sccm air	Electrospun MPL Pt/C (40%) Pt loading 0.25 mg/cm^2 cathode Mafion 211 membrane Graphite BP with serpentine FF		SEM images Water contact angle diagrams CD – CV graphs EIS graphs CV - time graphs	Cold start performance comparison of the electrospun MPL and the conventional one.
Qian et al. (2022) *(MPL study)*	-10 °C 10 mm thick graphite BP with thermocouple Parallel FF, 0.5 mm width, 0.3 mm depth 95 mL/min H_2, 226 mL/min air	PPS-MPL, PPS-PTFE Nafion 212 Pt loading 0.6 mg/cm^2 cathode SGL 29BC GDL 5x5 cm^2 AA		SEM images EIS graphs Porosity measure Water contact angle diagrams I-V curves CV - time graphs	The PPS-MPL shows better cold start performance than PTFE-MPL.

Santamaria et al. (2013) *(Flow field -FF study)*	-4, -6, -8 °C 420 µm SGL 10 BC GDL with MPL Nafion 112 MEA Silicon gaskets 2 SLPM N_2 gas purge for 600 s Temperature follows from 6 thermocouples	Aluminium alloy BP, Ni coated 30.5 cm^2 AA Galvanostatic starter technique 200, 400 mA/cm^2		CV - time graphs CD – CV graphs CT - time graphs Waste heat – time graph	Parallel and interdigitated flow-field comparison at various current densities. Interdigitated flow-field may provide better performance under less extreme cold-start conditions
Huo et al. (2017) *(Metal foam – FF study)*	-4, -6, -8 °C Thermocouple placed middle of cathode BP 2 SLPM N_2 gas purge 0.2 SLPM for anode, 0.3 SLPM for cathode	Parallel 1x1 mm^2 FF design 1.5x20 cm^2 AA Nafion 112 DuPont membrane Nickel foam FF vs. Parallel FF		CD – CV graphs I-V curves CV - time graphs Pressure drop – time graphs CT- time graphs	Galvanostatic and potentiostatic start control techniques. Metal foam is superior to the conventional parallel FF under galvanostatic control MF produces slightly lower power than parallel at low current operation.
Zhu et al. (2019b) *(Different cathode serpentine FFs)*	-5, -10, -15, -30 °C 0.4 and 0.6 V constant voltage operating 1.5 and 2 L/min N_2 purged to the anode and cathode, respectively 0.6 L/min H_2 and 1 L/min air 0.1, 0.2 and 0.3 V constant voltage operating	FF width/depth 1 mm Graphite BP 49 segment PCB		FF – velocity distribution FF – pressure distribution CT- time graphs CD - time graphs I-V curves	2 to 1 serpentine flow field has the best cold start performance and the best current density uniformity when cold start at constant voltage mode above -5 °C.

Nicotera et al. (2009) reported that the Nafion-based membranes are still active on the proton transport at -50 °C. It was noted that the proton transfer was carried out limited in high water uptakes while it can be eliminated when the water content is lower than 10 wt%. On the other hand, Mishler et al. (2013) indicated that a better-hydrated membrane (50% vs. 100% RH) performed greater ionic conductivity. But the difference was found negligible. Moreover, they researched the effects of the Nafion membrane types (NR-211, vs. NR-212), membrane thicknesses (25 vs. 50 μm), and ionomer/carbon black (I/C) ratios (0.33, 0.5, and 0.66). The thick membrane was pointed out to have a larger capacity because of the extra ice store space than the thin membrane and the 0.5 I/C ratios exhibited larger Coulombs of charge capacity. This study is one of the most comprehensive research in terms of the optimization of the membrane parameters for the cold start ability.

2.3.4. Catalyst Layer

Catalyst layer, another important component of the MEA, is the heart of the electrochemical reactions which consist of mainly Pt/C materials. Indeed, one of the most significant challenges is derived from this point: The expensive platinum catalyst requirement. The existence of a Pt/C ratio with a high percentage in the MEA structure both increases the performance and total cost. Therefore, studies on the reduction of Pt ratio in the ionomer have vital importance on behalf of cost-effective MEA production. Liu et al. (2021a) produced electro spun (E-spun: 4.7% Pt/C, 14.1% DI water, 23.5% isopropanol, 56.3% Nafion, 1.4% PAA) CL and investigated its characteristics under normal and cold start conditions. It is stated that the E-spun CL exhibited superior output under normal and sub-zero temperatures owing to its lower mass transport losses and more condensed product water rate. In another study, Nandy et al. (2010) investigated the CL thickness (pore volume) effect on the cold start performance of the PEM fuel cells. Ultrathin (1 μm), 10 μm, and 20 μm CL thicknesses were evaluated and it is reported that the importance of thick CL usage (above 20 μm) at harsh (-30 °C) conditions. In addition, a successful cold start

operation was achieved with 10 μm CL at 100 mA/cm^2 from -20 ℃. In other and similar CL studies, the effect of the electrode and membrane water storage capacities by Thompson et al. (2008) and hydrophilic nano-oxide SiO_2 addition into the cathode CL by Miao et al. (2010) were investigated. Experimental details on the cold start tests and main conditions are presented in Table 2.5.

2.3.5. Gas Diffusion Layer (GDL)

Oszcipok et al. (2006b) carried out a highly interesting study and compared the cold start capacities of the conventional GDL with the GDL modified by open anode channels (OAC), open cathode channels (OCC), and microporous layer (MPL). To obtain OAC and OCC GDLs, GDL was cut in a way, which was similar to the parallel flow field, and therefore the electrode surface was exposed to the gas stream, directly. The cut GDL image can be found in Table 2.5. They carried out cold start experiments at -10 °C and remarked that better water removal and higher charge transfer were ensured with the high GDL porosity. Han et al. (2011) investigated the anisotropic bending stiffness of GDL layers on degradation behaviour under temperature cycling between -10 and 1 ℃. They reported that lower HFR values were much more effective in durability improvement than gas pressure difference. In other studies, Hirakata et al. (2013) and Dursch et al. (2013) studied the effects of pore diameter and non-isothermal ice melting in GDL, respectively. The detailed examination of these studies is illustrated in Table 2.5.

2.3.6. Micro-Porous Layer (MPL)

Micro-porous layer (MPL) can be a key component for a successful unassisted cold start operation. Water particles are occurred and are frozen between GDL and MPL particles, mostly. Wang et al. (2019) investigated the effect of planar-distributed wettability of MPL on the cold start performance of the PEM fuel cell. They arrayed the hydrophilic and hydrophobic rows in the in-plane direction of the MPL component and aimed to water movement from hydrophobic to hydrophilic

region by the effect of capillary pressure. In a conclusion, a novel structured hybrid MPL was found much success in terms of continuous operation until shutdown without performance degradation. Rajbongshi et al. (2020) investigated the MPL-coated GDL effect on the freeze/thaw cycles. They noted that a low-performance drop is experienced at -10 ℃ operation. In addition, the contribution of the loss of the hydrophobicity in GDL on the performance decay with cycles is concluded. Li et al. (2021a) investigated the electro spun MPL effect, Qian et al. (2023) investigated hydrophobized MPL by polyphenylene sulfide performance in the cold start process, and Lin et al. (2021) optimized the MPL. The details related to the studies are demonstrated in Table 2.5.

2.3.7. Bipolar Plates

Santamaria et al. (2013) compared the cold start performances of the parallel and interdigitated flow fields under galvanostatic operating conditions (200 and 400 mA/mm^2). They used aluminium alloy BPs with 30.5 cm^2 AA and performed cold start tests at -4, -6, and -8 ℃ cold start temperatures. The interdigitated FF performed higher performance than the parallel one under lower current density cases at -4 ℃ (due to its water removal capability). In another study, Huo et al. (2017) compared the cold start performances of the metal foam and the conventional parallel flow field patterns. The cell temperatures were followed by thermocouples placed on cathode BPs and the cold start tests were conducted at -4, -6, and -8 ℃. Both galvanostatic (constant current) and potentiostatic (constant voltage) control strategies were applied and the metal foam was found much more successful under galvanostatic operation. Besides, it is stated that the metal foam produced slightly lower power than parallel at low current operation.

In a series of studies, Zhu et al. (2019b) evaluated different serpentine flow configurations as cathode BP and diverse cathode flow fields (Zhu et al., 2021). In addition, Yue et al. (2022) conducted on parallel FF specifications and Biesdorf et al. (2015) performed an active area dependence capability study. Flow field studies

(as well as bipolar plate studies) highly depend on the operating conditions of the cell and the estimation of the best flow field configuration is very hard due to the flexible, variable, and dynamic operating nature of the PEM fuel cell.

2.3.8. End Plates

End plates called compression plates are used for the assembling of the cell components. They are made of stainless steel (SS) or strength material, in general. The effect or significance of the end plates is not well discussed in the literature in terms of cold start capability. Wan et al. (2021) studied the effect of end plates on cold start performance considering the current density distribution, temperature variation, and pressure values at inlet and outlet sections. Low starting voltage (high current density) was found helpful to obtain quick temperature increase. Also, a high inlet gas flow rate enables to discharge of supercooled water from the MEA.

An unassisted cold start operation is hard when compared to an assisted one. Because both stack components and operating conditions should be optimized. In addition, optimized specifications should not decay performance at normal operating temperatures. Therefore, a fresh heat supply from an external source is easy and logical to achieve a successful cold start. DOE set the cold start temperatures from -30 and -40 ℃ for unassisted and assisted techniques, respectively (Website, 2021). That means the ultimate (-40 ℃) target can be achieved by only assisted techniques.

Assisted techniques are discussed in the previous section and the most powerful approach is assigned as the coolant heating method owing to its high heat capacity, homogeneous temperature distribution, and quick warm-up characterization. Another significant feature of the preferred method is the minimization of the MEA degradation since no contact between the approach and the cell active area. There is no charge to the MEA during the warm-up profile, and therefore, the effects of the assigned way on the cold start performance are negligible.

Indeed, this subject is not investigated and discussed in the literature sufficiently and effectively. The performed studies are relatively older than the other approaches. The exclusive features of the application are ignored and neglected due to the negative sides (mostly high energy requirement). That means the approach leads to overconsumption unless provided with an efficient energy management system. A working fluid (heating fluid – coolant) needs to be heated and driven to the stack to increase cell temperature. Hence, the heating mechanism should be equipped with a pump and a heater to satisfy these requirements. However, the power level of the heater is very high (in general) and overuse of this component may be induced excessive energy consumption, easily. This is the most important handicap of the way, and a thermal management system is essential to solve energy needing and provide low-energy-required and efficient heating provided applications.

In this thesis study, the operating duration effects of the external heating mechanism were considered and optimized at sub-zero temperatures using a single-cell stack. The effectiveness level of the heating system equipment was specified considering the energy consumption levels. The advantages and the disadvantages of the equipment were identified with the cold start experiments conducted in the range of -10 and -30 °C. The temperature, current, and voltage profiles of the experiments were followed, recorded, and compared to assign the most efficient heating strategy.

3. MATERIALS AND METHODS

All materials and methods used for equipment manufacturing processes are described and explained in detail with sub-sections. Firstly, BP design and fabrication steps are presented. Then, the auxiliary equipment for the short stack is given in detail. Even after, assisted external heating mechanism and its components are illustrated and the MATLAB code for the temperature picturization is depicted.

3.1. MEA Specifications

In this thesis study, commercially available MEAs were purchased from Fuel Cell Store, USA (Website, 2023c) and used in the tests. Two different active areas that 22x22 mm^2 and 50x50 mm^2 H_2-air MEAs were bought, but only 50x50 mm^2 MEAs were preferred in the tests. Because the effectiveness of all components and parameters is much more visible in large-scale works. MEAs are produced as a five-layer (GDL-CL-membrane-CL-GDL) structure. The purchased MEA and its dimensions are presented in Figure 3.1. The cell active area (AA) is 50x50 mm^2 and the whole membrane area is 100x100 mm^2 as seen in the figure.

All technical specifications of the MEA from the manufacturer company are also provided in Table 3.1 (Website, 2023c). The membrane type is Nafion 212, and the thickness is ~50 μm. Anode and cathode Pt/C loading is equal and 0.5 mg/cm^2. GDL type is carbon cloth with MPL and its thickness is 410 μm.

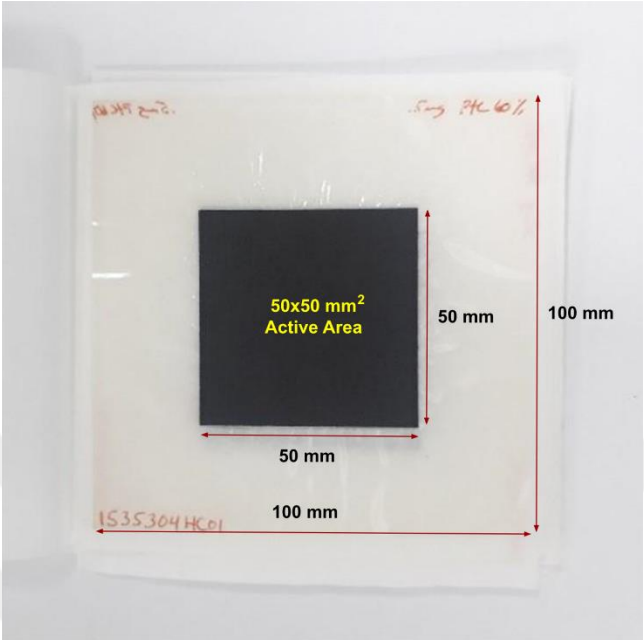

Figure 3.1. Purchased MEA, its dimensions, and cell active area

Table 3.1. Specifications of the purchased MEA

MEA type	Hydrogen air FC
Membrane type	Nafion™ PFSA NR-212
Membrane thickness	50.8 µm
Anode loading	0.5 mg/cm^2
Anode catalyst	60% in wt. Pt on Vulcan (Carbon)
Cathode loading	0.5 mg/cm^2
Cathode catalyst	60% in wt. Pt on Vulcan (Carbon)
GDL	Carbon Cloth with MPL
GDL type	Woven Carbon Fibre Cloth
GDL thickness	410 µm
Active area	50x50 mm^2
Whole membrane area	100x100 mm^2

3.2. Design and Fabrication of Short Stack Equipment

A stack should be designed and used in the cold start tests. As known, the stack dimensions may be changed from Watts to kiloWatts depending on the application areas. Therefore, a single-cell (short) stack is preferred in this thesis

considering the limited budget. At this step, the author had to take into financial support for the study and the rising exchange rate of the dollar in recent years.

3.2.1. Dual BP Design

One of the most important and distinctive features of the study is the dual BP design for gas and liquid circulation, separately. Thus, it allows internal and external gases and liquid circulation, separately with no contact and mixture. At the inner side of the BP, H_2 and air gases are supplied to the anode and cathode BPs, respectively. At the outer (back) side of the BP, the coolant (heating) fluid is provided to heat the stack instantly. The inner and outer sections of the BPs are presented in Figure 3.2. BPs were designed as 80x80 mm^2 whole dimensions with 10 mm thickness. All drawings were created using SolidWorks® commercial software.

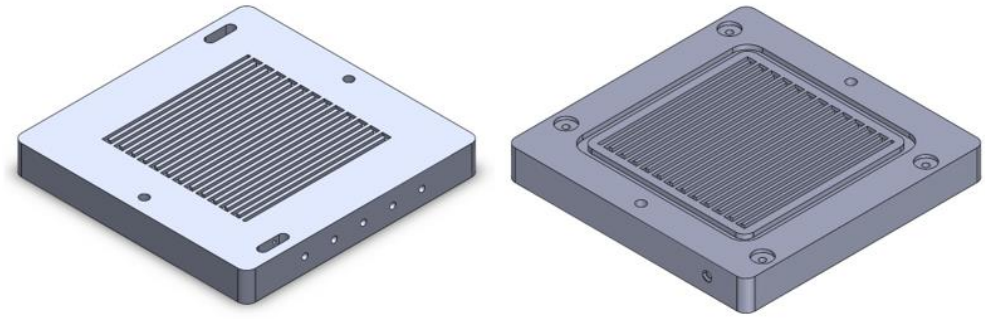

Figure 3.2. The inner and outer surfaces of the BP

All BP specifications are pointed out in Table 3.2. The whole stack equipment was fabricated by Hidronerji Hydrogen and Energy Systems (İvedik Organized Industrial Zone, Yenimahalle, Ankara). The author is thankful to Yavuz Topcu who is the director of the Hidronerji Company for his excellent experience and ability in fuel cell system construction.

Table 3.2. BP specifications

BP material	SS 316L
BP dimensions	80x80 mm^2
AA dimensions	50x50 mm^2
BP thickness	10 mm
Channel width	1 mm
Channel depth	1 mm
Rib height	1 mm
Radius dimensions at the corners	3 mm
Flow field geometry	Single-serpentine
O-ring channel dimensions	60x60 mm^2
Radius at the O-ring corners	5 mm
O-ring channel width	2.5 mm
O-ring channel depth	1.5 mm

The AA of the BP is designed according to the dimensions of the AA of the MEA (50x50 mm^2). Then, an 80x80 mm^2 area was assigned as a whole stack area considering the coating device area dependence. BPs are made of SS 316L material due to their high corrosion behaviour and high electrical conductivity (Öztürk et al., 2018). The AAs of the inner and outer sections were kept constant and placed back-to-back. Single-serpentine FF was chosen for both faces and channel width, depth, and height were 1 mm. Inner and outer images of the fabricated BPs are demonstrated in Figure 3.3.

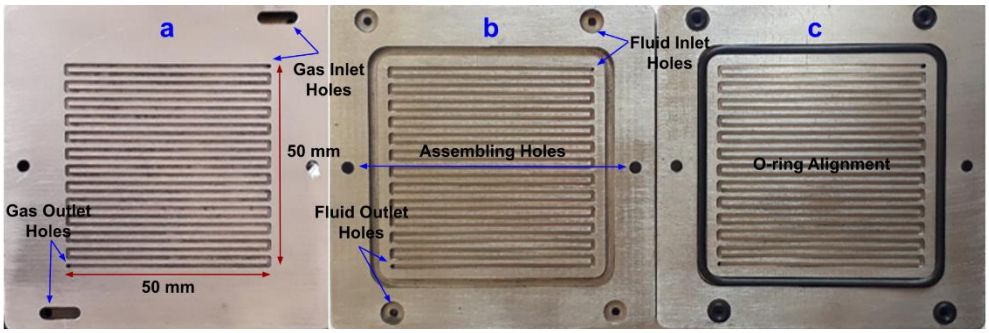

Figure 3.3. BP details; a) inner section details, b) outer surface details, c) O-ring alignment

3.2.2. O-Ring Alignment for the Back-Side of BP

Since a fluid is going to circulate at the back-side (outer) of the BP, an O-ring mechanism is designed to inhibit leakage from the sides. For this purpose, a 2.5 mm in width and 1.5 in-depth O-ring channel was machined throughout the 60x60 mm^2 area of the outer surface. O-ring spaces and alignment are picturized in Figure 3.3-b and c, respectively. Four O-rings which were 1.5 mm in diameter and 15.7 mm in perimeter were placed on the corners. An O-ring which was 2 mm in diameter and 213.5 mm in perimeter was placed on the outer line of the fluid flow area as seen in Figure 3.3-c. The diameters of the used O-rings for the corners and the outer line are represented in Figure 3.4 (dimensions are not scaled).

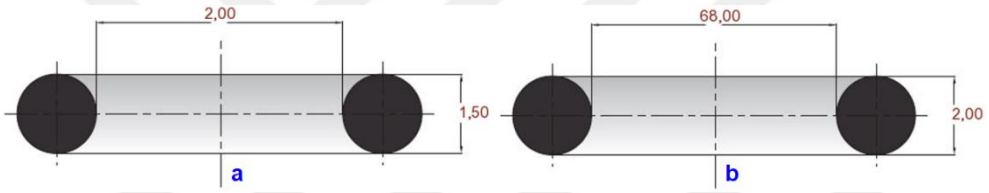

Figure 3.4. Dimensions of the used O-rings on the back-side; a) on the corners, b) on the outer line

O-rings, as known, have two diameters; the first one is its line diameter, and the second one is the whole perimeter. 1.5 mm in diameter and 15.7 mm in perimeter (calculated from πD^2) since holes were machined as 5 mm diameter on the corners. Similarly, 2 mm in diameter and 213.52 mm in perimeter (calculated from $\pi D^2, D = 68$) since the O-ring line was machined throughout the 60x60 mm^2 outer line of the fluid flow area.

3.2.3. BP Coating Process

Coating applications are very useful tools to decrease the contact resistance and corrosion level of the components as well as superior electrical properties (Rajaei et al., 2017). BPs and end plates used in the stack were made of SS 316L material. Their surfaces were coated using a thin coating to minimize current losses during the draw current. The coating process was completed by sputtering the gold

target to the surfaces of the BPs. The target was sputtered for 90 seconds by a coating machine in T. Nejat Veziroğlu Clean Energy Research Center (Niğde Ömer Halisdemir University, Niğde, Turkey) (coating machine model: Cressington Sputter Coater 108 auto, UK). The process is illustrated in Figure 3.5.

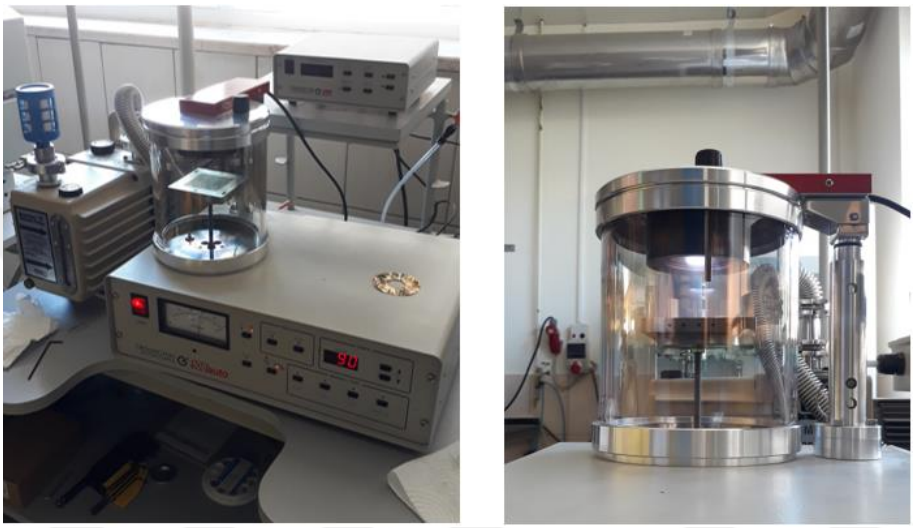

Figure 3.5. Gold coating process for the BPs

Two BPs were coated with gold with the mentioned method and therefore, the SS BPs were strengthened in terms of electrical conductivity and other related features. The BPs before and after coating application are presented in Figure 3.6.

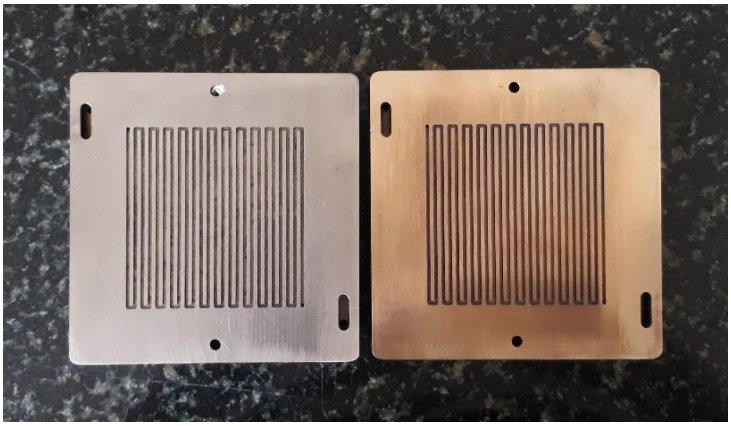

Figure 3.6. BPs without (left) and with the gold coating process (right)

3.2.4. Auxiliary Equipment

Current collectors, gaskets, mylar films, insulators, and fittings can be incorporated into the auxiliary equipment. Cable shoes were used for collecting current rather than current collector plates. Normally, current collectors fabricate as a separate component in the FC system as shown in Figure 1.3. However, separate manufacturing of this material brings about some problems such as the increase in contact resistance and total cost. Therefore, these disadvantages were eliminated by using cable shoes attached to the anode and cathode BPs.

In addition, silicone gaskets (as a sealant) were preferred in the short stack. One another important stack design parameter is determining and selecting the sealant thickness. Silicone sealants are good materials to provide low contact resistance and excellent sealing performance (Ghadimi et al., 2022). And sealant thickness should be determined considering the thickness of the MEA sandwich structure. Simply, whole MEA thickness and only membrane thickness should be calculated. Then, the difference between these two components should be divided by two because of the double-sided structure of the MEA. Thus, the required sealant thickness can be obtained. The calculation method is given in Equation 3.1.

$$t_{sealant} = \frac{t_{MEA} - t_{membrane}}{2} \tag{3.1}$$

Therefore, the silicone sealant thickness is determined as 410 μm considering the whole MEA thickness (870 μm) and polymer membrane thickness (50 μm).

Bolts used in the fitting of the stack coated with heat shrink tube and ensured insulation. Because bolts and screws operated in contact on both sides (anode and cathode). Thus, the first reason for the short circuit originated from the contact of the fittings. In other words, due to the not-well-insulated fitting tool set. Heat shrink

tubes (macaron) surrounded on M8 screws and heated by a lighter. Then, it shrunk and furled. Thusly, insulation was ensured with the mentioned technique.

3.2.5. End Plates

End plates are used for assembling the stack and are exposed to compression forces throughout the FC operation. Design drawings of the end plates are presented in Figure 3.7.

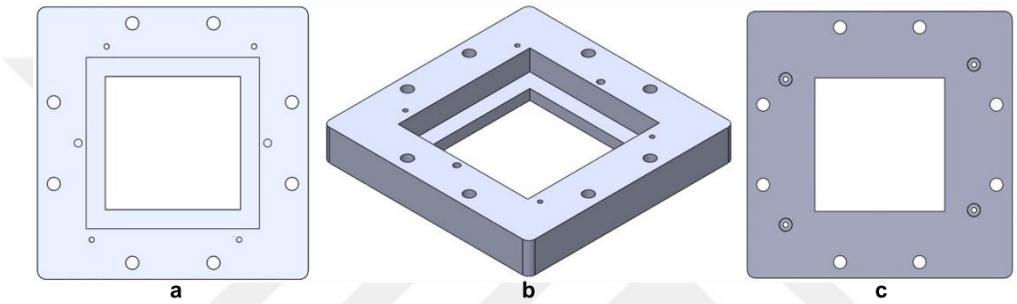

Figure 3.7. Solid drawings of the end plate; a) outer section, b) perspective, c) inner section

End plates made of SS 316L material with 100x100 mm^2 dimensions and 15 mm in thickness. Normally, end plates fabricate as a whole without any space in its center as pictured in Figure 3.7. In this thesis study, an observation from this wire is aimed at using a thermal camera. Thus, the flow of the working fluid (from the back-side of the BPs) is observed from this window. Thereby, the space is fulfilled with plexiglass (transparent) material. The plexiglass and end plate materials are a close fit and there is no leakage between these two components. In addition, the whole compression load acts on the O-rings, at first. The residual load, then, acts on the plexiglass and end plates. Plexiglass material has a similar thermal expansion behaviour to stainless steel. Thermal expansion coefficient (TEC) matching is another crucial design parameter to hinder micro or macro cracks that can be experienced in plexiglass material due to the freeze/thaw cycles. Besides the

mentioned TEC difference may lead to a leakage problem. The fabricated plexiglass/end plate couple is demonstrated in Figure 3.8.

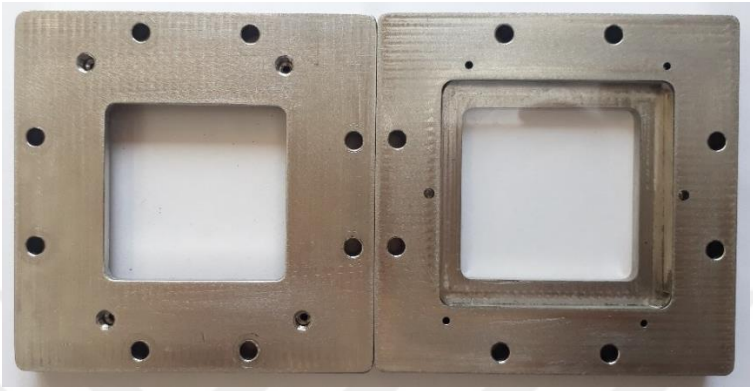

Figure 3.8. End plates with plexiglass; outer side (left), inner side (right)

All materials should be conductive between two end plates in an FC system. End plates should not conduct electricity; thus, insulator materials should be used at the inner sides of the end plates. Mylar films, at this point, are very appropriate ultrathin insulator materials made of versatile polyester. These materials do not affect by aging, and they have moisture-resistant behaviour. Therefore, self-adhesive mylar laminates were preferred as an insulator material and applied to the inner sides of the end plates. Silicone sealants and mylar films were cut using a laser cutting machine (Versa LASER, USA). The process is illustrated in Figure 3.9.

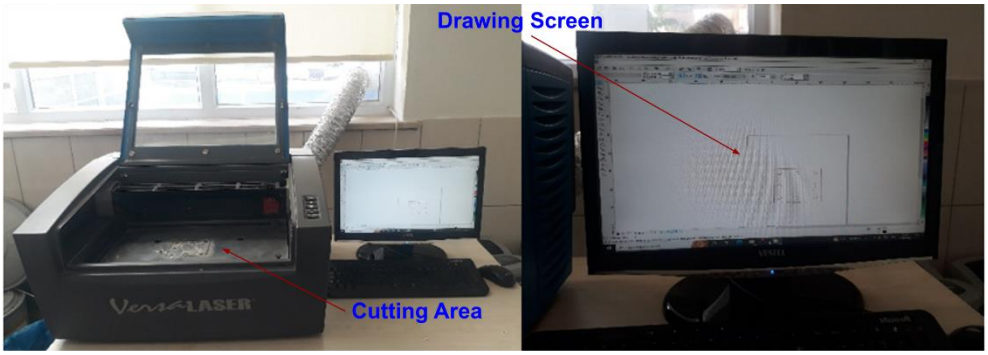

Figure 3.9. Laser cutting operation; cutting area (left), drawing screen (right)

Thus, mylar laminates and silicone gaskets were cut sensitively. After all material fabrication, the short stack was assembled in Figure 3.10.

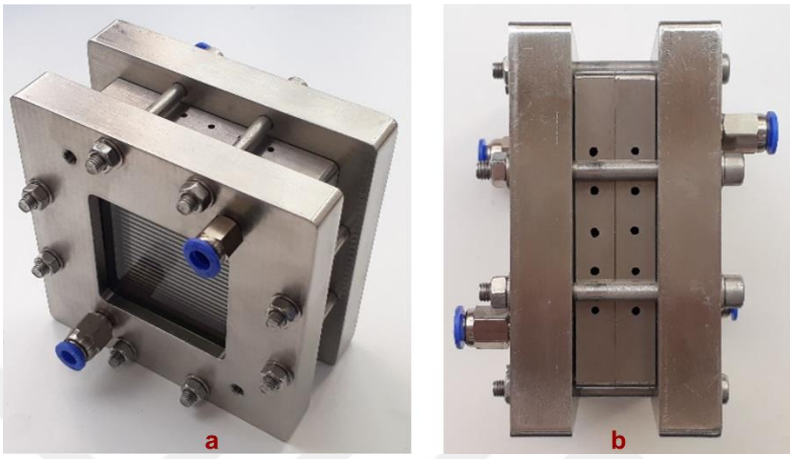

Figure 3.10. Short stack assembly; a) perspective, b) thermocouple holes

Therefore, the short-stack fabrication steps were completed, and all components were assembled successfully as depicted in Figure 3.10. Thermocouple holes were machined at this step, but the required information will be supplied on temperature (thermocouple measurements) following in the next sub-sections.

3.3. Assisted Heating Mechanism and Equipment

Assisted heating mechanism based on the coolant heating technique aforementioned and it is improved to ensure waste heat to the single-cell. The heating setup includes electronic driving equipment, a thermostat, a pump, a heater, an environmental chamber, and a heating fluid (coolant). All equipment is presented separately.

3.3.1. Electronic Control Circuit Accessories

An electronic circuit was constituted to control all external heating equipment including the heater, the pump, and the thermostat as picturized in Figure 3.11.

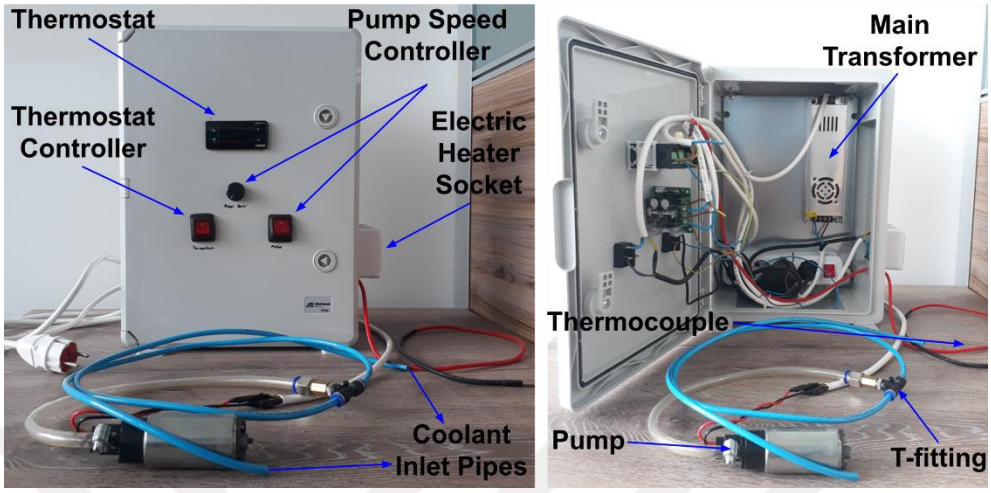

Figure 3.11. Electronic control circuit and equipment

A 10-kW main transformer was used to drive all electronic circuits. The thermostat was used to inhibit excessive heating of coolant, and also follow and control the coolant temperature by following a thermocouple. The pump and the heater specifications are given in the next sections. All equipment was placed into the panel (Mutlusan, İkitelli Organized Industrial Zone, Başakşehir, İstanbul). The author is thankful to Muhammet Yıldırımcan who is a technical staff working on electronic equipment establishment at Adana Alparslan Science and Technology University for his priceless support on the electronic setup.

3.3.2. The Pump

The coolant cycle was supplied thanks to the back channels machined onto the rear side of the BPs. The coolant was driven to the back of the bipolar plates thanks to a 12 V-DC pump (Bosch, NSA-I, 7200 rpm) which can operate at subfreezing temperatures. The image of the pump is provided in Figure 3.11 and it is used in the heater. The pump power was set as adjustable by a potentiometer as seen in the figure. Therefore, the pump speed was controlled by a dimmer, and the pump start or shutdown was controlled by a switch. A closed coolant cycle was

created and the coolant was sent to the stack while heated by the heater, at the same time.

3.3.3. Working Fluid

Working fluid should be operated at sub-zero temperatures and its boiling point should be suitable for the normal operating temperatures of the PEMFC. In this thesis study, in general, ethanol (C_2H_5OH, 99.99% purity) with an aqueous solution (80% ethanol – 20% pure water mixture) is preferred as a working (heating) fluid. Also, aqueous solutions (80% substance, 20% pure water) of the methanol (CH_3OH), ethylene glycol ($C_3H_6O_2$), and polypropylene glycol ($C_3H_8O_2$) fluids were prepared and tried as a working fluid for cold start experiments. Physical specifications of the pure working fluids are presented in Table 3.3. All fluids have 99.99% purity and they were purchased from Sigma-Aldrich Chemie GmbH (Taufkirchen, Germany).

Table 3.3. Physical properties of the working fluids (pure)

Substance	Chemical Composition	Melting Point (ºC)	Boiling Point (ºC)
Ethanol	C_2H_5OH	-114	78
Methanol	CH_3OH	-97.8	64.7
Ethylene Glycol	$C_2H_6O_2$	-13	197
Propylene Glycol	$C_3H_8O_2$	-25	200

The melting points of the ethanol and methanol are quite enough to level for the cold start operation except for ethylene glycol (-13 ℃) and polypropylene glycol (-25 ℃), as seen in Table 3.3. On the other hand, the boiling points of the ethanol and methanol coolants are not satisfied the requirements for the operating of PEM fuel cells at normal conditions (65-75 ℃). All physical specification data is supplied by the manufacturer companies for which ethanol (Website, 2023d), methanol (Website, 2023e), ethylene glycol (Website, 2023f), and propylene glycol (Website, 2023g). These substances can solve in the water, homogeneously, and the water content affects the melting and boiling of the substances. The whole substances were

mixed with pure water at 20% (80% coolant – 20% pure water) proportions. 80% rate was selected in order to compare the specifications of the coolants without losing their features. Otherwise, a 50% solution would have been preferred. Each mixture ratio will result in a different profile, naturally. 0.5 lt of each mixture was added to the heater and used in the tests. Test parameters and conditions are presented in the next section.

3.3.4. The Heater

An electric heater with 1.8 kW power is used to heat the working fluid (mostly ethanol). The heater selection is one of the most important challenges of the thesis study. The chosen heater should be operated in a conditioning cabinet and at sub-zero temperatures. Another important parameter is that the heater should be operated with different fluids. Because ethanol, methanol, ethylene glycol, and polypropylene glycol fluids and their aqueous solutions should be heated by the assigned heater. Therefore, an electric heater (heat flux adjustable) was preferred to warm-up the working fluid as depicted in Figure 3.12.

3.3.5. Environmental Chamber

A temperature and humidity-controlled conditioning chamber (ESPEC Corp, SH-221, Japan) was used to reach sub-zero temperatures. The cabinet can be conditioned in the range of -30 to 165 ℃. Due to the operating temperature range of the chamber, the cold start experiments are restricted until -30 ℃. A chamber and stack connections are provided in Figure 3.12.

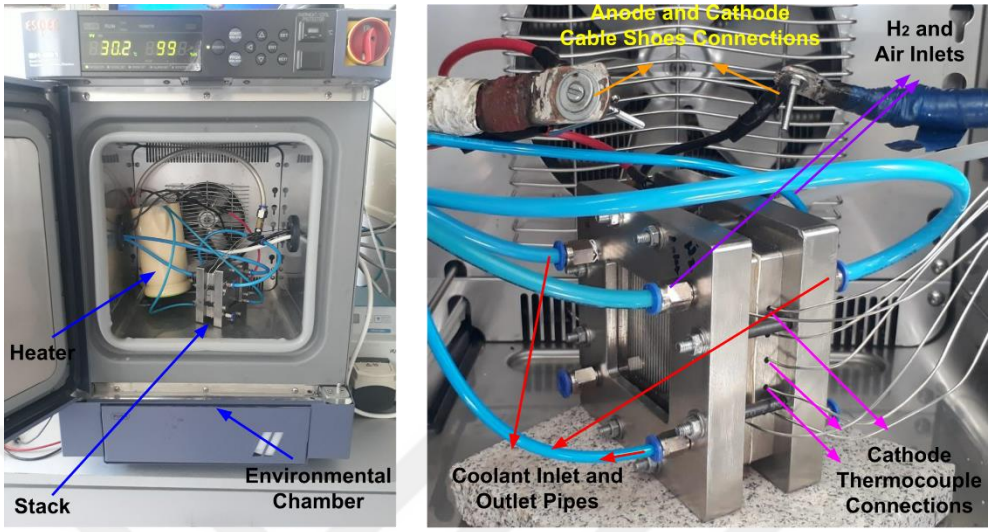

Figure 3.12. Connection details in the environmental chamber

The positions of the heater, the pump (placed into the heater), and the stack are illustrated in Figure 3.12 (left). Connection details of the stack are also provided in Figure 3.12 (right). H_2 and air gases are supplied to the inlet of the BPs, and coolant fluid (working fluid) is supplied to the rear side of the BPs as shown in Figure 3.12. Cable shoes connections of the anode and the cathode sections are used for current drawn from the cell. The pneumatic pipes (6 mm in diameter) were preferred for the driving of the coolant. A closed-loop coolant cycle was created and the circulated fluid was turned to the heater after each cycle.

3.4. Test Equipment

3.4.1. ARBIN Fuel Cell Test Station

All experimental setup was established, and all cold start tests were conducted in T. Nejat Veziroğlu Clean Energy Research Center Fuel Cell Laboratory (Niğde Ömer Halisdemir University, Niğde, Turkey). Test equipment includes all equipment operating synchronically which are the electronic load, the stack, and its accessories, as illustrated in Figure 3.13.

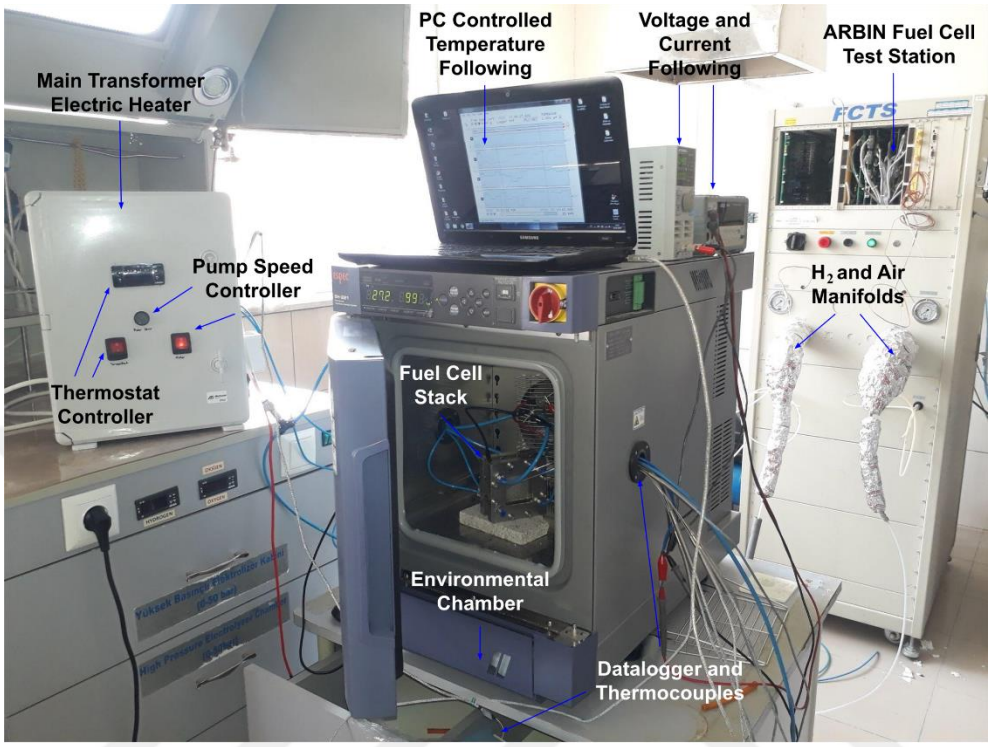

Figure 3.13. Experimental installation with ARBIN FC test station

The Standard ARBIN Instruments Fuel Cell Test Station (Texas, USA) was used in the first leg (performed at -10 °C) of the conducted cold start tests. The supply of the reactant and oxidant gases to the stack and voltage-current values were followed and the current was drawn by the FC test station.

3.4.2. Electrochem Fuel Cell Test Station

Electrochem Fuel Cell Test Station (ElectroChem®, Inc., Massachusetts, USA) is used with Erdes Fuel Cell Test Station Controller (Erdes Technology Chemistry Industrial Design Control Company, Çankaya, Ankara) at the second leg of the studies (below -10 °C). The experimental installation with the Electrochem FC test station is demonstrated in Figure 3.14.

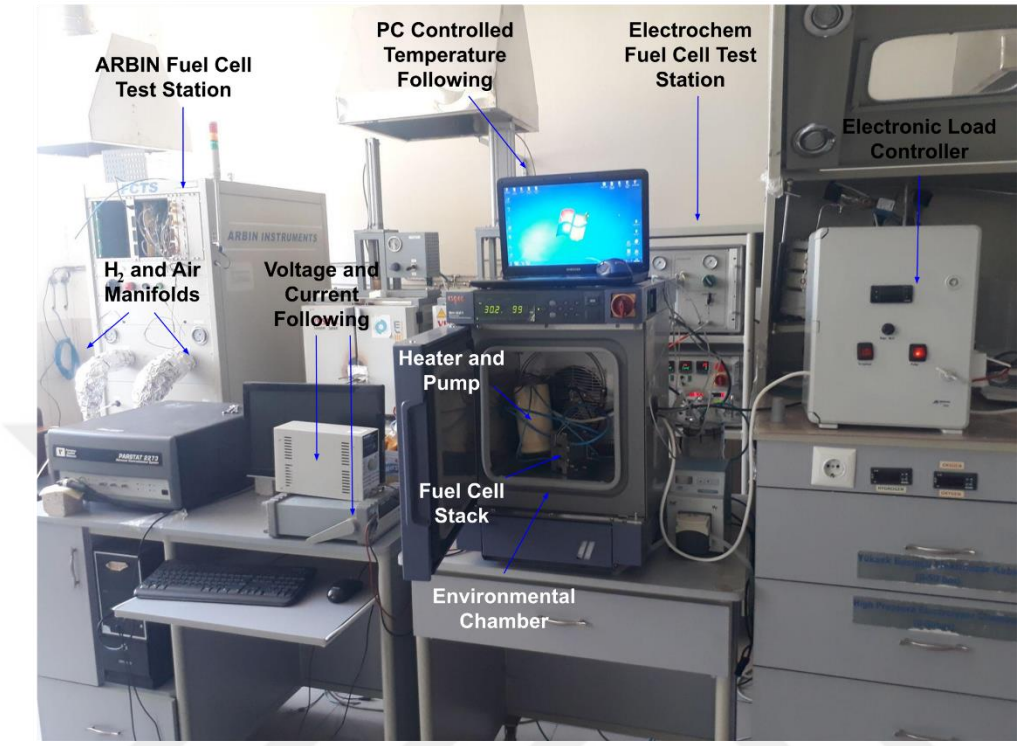

Figure 3.14. Experimental installation with Electrochem FC test station

In addition, schematic representation of the experimental setup is illustrated in Figure 3.15. The load was applied and the current was drawn from the Electrochem FC test station while the gases were supplied from the ARBIN test station. The main screen of the Electrochem management system is provided in Figure 3.16 which includes N_2, H_2, and air gas flow rate management and open/shutdown valves. This screenshot was taken during a test as seen that the gas flow rates are 0.4 and 1.2 lt/min for the H_2 and air gases, respectively.

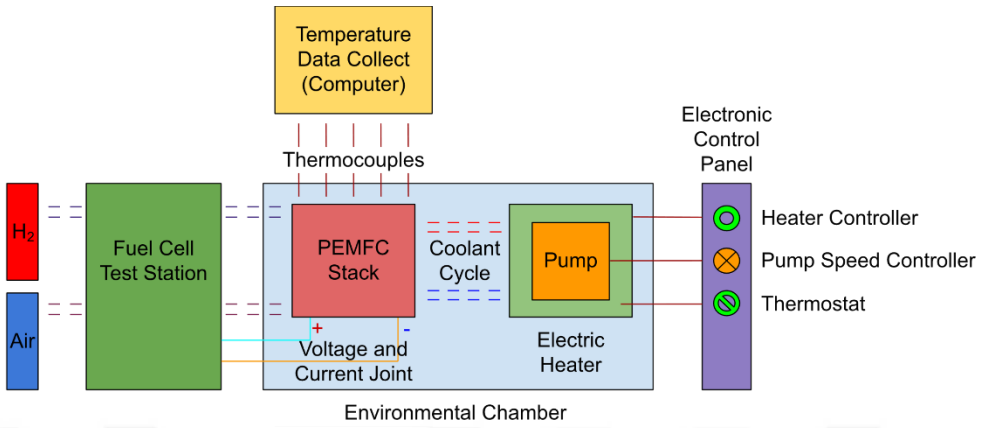

Figure 3.15. Schematic representation of the experimental bench

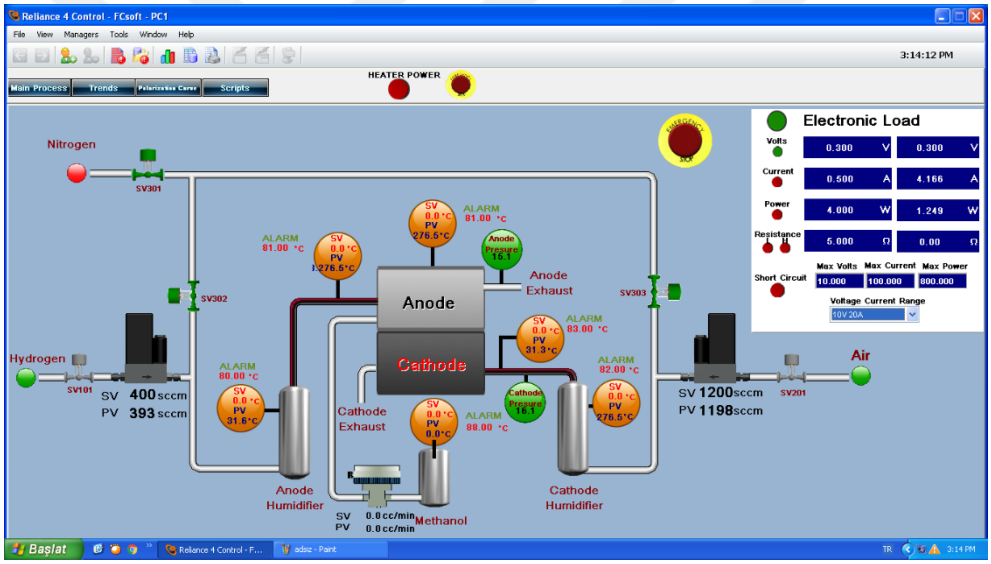

Figure 3.16. The main screen of the Electrochem test equipment

3.5. Data Collecting

Current and voltage data were recorded thanks to the Electrochem and ARBIN FC test stations. However, one of the most important features of the study is the temperature pursuit process by the cathode BPs. For this reason, the thermocouple holes were machined to the mid-section of the BPs, symmetrically.

Outer and inner surface details and the machined thermocouple holes are presented in Figure 3.17-a and Figure 3.17-b.

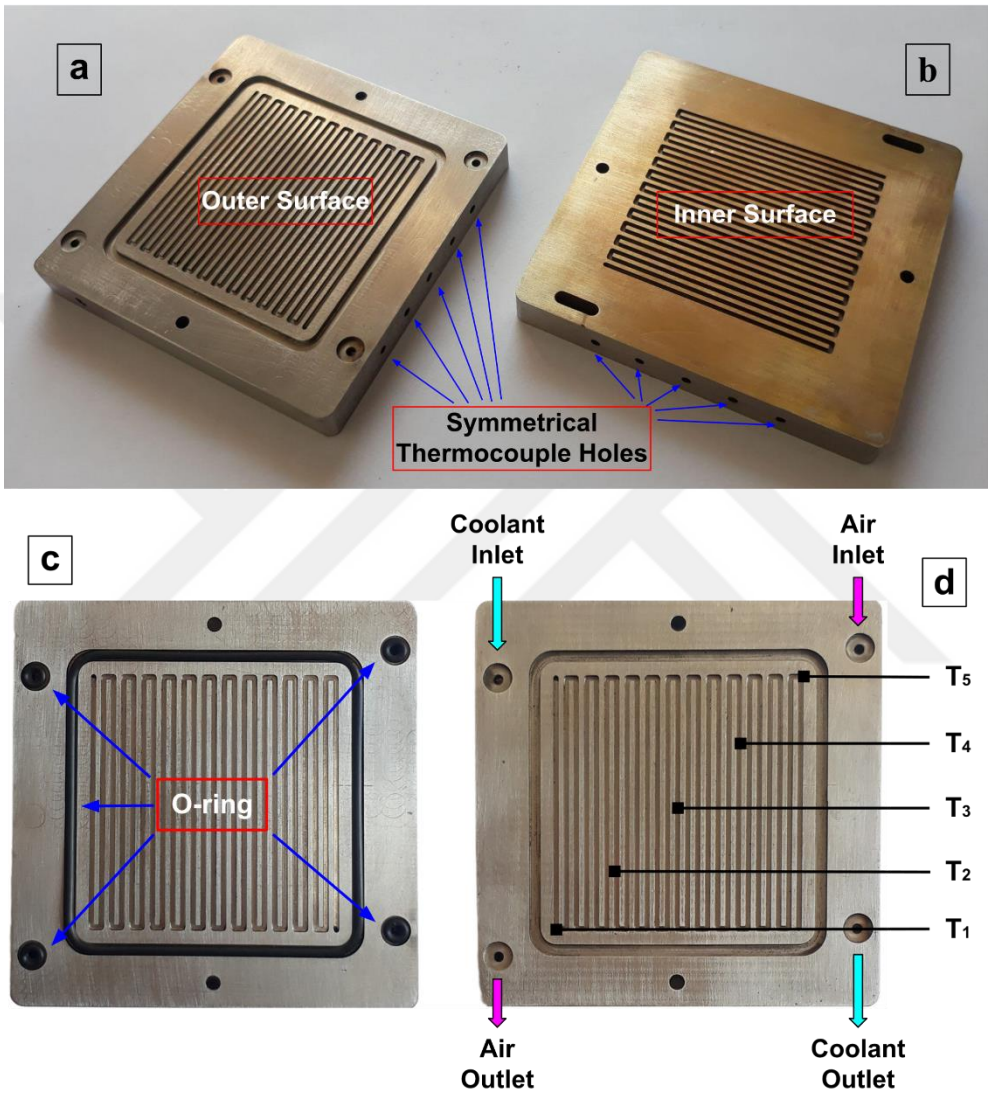

Figure 3.17. Symmetrical temperature monitoring mechanism

In addition, the O-ring settlement, and gas and coolant inlet and outlet points are indicated in the same Figure c and d sections. The cell temperature was followed by symmetrical five thermocouples (K-type, purchased from Ordel Ortadoğu

Electronics, Ostim Organized Industry Zone, Yenimahalle, Ankara) placed into the cathode BP. Because the electrochemical reactions occur at the cathode section and more to the point water particles form in this department. Therefore, the solution key to the cold start issue depends on the correct analysis of the cathode section. In addition, the details on the thermocouple alignment can be found in the experimental setup projections provided in Figure 3. 12 and Figure 3.13.

Temperature data was collected using a USB-connected PC-followed data logger (Measurement Computing, TracerDAQ Pro). The used data logger and thermocouples are demonstrated in Figure 3.18.

Figure 3.18. Measurement devices; data logger (left), K-type thermocouples (right)

Besides, two thermocouples were placed at the anode inlet and outlet points, and the coolant temperature was also followed by a thermocouple. Thus, a temperature record was performed from eight different points for all cold start tests. Temperature profiles were supplied to compare and characterize the cold start performance of the suggested starter methods.

3.6. Temperature Visualization

The obtained temperature profiles are enough to understand the cold start mechanism of the operating conditions. Notwithstanding, a visualization study was performed using experimental temperature data to increase comparison opportunities for the cold start techniques. A series of codes were written using MATLAB & Simulink commercial software to convert the temperature data to an image.

Lagrange Interpolating Polynomials method was followed (Burden and Faires, 2010) to obtain a temperature map throughout the cell AA. Five thermocouple data comes from the experiments were used as actual values and the other sections were determined by the mentioned numerical approach. The cell active area dimensions are 50x50 mm^2, and the area is divided by 50x50 grids, horizontally and vertically. Also, h = 0.1 step size was assigned for each grid, and Lagrange interpolating polynomials were derived at i = 1, 2, 3, 4, 5. The first-degree polynomial interpolating approximation equations were used using the distinct points (x_0, y_0) and (x_1, y_1). The interpolation and the Lagrange interpolating polynomial functions are presented in Equations 3.2 and 3.3, respectively.

$$L_0(x) = \frac{x - x_1}{x_0 - x_1} and \;\; L_1(x) = \frac{x - x_0}{x_1 - x_0} \tag{3.2}$$

$$P(x) = L_0(x)f(x_0) + L_1(x)f(x_1) = \frac{x - x_1}{x_0 - x_1}f(x_0) + \frac{x - x_0}{x_1 - x_0}f(x_1) \tag{3.3}$$

The actual experimental data and estimated novel values were used when creating the polynomials. The interpolation approach is expanded through the unknown regions considering the construction of the polynomial of degree at most n that passes through the n+1 points:

$$(x_0, f(x_0)), (x_1, f(x_1)), \dots, (x_n, f(x_n)).$$

The numerator of $L_{n,k}(x)$ contain the term;

$$(x - x_0)(x - x_1)\dots(x - x_{k-1})(x - x_{k+1}) \dots (x - x_n)$$

The denominator of $L_{n,k}(x)$ should be the same to obtain $L_{n,k}(x) = 1$. Thus, x=xk should be evaluated and the $L_{n,k}(x)$ can be calculated using Equation 3.4.

$$L_{n,k}(x) = \frac{(x - x_0) \dots (x - x_{k-1})(x - x_{k+1}) \dots (x - x_n)}{(x_k - x_0) \dots (x_k - x_{k-1})(x_k - x_{k+1}) \dots (x_k - x_n)} \tag{3.4}$$

Thereby, a mathematical relation and connection between the grids were ensured in horizontal and vertical directions. The mathematical application of the section was implemented in MATLAB and a series of codes were written. The MATLAB code is presented in Appendix – A1 section. A picturization study related to the process is provided in Figure 3.19. Used experimental (original) data and the determined (visualized) sections are denoted with red (+) and gray (x) characters, respectively. The obtained visualized images were used to compare the warm-up profiles of the cold start methods. The images were taken every 100 seconds toward the end of the related cold start test.

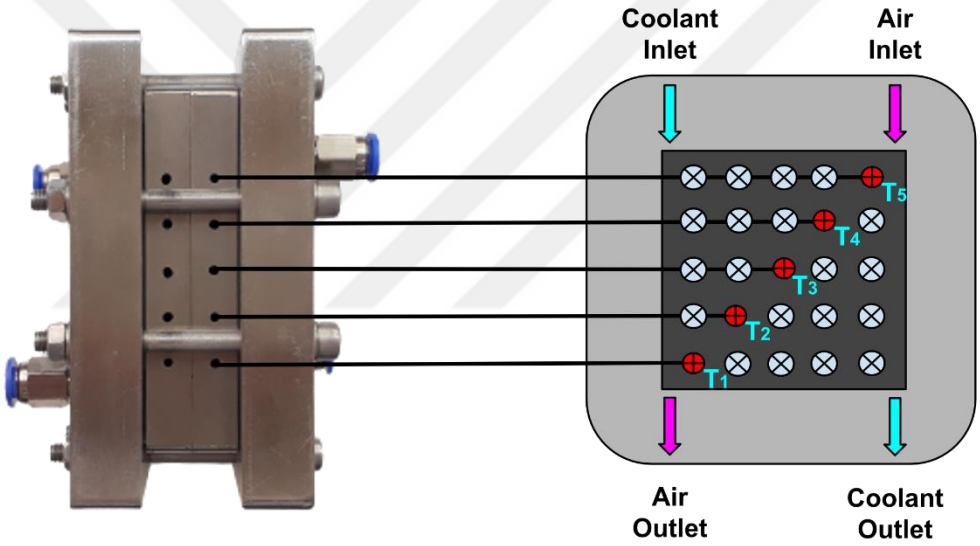

Figure 3.19. Original (experimental) data and mathematically estimated data points

4. EXPERIMENTAL STUDIES

All materials and methods used in the thesis were explained in detail in the previous section. Herein, the conducted experimental study details and cold start processes were discussed in sub-sections.

4.1. MEA Activation Process

The MEA should be activated before it is used in the tests. Indeed, the MEA can be used directly without any activation. But, the maximum current level can not be reached at the level of activated MEA anytime. Thereby, the MEA activation process was completed before beginning the cold start tests by following the activation process provided in references by Yang et al. (2021) and Zhong et al. (2021). The activation procedure can be done by different applications, too. In this thesis, the MEA activation was ensured by the constant voltage technique. This approach is suitable to avoid the long-term deterioration of the constant current MEA activation as reported by Taghiabadi et al. (2019). The operating conditions and followed technique on the MEA activation are illustrated in Table 4.1.

Table 4.1. MEA activation process (Yang et al., 2021, Zhong et al., 2021)

Parameter	**Value**
Environment chamber temperature	75 ºC
Anode/cathode inlet gas temperature	75 ºC
Gas humidity	100%
Operating voltage	0.7, 0.5, and 0.3 V
Anode H_2 gas flow rate	0.5 l/min
Cathode air gas flow rate	1.5 l/min
Back pressure	-

The environmental chamber was set to 75 ℃ and the temperature stabilization was ensured for 1h. Then, H_2 and air gases are supplied to the anode and cathode compartments with 0.5 and 1.5 l/min flow rates, respectively with 100% relative humidity (RH). The cell was operated respectively at 0.7 and 0.5 V constant

voltage for 1h. Then, the cell operated at 0.3 V constant voltages for 2h, and the MEA activation process was completed. The polarization curves were obtained before and after the activation process. The temperature was 75 °C and the H_2 and air flow rates were 0.5 and 1.5 lt/min, respectively. All cold start tests were conducted with the activated MEA.

4.2. Viscosity Measurements

Viscosity and density values are related to the heat capacity of the fluid and it is required to calculate heat capacities and to determine the warm-up profile of the working fluid. The viscosity measurements were performed using Julabo ME-16G – Glass Capillary Viscometer device (Julabo GmbH, Seelbach, Germany) as presented in Figure 4.1-a.

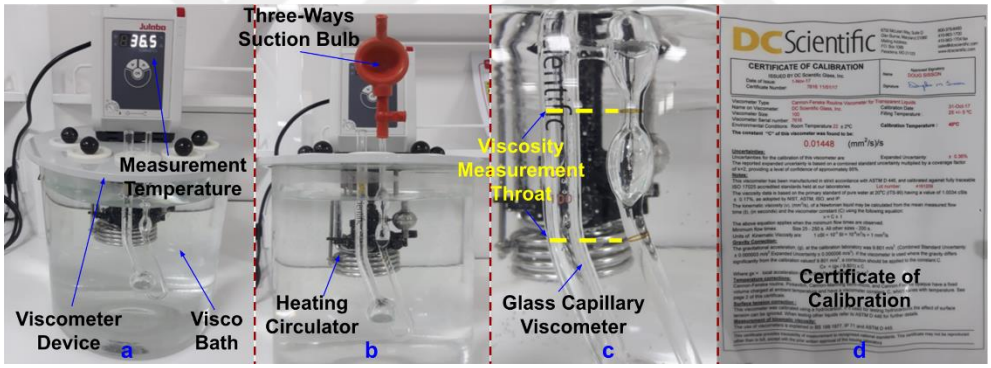

Figure 4.1. Viscosity measurement setup; a) viscometer device and equipment, b) three-ways suction bulb and heating mechanism, c) viscometer type and measurement points, d) certificate of calibration

Viscometer operates based on the glass capillary method and viscometer device equipment consists of a visco bath, a heating circulator, and a calibrated capillary measurement glass. Firstly, water is filled to the visco bath and the temperature is set to the measurement point using the device panel (Figure 4.1-a-b). The measured fluid is filled into the capillary glass and moves to the level above the measurement throat (Figure 4.1-c) with the help of a three-way suction bulb (Figure 4.1-b). Then, the bulb is ejected and the tip of the glass opens to the atmosphere. The

fluid level decreases by the capillary effect and atmospheric pressure and passes throughout the measurement throat. The time passed is saved manually during this process and the measurements repeat five times to increase the level of accuracy.

In this thesis, the viscosity measurements were performed at 40 °C. Because the capillary glass (DC Scientific, Inc., Maryland, USA) is certified at 40 and 100 °C. The certificate of calibration for 40 °C is provided in Figure 4.1-d. The device temperature was set to 40 °C and the aqueous solutions of the working fluids were inserted into the capillary glass. The process was applied mentioned above and the measurements were conducted five times per sample. The average time when the fluid is passed through the throat is multiplied by the "C" constant (available on the certificate of calibration and given as 0.01448 (mm^2/s)/s. Therefore, the kinematic viscosity (v) values of the fluids were obtained.

The author wishes to thank the helps on viscosity and density measurements to the all academic staff of the Mechanical Engineering Department of Adana Alparslan Türkeş Science and Technology University, especially Res. Asst. Mahir Şahin.

4.3. Density Measurements

Density measurements were carried out using a portable digital density meter (Kyoto Electronics DA-130N, Kyoto Electronics Manufacturing (KEM) Co., Ltd., Kyoto, Japan). The measurement method is very simple since the device is automatic. The pipette of the device is submerged in the measured fluid cap and pushes the button on the device. The result appears on the screen. The density measurements of the aqueous solutions of the working fluids were performed at room temperature. The measurements were conducted during the viscosity measurements. Each measurement was repeated five times and the average point of the values are evaluated as the density of the fluid. The measurement method and the device used are given in Figure 4.2.

Figure 4.2. Density measurements

4.4. Self-Stack Operation without Assist

The unassisted operation of the MEA is an important feature that provides insight to the cold start ability of the MEA. The single-cell stack was operated without any assistance at -10 ℃. 0.5 lt/min H_2 and 1.5 lt/min air gases were sent to the stack after the temperature stabilization was ensured in the conditioning cabinet. The cell temperature was followed by five points on the cathode BP and the cell was operated at constant voltage mode at 0.4 V. Temperature distribution throughout the cell AA was determined and the capacity of the MEA was specified with the absence of an external heat source. Another self-operation test was also conducted under the same operating conditions as the test previous. The reactant and oxidant gases were sent to the cell, and only open circuit voltage (OCV) was recorded without a current draw from the cell. Therefore, the cell potential and unassisted operation abilities of the single-cell stack were put forward.

4.5. Equal Heating Check of Anode and Cathode Sides

The heating mechanism was tested before parametric case studies. The stack was not operated when control tests were carried out to understand if both sides were

heated equally. It is known that if the cell was operated, the cathode compartment would be warmer than the anode side. Herein, 1 l ethanol coolant was heated to 40 ºC before being sent to stack. The pump operated at full power (12VDC) and hot ethanol was supplied to the anode and cathode compartments, at the same time. The temperature was followed by inlet (T_1) and outlet (T_5) points of the compartments.

4.6. Cold Start Test Parameters

The cold start tests were performed under sub-sections to understand the effects of each piece of equipment in the heating mechanism, separately. The whole initial parameters were examined at -10 ℃. They are investigated dividing by sub-sections:

- Optimum coolant selection
- Effect of pump operating voltage
- Optimum heating section
- Effect of heater operation duration
- Parametric case studies below -10 ℃

4.7. Optimum Coolant Selection

Working fluid freezing and boiling points should be appropriate for operations at sub-zero temperatures and normal operating temperatures. Aqueous solutions (80% substance, 20% pure water) of the ethanol (CH_5OH), methanol (CH_3OH), ethylene glycol ($C_3H_6O_2$), and polypropylene glycol ($C_3H_8O_2$) fluids were prepared and tried as a working fluid for cold start experiments. 0.5 lt of each mixture was added to the heater and used in the tests. The single-cell stack and the heating mechanism were operated synchronized. The heater and the pump were operated for 20 and 150 s, respectively. At the same time, 0.5 lt/min H_2 and 1.5 lt/min air gases were sent to the stack and the current was drawn at 0.4 V.

4.8. Effect of Pump Operating Voltage

12 VDC pump was used to drive the closed coolant cycle as aforementioned. In addition, the pump operating voltage was controlled with the help of a potentiometer, and the pump was operated at 3, 6, 9, and 12 VDC voltages. Correlatively, the drawn current and the coolant flow rate were changed depending on the pump power. It should be noted that the ethanol flow rates decrease a few amounts due to the pressure losses in the flow channels when it is connected to external coolant inlet points. The measured flow rates and drawn current corresponding to each voltage value are presented in Table 4.2. The measurements were performed with and without the connections and the connections were supplied to both sides of the stack. Therefore, the sum of both flow rates was illustrated. 0.35 A current was drawn by the pump and supplied 0.0025 kg/s ethanol flow at 3V operating voltage after the connection. 0.00583333, 0.866667, and 0.01083333 kg/s flow rate was delivered to the stack at 6, 9, and 12 VDC operating voltages, respectively. The flow rates can be seen as low level due to the presenting unit (kg/s). It should be considered that the 12 VDC pump operation delivered 0.01083333 kg/s (0.65 kg/min) and 0.03833333 kg/s (2.3 kg/min) flow rates with and without coolant inlet connection, respectively. The flow rates of the idle operating of the pump are higher than the connected flow rates, as expected, as shown in the table. It is proved that the pressure loss in the back flow channels is very high and decreased the flow rate considerably.

Table 4.2. Measured coolant (ethanol) flow rates concerning the pump operating voltage

Operating voltage (V)	Drawn current (A)	Power (W)	Before Connection	After Connection
			Flow rate (kg/s)	Flow rate (kg/s)
3	0.35	1.05	0.00884615	0.0025
6	1.75	10.5	0.02064103	0.00583333
9	4.44	40	0.03066667	0.00866667
12	6.66	80	0.03833333	0.01083333

Therefore, the effect of coolant flow rate was investigated as an initial parameter. The temperatures at the inlet (T_1) and outlet (T_5) points of the cathode BP were collected for all tests.

4.9. Optimum Stack Heating Method

The study aims to heat the single-cell stack thanks to the installed external coolant cycle. However, the coolant can be supplied to the stack in various ways which are self-anode, self-cathode, and double-side heating strategies. Thereby, the optimum stack warm-up way was examined in addition to the pump operating voltage conditions.

4.9.1. Self-Anode Heating Strategy

The stack and the external coolant cycle were operated concurrently. The stack was operated using H_2 and air gases with 0.5 and 1.5 l/min flow rates, respectively. At the same time, the current was drawn from the cell at 0.3 constant voltage. Therefore, the current was followed when the cell was operated at the potentiostatic method. Standard Arbin Fuel Cell Test Station equipment was used to supplying of gases, current collecting, and data processing. A dry membrane was used for all cold start tests. For this reason, the stack was disassembled after each cold start operation and reassembled after removing the occurred water particles on the surfaces of the components. On the other hand, the coolant cycle was operated with 0.5 l ethanol. The coolant was heated for 20 seconds, and the pump was operated for 150 seconds. Consequently, the cell and coolant cycle was operated synchronously at -10 ºC cold start temperature. The coolant was provided to the anode compartment, only. In this operation, the cathode side was not heated by the coolant. Nevertheless, the cathode section was warmup by the dual effect of coolant circulation at the anode side and chemical reactions at the cathode side. The warmup profile of the stack was followed by the thermocouples for 600 seconds. All connection details and cold start parameters were provided in Figure 3.13 and Table

4.3, respectively. In addition, the pump was operated at 9 and 12 VDC pump operating voltages, and two tests were performed with the self-anode method. The pump is consumed 40 W and 80 W power for the 9VDC and 12VDC operations, respectively. Because the pump is operated at full power (80 W) for both side heating. Therefore, 80 W power is shared equally by the anode (40 W) and cathode (40 W) sections. Thus, the combined effect of the pump power and heating strategy was studied as an extra parameter.

Table 4.3. Cold start test parameters for the initial comparison conditions

Parameters	**Value**	**Unit**
Test temperature	-10	°C
H_2 flow rate	0.5	lt/min
Air flow rate	1.5	lt/min
Relative humidity of H_2	0	%
Relative humidity of air	0	%
Cell operating voltage	0.3	V
Coolant type	Ethanol	-
Coolant volume	0.5	lt
Coolant heating duration	20	s
Pump operation voltage	9 and 12	V (DC)
Pump operation duration	150	s

4.9.2. Self-Cathode Heating Strategy

The coolant was provided to the cathode side as different from the self-anode heating strategy. Similarly, the other operating parameters were kept constant as presented in Table 4.3. The coolant was supplied to the only cathode side with 9VDC and 12VDC pump operations for the durations aforementioned. At the same time, the stack was operated, and the current was drawn from the cell. The temperature distribution was recorded throughout the tests.

4.9.3. Double-Side Heating Strategy

The coolant was provided to both sides in this strategy as different from the previous cases. The other operating conditions were constant. Besides, the pump was

operated at only 12VDC to drive the coolant cycle. The stack was operated co-ordinately, and the current was drawn at 0.3 V in potentiostatic mode. Therefore, the stack gained heat from both sources which are anode and cathode coolant circulations and exothermic H_2/O_2 reactions. The cold start test was maintained for 600 seconds, and the temperature was recorded along with the test. Thereby, it is determined that the optimum heating strategy is achieved by the tests performed in this section.

4.10. Effect of Heater Operation Duration

The optimization of the heater's operating duration is vital to decrease the overall energy consumption level. Four different cases were conducted to put the importance of heater operation in cold start tests:

1. 10 s heater, 150 s pump operation,
2. 15 s heater, 150 s pump operation,
3. 20 s heater, 150 s pump operation,
4. 15 s heater, 262.5 s pump operation

The heater operation duration was raised by 5 seconds for the first three tests. The fourth test was carried out for a comparison of the effectiveness of the pump and the heater with Case #3. The temperature profiles, voltage, and current levels of the cases were evaluated and compared.

Only an MEA was used for the tests and the MEA should be stable for each cold start test to provide sound judgment on the comparison of the tests. The most suitable and acceptable operation is the use of a dry membrane in the tests. To provide this, the stack was disassembled after the tests, and the MEA was dried by natural convection. Water droplets were removed from the flow channels of the cathode BP and with the MEA drying process, completely. Then, the components

were assembled again and the next test was conducted. Herein, it should be noted that the compression load of the assembly affects the overall cell performance.

Table 4.4. Cold start test parameters for the parametric case studies

Parameters	**Value**	**Unit**
Test temperature	-10, -15, -20, -25, -30	°C
H_2 flow rate	0.4	lt/min
Air flow rate	1.2	lt/min
Relative humidity of H_2	0	%
Relative humidity of air	0	%
Cell operating voltage	0.3	V
Coolant type	Ethanol	-
Coolant volume	0.5	lt
Coolant heating duration	15 or 20	s
Pump operation voltage	12	V (DC)
Pump operation duration	150 or 262.5	s

Therefore, the compression force should be kept stable since the stack is assembled/disassembled due to the freeze/thaw cycles. The stack was compressed using a torque wrench with 4 Nm torque before each test. Thusly, pressure stabilization and homogenous distribution were achieved through both internal chemical reactions and external coolant circulation. Actually, the MEA performance is influenced by the compression torque which is a significant performance parameter. The MEA power increases with the increase of compression load, in general. However, it ends when reached a peak point and decreases, then (Li et al, 2019a). Overload damages to MEA, and therefore the stack should be tightened appropriately. The value of torque (4 Nm) was randomly specified in this thesis due to the clamping force is not considered a separated cold start parameter. The single-cell operated and 0.4 and 1.2 lt/min gas flow rates of H_2 and air were sent to the anode and cathode compartments, respectively. The current was drawn at 0.3 constant voltage mode during the tests. At the same time, the coolant loop was activated and the heater and the pump were operated for the aforementioned durations. The cell gained heat from the combined effect of the coolant loop and the

cell operation. Fundamental cold start test parameters are given in Table 4.4. Temperature follow was supplied by the cathode thermocouples during the tests and compared. Voltage and drawn current values were recorded.

4.11. Parametric Case Studies

The coolant heating method leads to over-energy consumption in case of successful energy management is not provided (Zhan et al., 2018; Yang et al., 2021; Luo et al., 2022). The main reason for overconsumption is the heater (1800 W at full power) in the established heating mechanism. The other energy-required equipment is the pump (80 W at full power).

Thus, the energy consumption levels of the equipment were determined, and the effectiveness of the pump and the heater were compared at the same energy level. The weaknesses and the strengths of the equipment were found out. To reveal this, the cold start tests were performed in the range of -10 and -30 °C. Characteristics of the energy-consuming equipment were revealed by the temperature and current profiles. The proposed heating mechanism was tested at -30 °C lowest cold start temperature. The importance of the heating strategy was revealed by the current thesis study.

The cold start tests were conducted at -15, -20, -25, and -30 °C. Two main parameters were compared: Heater operation duration vs. pump operation. 1800 W power electric heater and 80 W power pump were used in the tests to heat and deliver the ethanol to the stack, respectively. The effectiveness of these two energy consumer components was investigated under the same operating conditions. Because only 1-second operation of the heater is equivalent to 22.5 seconds of operation of the pump. Therefore, the optimum management system was investigated under the same energy consumption levels.

4.11.1. Case Studies at -15 ℃

Two tests were carried out at -15 °C:

1. 20 s heater, 150 s pump operation
2. 15 s heater, 262.5 s pump operation

The tests were conducted under the same operating conditions as in the previous section. Therefore, the temperature profile characteristics of the cases were compared.

4.11.2. Case Studies at -20 ℃

1. 20 s heater, 150 s pump operation
2. 15 s heater, 262.5 s pump operation

Cases were conducted under the same operating conditions as the previous section. The temperature profiles of the cases were compared.

4.11.3. Case Studies at -25 ℃

The operation ability of the cell decreases with the decrease of the cold start temperature. The tests were conducted under the same operating conditions as the previous case studies, and the performances of;

1. 20 s heater and 150 s pump operation
2. 15 s heater and 262.5 s pump operation case studies were compared.

4.11.4. Case Studies at -30 ℃

The cold start tests were performed at -30 °C as the lowest temperature. In this section, the operation duration of the pump and the heater were increased due to the insufficient heat supply from the established external loop (for 15 or 20 s heater operation). As an initial try, 30 s heater operation and 210 s pump operation were assigned. After the initial test;

1. 50 s heater, 200 s pump operation
2. 45 s heater, 312.5 s pump operation tests were conducted.

Herein, operation durations increased proportionally, and the overall energy consumption levels were kept equal. Therefore, the temperature profile characteristics of the cases were compared at -30 °C.

4.12. EIS Measurements

Electrochemical impedance spectroscopy (EIS) is a good diagnostic test approach to understanding FC performance (Changjun and Shuhai, 2011). It shows the resistance level of the membrane and the source of these resistances. In this thesis study, EIS measurements (Princeton Applied Research, Parstat® 2273 Advanced Electrochemical System, Illinois, USA) were performed four times to show whether the PEMFC was affected by the thaw/freeze cycles. The first one is conducted even after the performance (I-V) curve was saved during the activation process. The 2nd, 3rd, and 4th measurements were recorded after the 10th, 20th, and 30th cold start tests were carried out. EIS measurements were conducted with 0.4 lt/min H_2 and 1.2 lt/min air flow rate conditions. While the EIS study performing, the current should not be drawn from the cell. Thus, the cell was active and operated without current drawn when the EIS study was performed.

Figure 4.3. EIS measurement equipment

4.13. Fluid Flow Analysis

The established setup includes both internal and external flows with gas (H_2 and air) and liquid (ethanol mostly) fluids, respectively. At this point, a fluid flow analysis is required especially for the external coolant cycle due to the heat transfer supplied by this section primarily. Firstly, fluid flow analysis was performed considering the different operating voltages of the pump. Therefore, the coolant cycle was operated at 3, 6, 9, and 12 VDC pump operations. The serpentine channel structure of the back side flow channels leads to pressure drops aforementioned in Section 4.8. In the same section, the flow rates by the coolant cycle are provided in Table 4.2. In evaluating these flow rates, a series of theoretical analyses were conducted. Chapter 8 (Internal Flow) section of the Fluid Mechanics (Çengel and Cimbala, 2020) was followed in the calculations, in general.

4.13.1. Average Velocity

It is known that the fluid velocity in an internal flow is zero at the wall (surface contact points) due to no-slip condition and is maximum at mid-section. The value of the average (mean) velocity usage in the equations is appropriate due to the cross-sectional area of the square duct (flow channels) is constant and the flow type is incompressible (there is no change in density with time). The representation of the square duct shape of the channels is given in Figure 4.4.

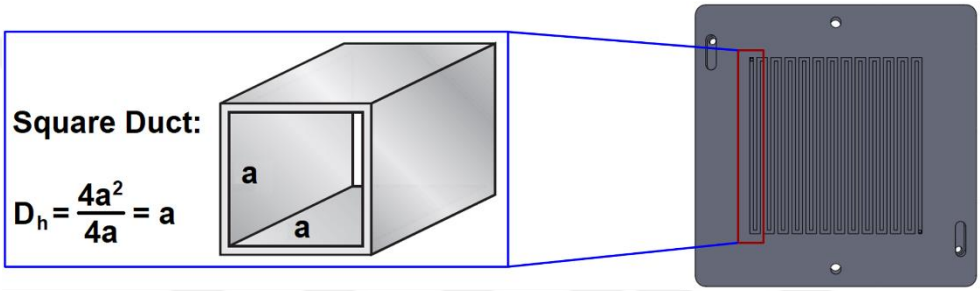

Figure 4.4. Shape details of the square duct flow channels

With the satisfaction of the *Conservation of Mass* principle, The average velocity, V_{avg}, can be determined by the following equation (4.1) where the $\dot{m}$ is the mass flow rate (kg/s), ρ is the density (kg/m^3), V_{avg} is the mean velocity (m/s), and A_c cross-sectional area (m^2).

$$\dot{m} = \rho V_{avg} A_c \tag{4.1}$$

4.13.2. Reynolds Number

The ratio of the inertial forces to viscous forces is known as the Reynolds number (dimensionless) and is calculated by the following equation (4.2) where D_h= characteristic length of the duct (m), v= kinematic viscosity (m^2/s), μ = dynamic viscosity ($Pa.s$).

$$Re = \frac{V_{avg} D_h}{v} = \frac{\rho V_{avg} D_h}{\mu} \tag{4.2}$$

The characteristic length (D_h) is the ratio of the cross-sectional area to the perimeter of the geometry (hydraulic diameter) which is the shape-dependent specification. The hydraulic length calculates by Equation 4.3 since the flow channel geometry has a square duct shape as seen in Figure 4.4.

$$D_h = \frac{4A_c}{p} = \frac{4a^2}{4a} = a \tag{4.3}$$

In our calculations, the characteristic length or hydraulic diameter is 1 mm (0.001 m) and is equal to a side of the flow channel as understood from Figure 4.4. The kinematic viscosities (v) of the fluids were determined as presented in Section 4.2. Therefore, V_{avg} can be calculated since the other parameters given in Equation 4.1 are determined experimentally. Hence, the Reynolds number of the cases also may be specified using the calculated V_{avg} in Equation 4.2. As known, the Reynolds number specifies the flow region as laminar, transitional, or turbulent. Under most practical conditions, the region in an internal flow is divided into groups depending on the Reynolds number as below:

$Re \lesssim 2300$	laminar flow
$2300 \lesssim Re \lesssim 4000$	transitional flow
$Re \gtrsim 4000$	turbulent flow

4.13.3. Entrance Region

The flow characteristics and the formulations depend on the flow region as defined above. One of them is the calculation of the entrance region which indicates the flow region is in the fully developed or hydrodynamic entrance region. The entrance region depends on the flow region and is calculated as presented in Equations 4.4 and 4.5 for the laminar or turbulent regions, respectively. Therefore,

it is calculated that the flow region is whether in a hydrodynamically fully developed region.

$$\frac{L_{h,laminar}}{D} \cong 0.05\, Re \tag{4.4}$$

$$\frac{L_{h,turbulent}}{D} \cong 1.359\, Re^{1/4} \tag{4.5}$$

4.13.4. Pressure Drop

It is obvious that the pressure drop will occur due to the serpentine pattern of the flow fields. Pressure loss is a natural result of the flow and is derived from continuous and minor losses which calculate using Equations 4.6 and 4.7, respectively. Besides, the total pressure loss can be calculated thanks to Equation 4.9 with the help of total head loss (the sum of the continuous and minor losses) calculation by Equation 4.8.

$$\Delta P_L = f\frac{L}{D}\rho\frac{{V_{avg}}^2}{2} \tag{4.6}$$

$$h_L = K_L\frac{V^2}{2g} \tag{4.7}$$

$$h_{L,total} = \left(f\frac{L}{D} + \sum K_L\right)\frac{V^2}{2g} \tag{4.8}$$

$$h_L = \frac{\Delta P_L}{\rho g} \rightarrow \Delta P_L = h_L \rho g \tag{4.9}$$

In the given equations, f denotes Darcy friction factor, and the rest of the equation is the dynamic pressure. Darcy friction factor is determined depending on the Reynolds number which indicates the flow is laminar or turbulent. For laminar flow, it calculates with 64/Re for the circular pipe. However, the friction factor is

calculated by 56.92/Re for laminar flow with the help of Table 8-1 in the Fluid Mechanics book (Çengel and Cimbala, 2020). For the turbulent flow, is calculated by Moody Chart using relative roughness (ε/D) and Reynolds number. The equivalent roughness of the stainless steel (BP material) is $\varepsilon = 0.002$ and the relative roughness is $\varepsilon/D = 0.002$ due to the characteristic length being $D = 1\ mm.$ The intersection point of the relative roughness and the related Reynolds number gives the f Darcy friction factor.

In the minor losses calculation, the loss coefficient, K_L, is given as 1.1 for the 90º miter bend (in Table 8-4 in the Fluid Mechanics book). Because the flow channels include 48 turns with 90º miter bend and 2 turns with 90º miter bend at the inlet and outlet points. In a typical system with long pipes, these losses are minor compared to the head loss in the straight sections (the major losses) and are called minor losses. Although this is generally true, in some cases the minor losses may be greater than the major losses. This is the case, for example, in systems with several turns and valves in a short distance (Çengel and Cimbala, 2020).

4.13.5. Pumping Power

The friction factor for flow in a tube is proportional to the pressure loss. Since the pressure loss along the flow is directly related to the power requirements of the pump to maintain flow, the friction factor is also proportional to the power requirements to overcome friction. The applicable relations are given in Equations 4.10 and 4.11. The pumping power requirement for a laminar-flow piping system can be reduced by a factor of 16 by doubling the pipe diameter.

$$\dot{W}_{pump} = \frac{\dot{m}\Delta P_L}{\rho} = \dot{V}\Delta P_L \tag{4.10}$$

$$\dot{V} = V_{avg} A_c \tag{4.11}$$

Finally, the pumping power is calculated by the equations above. The pumping power is needed to overcome the losses in the duct. The volume flow rate ($\dot{V}, m^3/s$) is equal at the inlet and outlet points of the flow area since the flow is steady and incompressible. The pumping power is determined by the different operating voltages of the pump. The required power to defeat pressure losses is specified for each case. The same process can be characterized by the efficiency of the pump. Equation 4. 12 is used to determine the efficiency of a pump (Chapter 14, Çengel and Cimbala, 2020).

$$\eta_{pump} = \frac{\rho g \dot{V} H}{bhp} \tag{4.12}$$

The pump efficiency is found with the ratio of useful power to the supplied power. This external power ensured to the pump is called the brake horsepower (bhp). The other variables in the equation are presented above. Therefore, the pumping power is calculated in two ways which are the pumping power equation and the efficiency calculation.

4.14. Heat Transfer Analysis

One of the main goals of the thesis is to provide rapid energy to the stack and increase the stack temperature as much possible as quick. That is heat transfer from the fluid to the stack has vital importance to achieving this aim. Herein, the heat is ensured by the electric heater (1800 W) and the coolant is warmed by the heat flux throughout the base contact point. The coolant is warmed by the heater as well as circulated by the pump. Therefore, the heated coolant loses its energy during circulation through the flow channels. At this point, a heat transfer analysis can be conducted to investigate the process analytically and put the heat transfer differences between the cases.

Some values were calculated in the fluid flow analysis section (Section 4.13) since the many points of the heat transfer and fluid mechanics are common and

similar. Chapter 8 (Internal Heat Transfer) of the Heat Transfer book (Çengel and Ghajar, 2020) was followed for the calculations, in general. The average velocity, Reynolds number, hydraulic diameter, entrance length, and pressure drop corresponding to the flow were calculated previously. With the satisfaction of the *Conservation of Energy* principle, the mean (average) temperature (T_m) can be calculated at any point of the fluid. The mean temperature changes in the flow direction by contrast with the average velocity. This can be expressed mathematically as given in Equation 4.13.

$$\dot{E}_{fluid} = \dot{m} c_p T_m = \int_{\dot{m}} c_p T(r) \delta\dot{m} = \int_{A_c} \rho c_p T(r) u(r) dA_c \tag{4.13}$$

The conservation of energy equation for the flow of a fluid in a duct is given in Equation 4.14. At the same time, it is the general heat transfer equation.

$$\dot{Q} = \dot{m}\, c_p\, (T_e - T_i) \tag{4.14}$$

c_p is the specific heat value of the fluid, and T_e and T_i denote exit and inlet temperatures. It should be noted that $\dot{m} c_p T_m$ is represents the energy flow with the fluid. Internal flow in a duct or pipe can be laminar or turbulent depending on the flow conditions and is characterized by the Reynolds number as determined earlier. The heat transfer rate to or from a fluid can be expressed as given in Equation 4.15 from Newton's law of cooling:

$$\dot{Q} = h A_s \Delta T_{avg} = h A_s (T_s - T_m)_{avg} \tag{4.15}$$

where h is the average convection heat transfer coefficient, A_s is the surface area corresponding to heat transfer (it is equal to $a^2 L$ for a square channel of length L), and ΔT_{avg} is the appropriate average temperature difference between the fluid and the surface. ΔT_{avg} can be found in two ways; the first one is the arithmetic mean

temperature difference (ΔT_{am}), and the second one log mean temperature difference (ΔT_{lm}). It is known that the log mean temperature is a better way to estimate the temperature conditions of the fluid. However, the exit temperature of the coolant was calculated in two ways and compared. In calculations, the average temperature of the inlet and outlet conditions of the coolant was considered which is called *bulk mean fluid temperature* ($T_b = (T_i + T_e)/2$). Herein, the mean coolant temperature can be estimated by Equation 4.16.

$$T_e = T_s - (T_s - T_i)\, exp(-hA_s/\dot{m}c_p) \tag{4.16}$$

The ratio of $hA_s/\dot{m}c_p$ is known as NTU (number of transfer units) is a dimensionless number that measure of the effectiveness of the heat transfer systems. It indicates the saturation level of the system against heat transfer. Thus, it is a measure of the limitation of heat transfer. The NTU of the proposed mechanisms were calculated separately. In this case, the cooling law (Eq. 4.15) can be rearranged as presented in Equation 4.17 and the log mean temperature difference, ΔT_{lm} can be determined with the help of Equation 4.18. The calculations can be performed under constant surface temperature conditions since the heated surface (stack surface) is maintained at a constant temperature.

$$\dot{Q} = hA_s\Delta T_{avg} = \dot{Q} = hA_s\Delta T_{lm} \tag{4.17}$$

$$\Delta T_{lm} = \frac{T_i - T_e}{\ln[(T_s - T_e)/(T_s - T_i)]} = \frac{\Delta T_e - \Delta T_i}{\ln(\Delta T_e/\Delta T_i)} \tag{4.18}$$

The log mean temperature difference should always be considered when determining the convection heat transfer in a duct whose surface is maintained at a constant temperature T_s. The laminar or turbulent flow region is specified by Reynolds number as indicated in the previous section. Similarly, pressure drop and pumping requirements were calculated previously. The heat transfer coefficient, h

calculation is changed with the region of the flow. Herein, the heat transfer coefficient can be calculated with the help of *Nusselt Number* calculation as presented in Equations 4.19 and 4.20 for the laminar and turbulent flow conditions, respectively.

$$Nu = \frac{hD_h}{k} = 3.66 + \frac{0.065(D/L)RePr}{1 + 0.04[(D/L)RePr]^{2/3}} \tag{4.19}$$

$$Nu = \frac{hD_h}{k} = 0.023Re^{0.8}Pr^{n} \tag{4.20}$$

Actually, the Nusselt number can be calculated thanks to different equations from the present. Yet, suitable relations were preferred matching the coolant specifications. For instance, Equation 4.19 is assigned due to the Prandtl number specification of the coolant at sub-zero temperatures. In Equation 4.20, n coefficient of the Prandtl number should be 0.4 for the heating application (it assumes as 0.3 for the cooling).

As an extra heat transfer parameter, the number of transfer units (NTU) is a measure of the heat transfer area and the effectiveness of a heat transfer system was calculated for each parameter. The NTU calculation is provided using Equation 4.21.

$$NTU = hA_s/\dot{m}c_p \tag{4.21}$$

Therefore, the total heat transfer supplied by the coolant cycles through the cases was determined with the calculation of heat transfer coefficient h, theoretically. In addition, a heat transfer analysis was conducted on the pump operating voltage study. Herein, the coolant was heated to 40 °C and sent to the stack with different operating voltages of the pump.

5. RESULTS AND DISCUSSION

5.1. Activated MEA Performance

The I-V curves before and after the activation process are given in Figure 5.1. The open circuit voltage (OCV) of the MEA was 0.9 levels before activation. However, it evolved at 0.97 levels after the activation process. Polarization curves were recorded with 0.03 voltage steps. Maximum 22 A and 4.77 W power values were obtained before the activation process. With the MEA activation, the current and the power were improved and reached 25 A and 5.39 W values, respectively. Thence, all cold start tests were performed with the activated MEA.

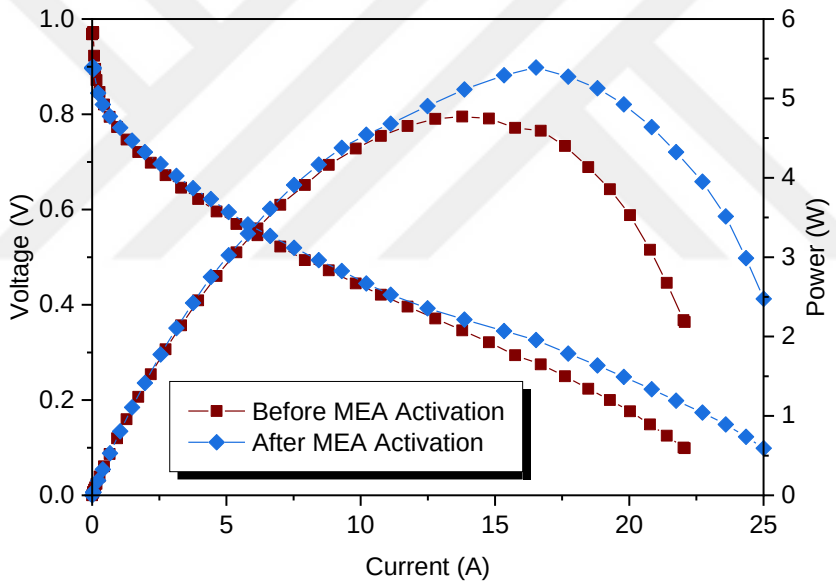

Figure 5.1. Polarization curve of the activated MEA

5.2. Viscosity Measurements

Viscosities of the prepared aqueous solutions of the working fluids were measured five times per sample, and the average is multiplied by the “C” coefficient of the viscometer capillary glass tube. The measurements were performed at 40 °C

with the agreement in the certificate of calibration of the glass capillary tube. The findings (measurement durations) are illustrated in Table 5.1.

Table 5.1. Viscosity measurement durations of the pure coolant fluids and their aqueous solutions

Substance	#1 (s)	#2 (s)	#3 (s)	#4 (s)	#5 (s)	Ave. (s)
Ethanol	83.32	83.24	83.69	83.03	83.60	83.376
Ethanol-Water (80-20%)	109.67	109.45	109.69	109.46	109.57	109.568
Methanol	41.47	41.5	41.48	41.49	41.48	41.484
Methanol-Water (80-20%)	68.9	68.85	68.73	68.93	68.86	68.854
Ethylene Glycol	-	-	-	-	-	-
Ethylene Glycol-Water (80-20%)	496.41	496.34	496.42	496.37	496.39	496.386
Propylene Glycol	-	-	-	-	-	-
Propylene Glycol-Water (80-20%)	541.93	541.74	541.82	541.89	541.81	541.838

The viscosities of the pure ethylene glycol and pure propylene glycol were not determined due to the dense structure of the fluids. However, the viscosities of the aqueous solutions were calculated as seen in the table.

The average of the five measurements was determined and the average is, then, multiplied by the “C” coefficient. Therefore, the kinematic viscosities of the pure substances and the aqueous solutions were obtained as illustrated in Table 5.2. In addition, kinematic viscosities (at room temperature) of the pure fluids supplied by the manufacturing companies are given in the same table.

The measured data is in agreement with the raw data by the manufacturer. It is seen clearly by the ethanol and methanol measurements. However, the viscosities of the pure ethylene glycol and propylene glycol were not measured by the implemented measurement system.

Table 5.2. Measured kinematic viscosity values of the fluids and raw data comparison

Substance	Kinematic Viscosity, *v* (m^2/s, $x10^{-6}$, measured, 40 ºC)	Kinematic Viscosity, *v*, (m^2/s, $x10^{-6}$, manufacturer data, room temp.)
Ethanol	1.207	1.2
Ethanol-Water (80-20%)	1.587	-
Methanol	0.6	0.54-0.59
Methanol-Water (80-20%)	0.997	-
Ethylene Glycol	-	-
Ethylene Glycol-Water (80-20%)	7.188	-
Propylene Glycol	-	-
Propylene Glycol-Water (80-20%)	7.847	-

It is obvious that the viscosities of ethylene glycol and propylene glycol are low and it aggravates the measurements. At this point, it can be concluded that the existing measurement system may not be appropriate for the viscosity measurements of these types of fluids. On the other hand, the viscosities of the aqueous solutions of the same fluids were determined, successfully. Thus, pure water added to the substances decreased the viscosity level of the solutions and enable measurement by the glass capillary tube system.

It should be noted that the viscosities of the fluids decrease with the increase in measurement temperature. Thereby, it was expected that the measured values should be lower than the raw data. However, the values are pretty close as understood from the table. The environmental conditions (such as air pressure and density), ambient temperature, the competence and capability of the measurer, measurement errors (inaccuracy of the measuring instruments, unstable decision on the time tracing), etc. should be considered when evaluating the measurement values.

5.3. Density Measurements

The density measurements of the pure substances and the aqueous solutions (80-20% in wt.) were performed at room temperature and each measurement was repeated five times. The average of the measurements is evaluated as the density of the fluid. The measurement results are tabulated in Table 5.3.

Table 5.3. Measured density values of the fluids and raw data comparison

Substance	Density, ρ (kg/m^3, measured, room temp.)	Density, ρ (kg/m^3, manufacturer data, room temp.)
Ethanol	786.6	792
Ethanol-Water (80-20%)	853.8	-
Methanol	788.8	790
Methanol-Water (80-20%)	862.6	-
Ethylene Glycol	1114.3	1113
Ethylene Glycol-Water (80-20%)	1093.4	-
Propylene Glycol	1033.8	1030
Propylene Glycol-Water (80-20%)	1029.3	-

The densities of the pure substances are in agreement with the raw data supplied by the manufacturer. Besides, the densities of the aqueous solutions were calculated values between pure water and substance densities. The densities of the aqueous solutions of the ethylene glycol and propylene glycol are quite higher than the ethanol and methanol solutions, as in the viscosity measurements.

Physical specifications of the pure working fluids were presented in the previous section in Table 3.3. Herein, the specifications of the aqueous solutions of the working fluids are presented in Table 5.4. The melting and boiling points of the solutions were saved from the literature; ethanol (Website, 2023h), methanol (Website, 2023i), ethylene glycol (Website, 2023j), propylene glycol (Website, 2023k). It is seen that the freezing and boiling points of the aqueous solutions of the

prepared working fluids are in the appropriate range for both operations at normal conditions and cold start operations. With the mixture, the freezing points of the ethylene glycol and propylene glycol coolants decreased. Also, the boiling point of the methanol mixture increased and reached 83 ℃ while the ethanol solution was not affected by the mixture ratio.

Table 5.4. Physical specifications of the aqueous solutions (80-20% in wt. with pure water) of the working fluids

Working Fluid	Freezing Point (ºC)	Boiling Point (ºC)	Density (kg/m^3)	Viscosity (m^2/s, $x10^{-6}$)
Ethanol	-70	78	853.8	1.207
Methanol	-87	83	788.8	0.6
Ethylene Glycol	-46	127	1114.3	7.188
Propylene Glycol	-82	110	1029.3	7.847

A working fluid with high density and high viscosity properties is nonpurposive for the cold start operation. Because the heating fluid should be delivered easily and carry high heat transfer specifications to provide a quick cold start. From the point of view of viscosity and density measurements, the aqueous solutions of the ethanol and methanol were evaluated as more appropriate than the ethylene glycol and propylene glycol solutions considering the cold start requirements.

5.4. Self-Stack Operation without Assist

Two tests were conducted at -10 °C to characterize the cold start capability of the cell without any assistance. All figures were created using Origin commercial software (Origin 2019b Graphing & Analysis). The obtained results are presented in Figure 5.2. In the first test, the cell was operated at 0.4 constant voltage and the current was drawn when the cell temperature reached -10 °C. The current (Figure 5.2-b), voltage (Figure 5.2-c), and temperature profile throughout the cell (Figure 5.2-d) distributions were given. The cell quickly generated current at the initial stage and improved with time. It reached 1.64 A maximum current at 225 s and decreased

linearly to zero in 26 seconds after reaching a peak point. On the other hand, the unstable and fluctuant increase was recorded in the temperature profile, at the initial stage of the test. Nonetheless, it increased throughout the current generation in the cell and reached -7.5 °C at 250 s. With the current generation stopped and the voltage dropped to zero, the temperature is turned to the negative side again. After this point, the cell was dragged to an irremediable position to survive.

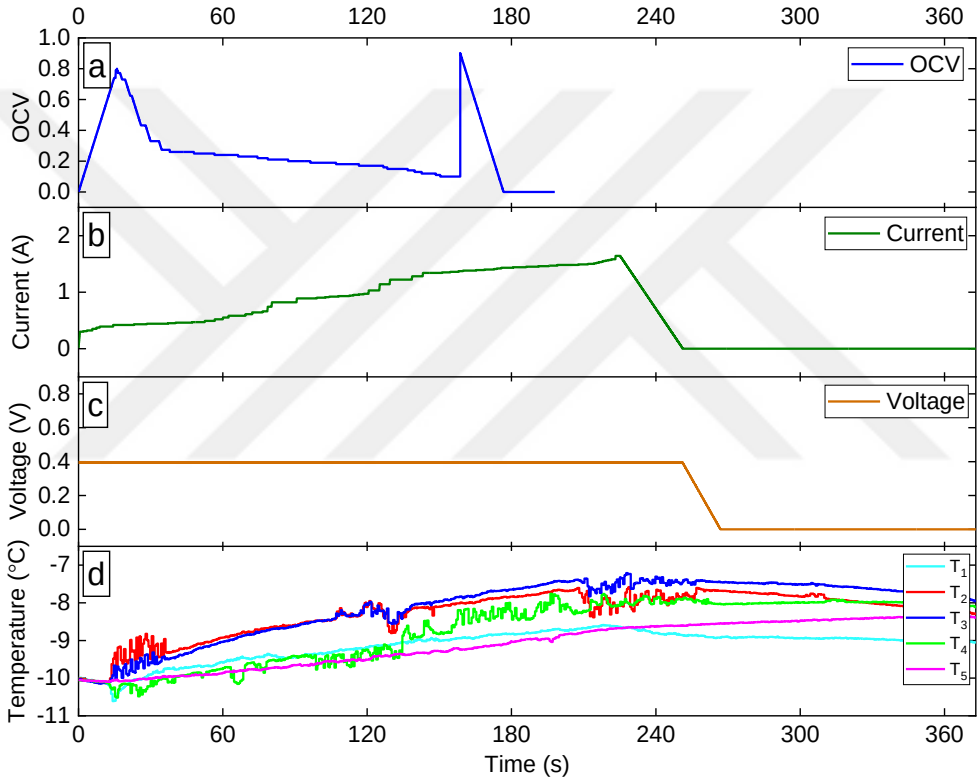

Figure 5.2. Dry membrane test without an assist; a) only OCV follow, b) current, c) main voltage, d) time-temperature profile during the test

Similar behaviour was observed with the OCV pursuit without the current drawn as depicted in Figure 5.2-a. The OCV increased to 0.79 V as soon as H_2/air gas was supplied to the cell and then it decreased gradually to 0.28 V levels. It slowly decreased to 0.1 V during the next 100 seconds and then it arrived at zero even

though it attacked with the last move to rise. The importance of the current drawn was revealed with the comparison of the performed tests on behalf of a cell operation at sub-zero temperature. The current drawn increased the cell operation duration dramatically before it drop zero (Figure 5.2-a and Figure 5.2-c comparison). It was proved with the two initial cold start tests that the cell may not be survived without any assistance. The self-operate of the single-cell test was not repeated at lower temperatures than -10 °C since it is estimated that similar trends will be observed.

5.5. Equal Heating of Anode and Cathode Sections

The time-temperature figure regarding the test is shown in Figure 5.3. Anode-cathode inlet and anode-cathode outlet temperatures were found in agreement. The temperature was -10 ºC at the initial stage of the test. Then, it increased above zero instantaneously at the inlet points with the effect of hot ethanol circulation. Outlet points arrived above zero temperatures with delay, naturally. However, outlet points achieved hotter temperatures than inlet points with time. The temperature decreased gradually after reaching a peak point since the coolant is not heated, and then the test was completed.

Herein, it is proved that the anode and the cathode compartments are heated equally. This validation has important to evaluate case studies accurately. Otherwise, a section (anode or cathode) may provide a higher warm-up than the other, and thence it may cause misinterprets in the results.

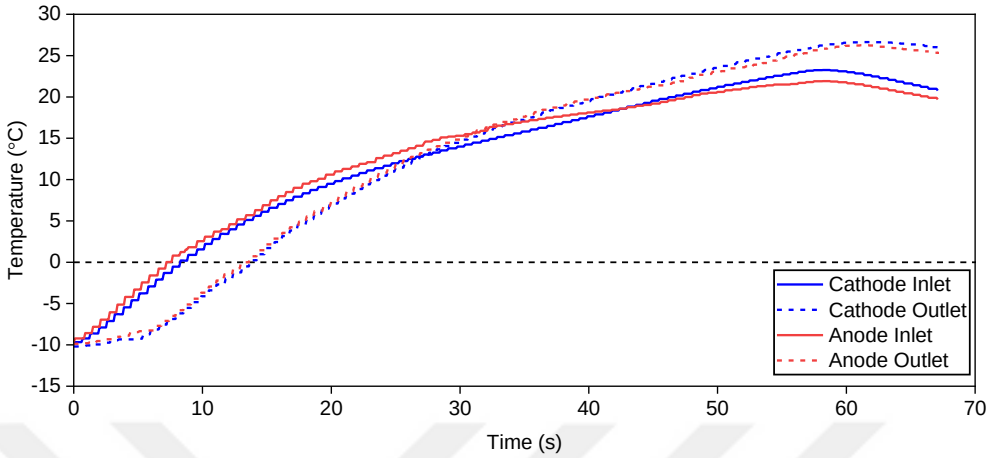

Figure 5.3. Anode and cathode temperatures during the initial warm-up cycle

5.6. Optimum Coolant Selection

The heater operated for 20 s and the coolant was circulated for 150 s to specify the best coolant which provides the most efficient, rapid, and homogeneous temperature distribution at -10 °C cold start tests. Time-temperature, voltage and current values of the aqueous solutions of the working fluids were depicted separately, and their specifications were discussed.

5.6.1. Cold Start with Ethanol Cycle

The aqueous solution of the ethanol (20:80% in wt.) characterization is presented in Figure 5.4. The temperature reached above zero within 15 seconds (at mid-sections of the cell) and increased to 30 °C levels. After the pump was shutdown, the temperature gradually decreased and kept its position at 12-13 °C around. The warmer temperature profile was achieved by a long heater operation duration, as expected. And, the highest temperature difference was experienced in this case study considering the pump shutdown and the temperature stabilization range. Another affirmative feature of the ethanol cycle is the climbing tendency of the current. The current slightly increased after the temperature stabilization was supplied in the cell. This tendency provided promising insight into the temperature and current profile in the continuation of the test.

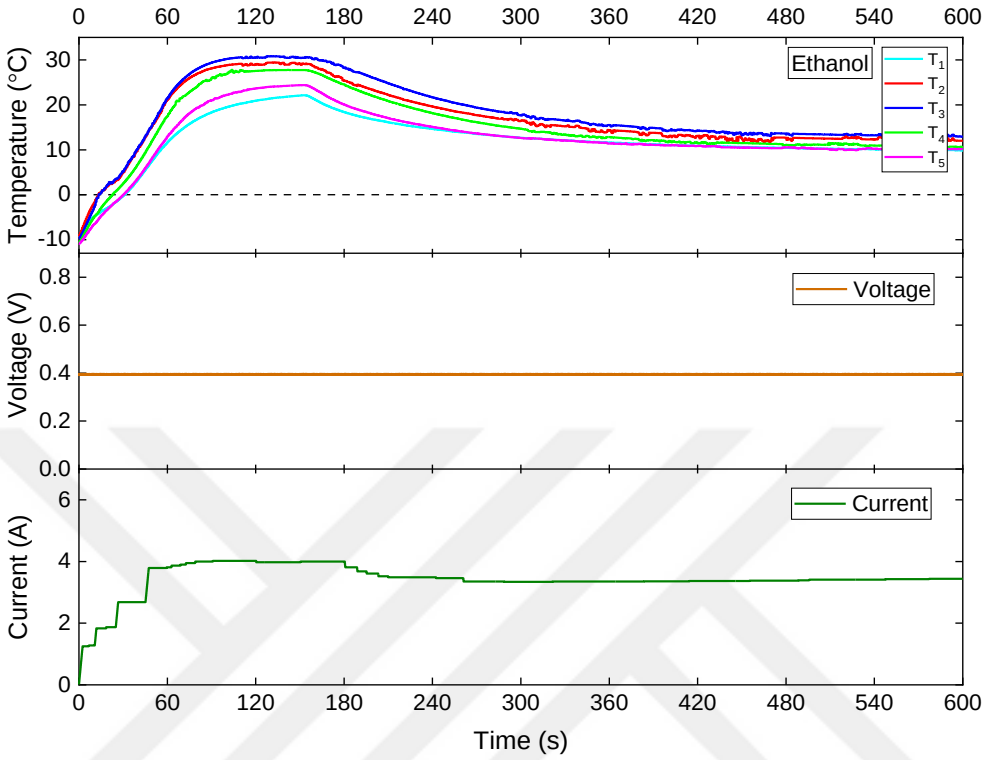

Figure 5.4. Temperature-Voltage-Current vs. Time graphs of the ethanol coolant operation

5.6.2. Cold Start with Methanol Cycle

The aqueous solution of the methanol (20:80% in wt.) characterization is demonstrated in Figure 5.5. The methanol coolant has performed a worse temperature increase profile than the ethanol cycle. The temperature raised 17-18 °C grades maximum, and then the generated heat by the cell operation kept the cell temperature at ~10 °C. In addition, the cell reached above zero within 14.6 s.

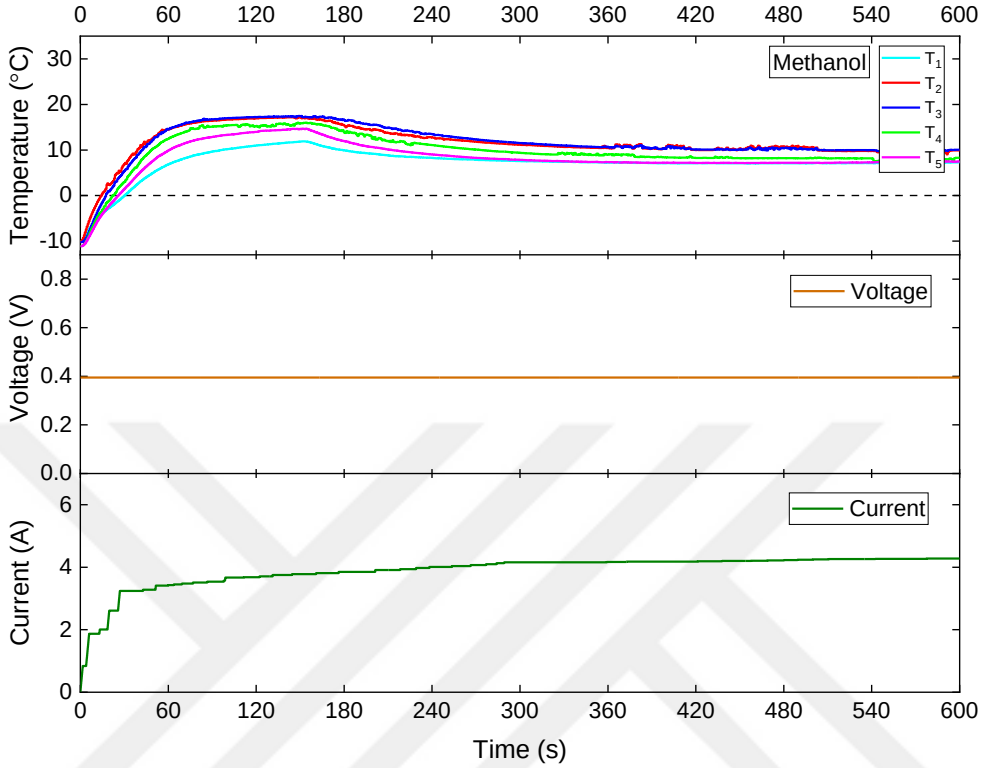

Figure 5.5. Temperature-Voltage-Current vs. Time graphs of the methanol coolant operation

The current was generated throughout the test. The current was 4 A levels during the test and it was above 4 A when the test was completed (4.28 A). The temperature was 10 °C at the mid-sections and 7-8 °C levels at the side-sections. When compared to the ethanol cycle, nonetheless, the more stable temperature profile was supplied by methanol coolant operation. The temperature difference between the reached highest value and the temperature at the end of the test is ~10 °C.

5.6.3. Cold Start with Ethylene Glycol Cycle

Time-temperature, voltage, and current follow of the aqueous solution of the ethylene glycol (20:80% in wt.) are illustrated in Figure 5.6. The ethylene glycol exhibited a performance between ethanol and methanol coolants. The temperature

rose above zero at the mid-sections within 25.6 s. The time required to reach zero is very long when compared to the ethanol and methanol cycles. 22.5 ℃ maximum temperature was achieved and the test was completed at 8 ℃ at mid-section (also ~5-6 ℃ levels at the sides).

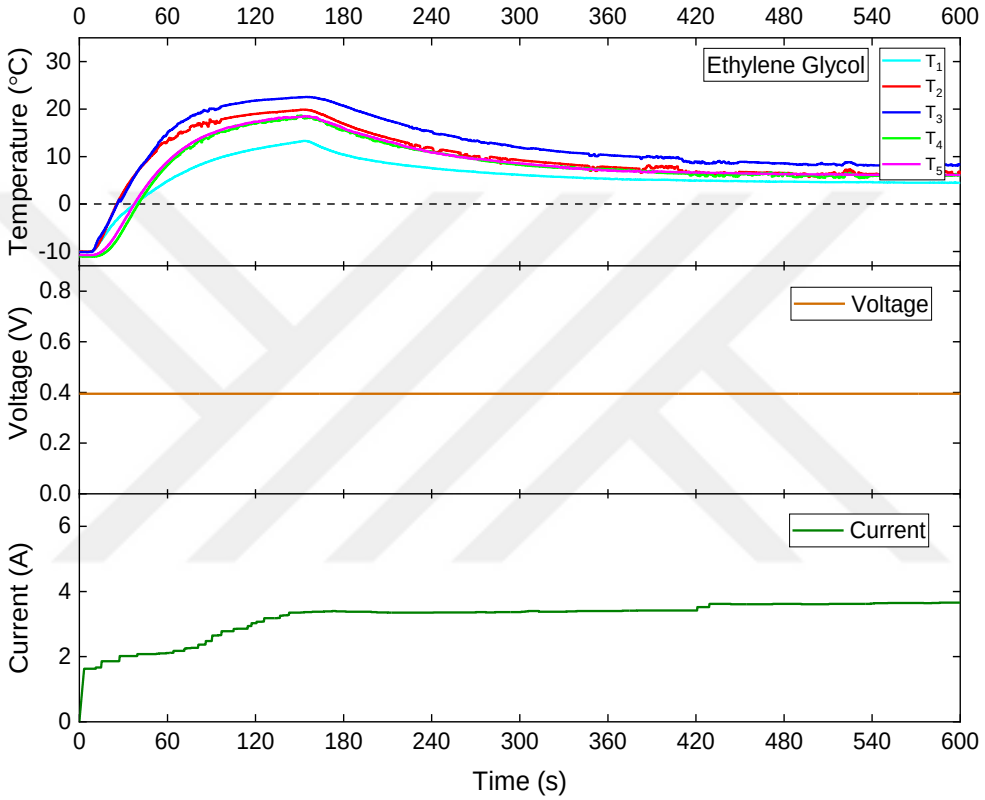

Figure 5.6. Temperature-Voltage-Current vs. Time graphs of the ethylene glycol coolant operation

It was reported that the mixture was driven formidably by the pump due to the non-viscous and dense structure of the ethylene glycol-water solution. The delay in the time to achieve zero originated from the density and viscosity relations of the mixture. Even, the flow channels may be choked and blocked by the mixture particles. Furthermore, the flow rate of the delivered fluid is decreased due to similar reasons. Nevertheless, a successful cold start operation was achieved at -10 ℃

against all the odds. It is obvious that the ethylene glycol-water mixture is not a suitable coolant (heating fluid) for the cold start operation especially in harsh conditions than -10 ℃.

5.6.4. Cold Start with Propylene Glycol Cycle

The triple graph of the cold start performance of the propylene glycol solution coolant is illustrated in Figure 5.7. At first view, fluctuating and unstable temperature profiles attracted attention. The cell reached zero within 23 seconds and 19.4 ℃ of maximum stack temperature was achieved.

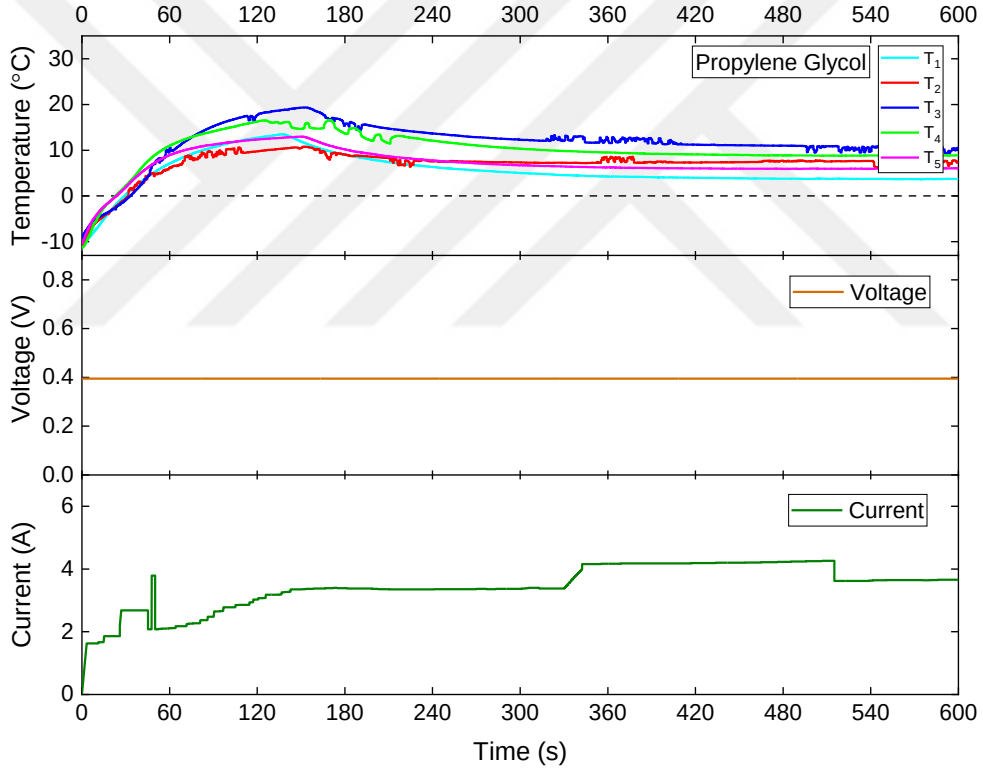

Figure 5.7. Temperature-Voltage-Current vs. Time graphs of the propylene glycol coolant operation

The cell act unstable after the pump was shutdown, especially. Nevertheless, the cell completed the test above 10 ℃ at the mid-section. The other regions were 7-

8 ℃, and the only inlet region decreased to 3.7 ℃ levels. The current was generated through the cell throughout the test. The current was climbed -like a current ramp- at the initial stage, and a long duration was completed at 4.25 A. Then, the current decreased to 3.62 levels, and the test was finished at 3.7 A.

Undoubtfully, the ethanol solution is the most attractive and appropriate working fluid to provide enhanced cold start operation as examined in the figures. Slightly lower performance measurement was saved with the methanol cycle when compared to the ethanol cycle. On the other hand, it was reported that the aqueous solutions of ethylene glycol and propylene glycol are not satisfied the required viscosity and heat transfer coefficient. Therefore, the rest cold start tests were performed using the ethanol-water solution. The pre-test results of this section were published in a conference paper (Topcu et al., 2021b).

5.7. Effect of Pump Operating Voltage

The pump consumed energy during its operation since is an electronic device. Firstly, the pump operation conditions were tested on the behalf of proposing an energy-saving method. All time-temperature figures regarding the operating voltages are presented in Figure 5.8. Temperature pursues of the 3V pump operation are given in Figure 5.8-a. The temperature increased above zero at the inlet and outlet points after 38 and 82.6 seconds, respectively. The low operating voltage has resulted in a low coolant flow rate (0.15 lt/min). Heat transfer between the coolant and the bipolar plates is carried out slowly, naturally. Consequently, the low voltage operation was failed and pointed out as an ineffective way to heat the stack.

On the other hand, similar and successful trends were observed at 6, 9, and 12 VDC operations. The temperature increased above zero at the inlet points in less time than 10 seconds for all three cases. Similarly, outlet points arrived above zero temperatures in less time than 20 seconds. However, outlet temperatures exceeded the inlet temperatures with time.

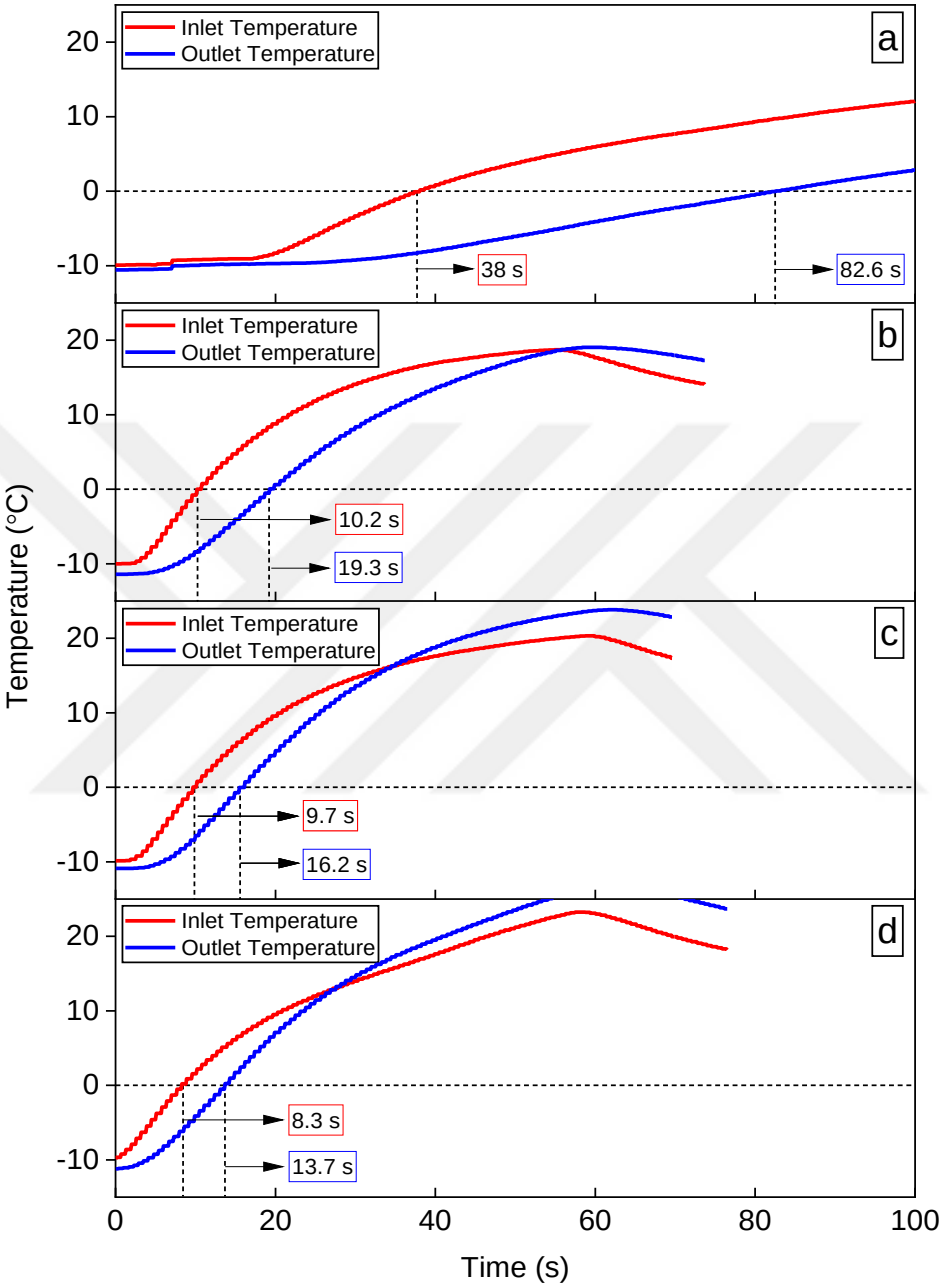

Figure 5.8. Time-temperature figures concerning the pump operating voltage; a) 3VDC, b) 6VDC, c) 9VDC, d) 12VDC

Although no significant difference is not recorded between the cases, the 12VDC pump operation is provided the most effective heating way, as expected. High coolant flow rates ensure high and fast heat transfer. The temperature reached 23.3 and 26.6 ºC respectively at the inlet and outlet points for 12VDC operation. 23.8 ºC maximum temperature was achieved for 9VDC operation while 19 ºC was obtained with 6VDC. Temperature levels decreased with the operating voltage drops. 6VDC pump operating voltage may be preferred around the -10 ºC cold start temperatures instead of 9 or 12VDC to decrease the energy consumption level of the equipment. Nevertheless, full pump power (12VDC) may be interiorized at harsh conditions (-20, -30 ºC) to provide rapid warm-up. The pre-test results of this section were published in a conference paper (Topcu et al., 2020).

It should be remembered that the single-cell was not operated during the pump operating voltage tests. Therefore, the stack was warmed up only with the effect of the coolant loop. Besides, stepped increased temperature values are observed in Figures 5.3 and 5.8. Relatively limited (5 data/second) temperature data collection is the primary reason for this problem. Therefore, this problem was eliminated with the collection of more data (100 data/second) in the next tests.

5.8. Optimum Stack Heating Method

5.8.1. Self-Anode Heating Strategy

The temperature, voltage, and current profiles corresponding to self-anode heating with 9VDC and 12VDC pump operations were given in Figures 5.9 and 5.10, respectively. Firstly, the cell properly operated at 0.4 constant voltage as understood from the figures. Even though the cell is not available at the initial stage of the tests with 9VDC operation, shortly after the cell produced electricity and the current was drawn during the test. Herein, the current was recorded at 1~2 A levels. The drawn current increased towards the end of the test, especially. However, it was understood from the temperature profile that the method cannot apply at both the start and maintenance steps. The temperature arrived above zero for the first time after 99

seconds at the mid-section of the bipolar plate. It is a highly long time in terms of the cold start operation. Also, the maximum temperature was recorded as 8.8 ºC in the middle sections. The temperature maintained a decremental position after ~200 seconds. Although the cell generated current, the temperature decreased gradually and reached below zero. The temperature decreased below zero at side-sections earlier than the mid-section. This situation proved the importance of heat generation by the cell. However, it is predicted that the current generation in the cell will decrease and finally stop if the test continued. Because occurred water particles freeze at sub-zero temperatures in the flow channels and barrier to gas transmission.

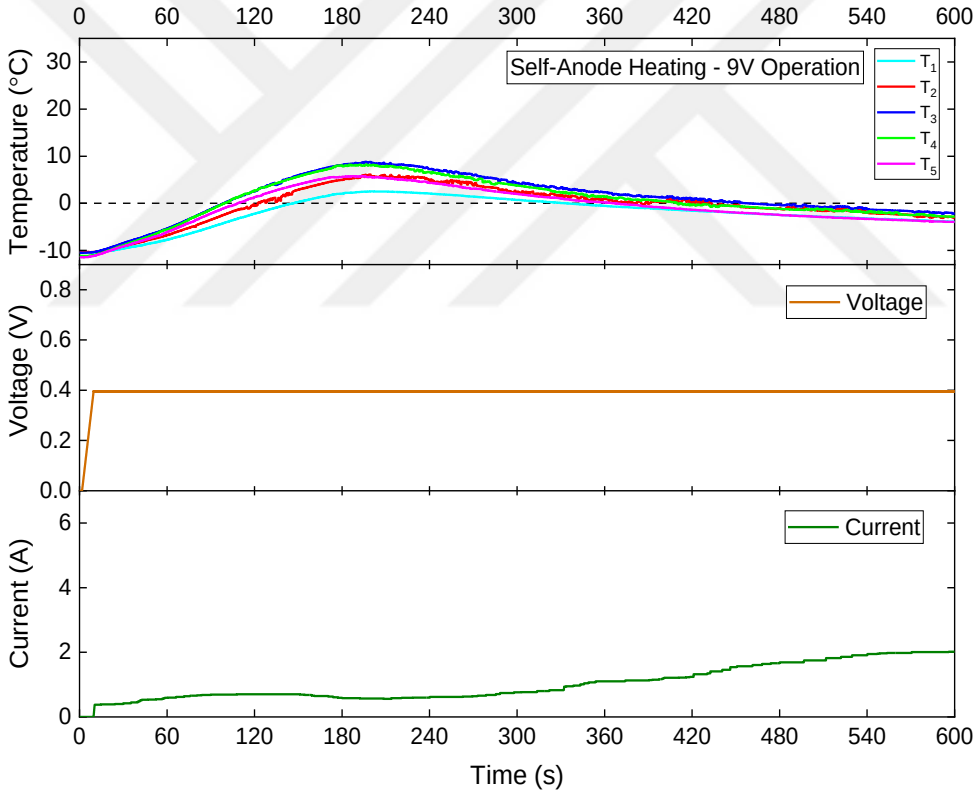

Figure 5.9. Temperature-Voltage-Current vs. Time graphs of the self-anode heating strategy with 9VDC pump operation

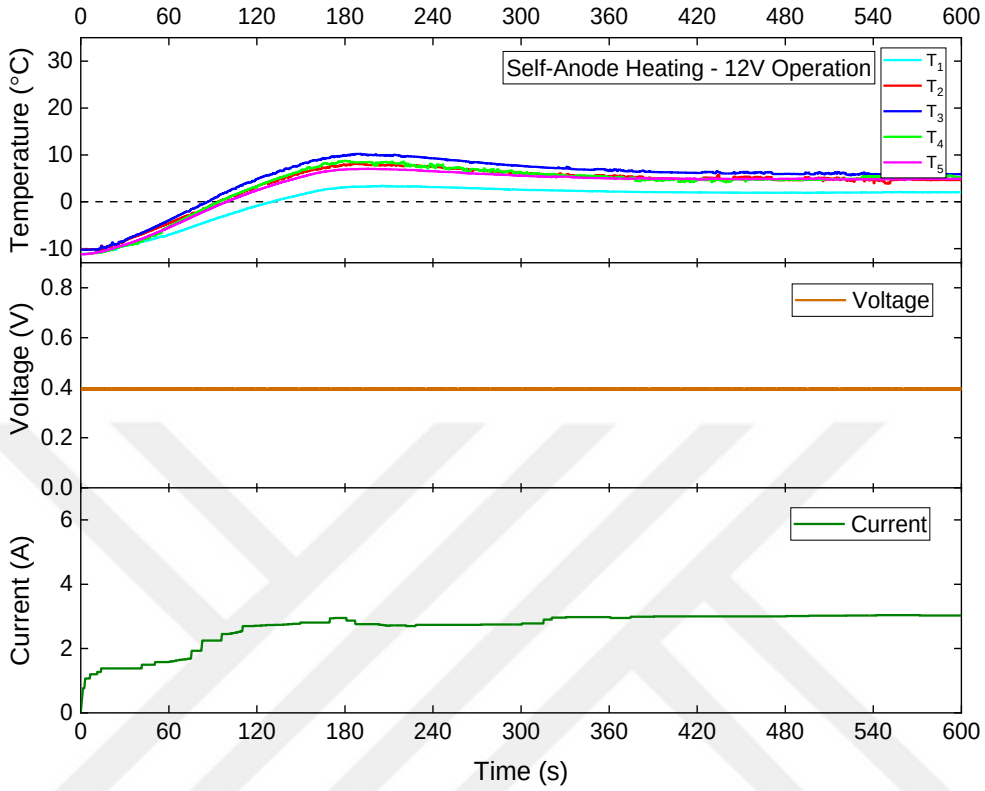

Figure 5.10. Temperature-Voltage-Current vs. Time graphs of the self-anode heating strategy with 12VDC pump operation

On the other hand, a relatively more succeeded temperature and current profile were provided with the 12VDC self-anode operation. The temperature maintained its position above zero till the end of the test. In addition, the cell improved the current level step by step. Nevertheless, heat transfer provided from the anode to the cathode side is not an effective way. Because the supplied heat should warm up the anode bipolar plate, membrane layers, and cathode bipolar plate. In addition, membrane temperature may be a bit amount warmer than the measured value since the measurements were performed by the cathode bipolar plate. Nonetheless, it is valid for all tests. In a conclusion, the self-anode heating method was referred to as an unsuitable method due to the insufficient heat transfer to heat the whole stack and maintain the reactions.

5.8.2. Self-Cathode Heating Strategy

The temperature, voltage, and current profiles regarding self-cathode heating with 9VDC and 12VDC pump operations were demonstrated in Figures 5.11 and 5.12, respectively. The cell generated electricity at 0.4 constant voltage operation during the tests. The current level increased above 4A in the middle of the test and maintained its position at ~4A until the test ended for the 9VDC operation.

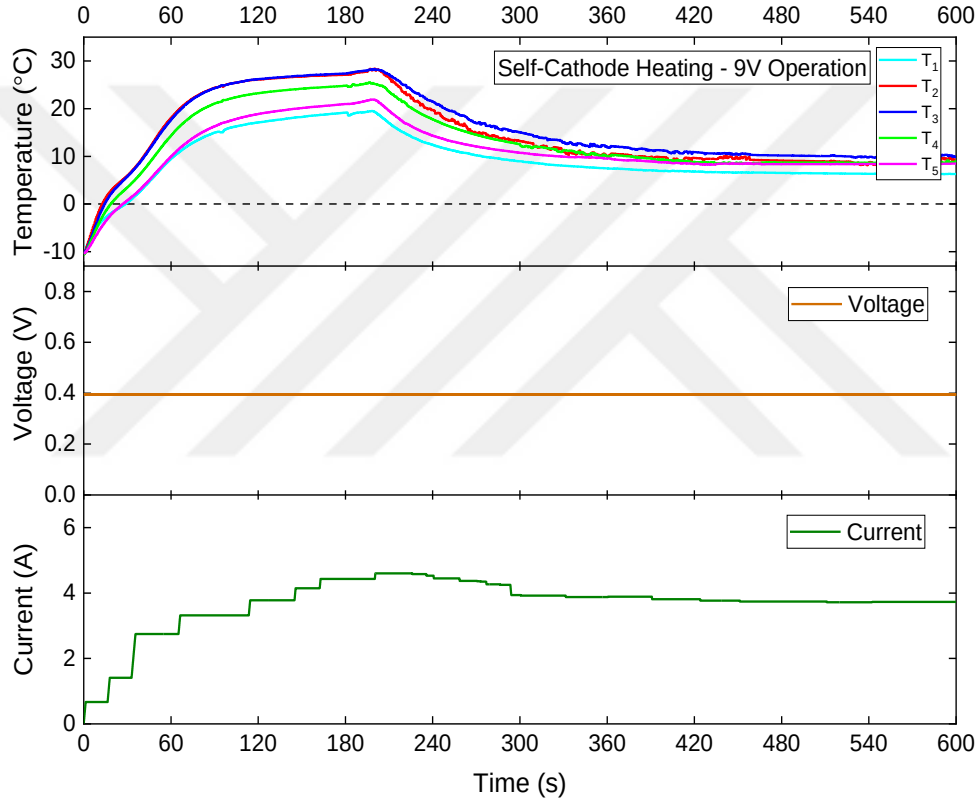

Figure 5.11. Temperature-Voltage-Current vs. Time graphs of the self-cathode heating strategy with 9V pump operation

On the other hand, in the 12VDC operation, the current value approached 6A and hold its state at ~4A. The current curve characteristics of these strategies are highly close and match. However, the temperature distribution curves revealed the quick heat potential of the 12VDC operation. The temperature reached above zero

in only 11.2 seconds (T_1 point), and the stack arrived at 33.4 ºC maximum temperature and hold its state at ~7-8 ºC to the end of the test.

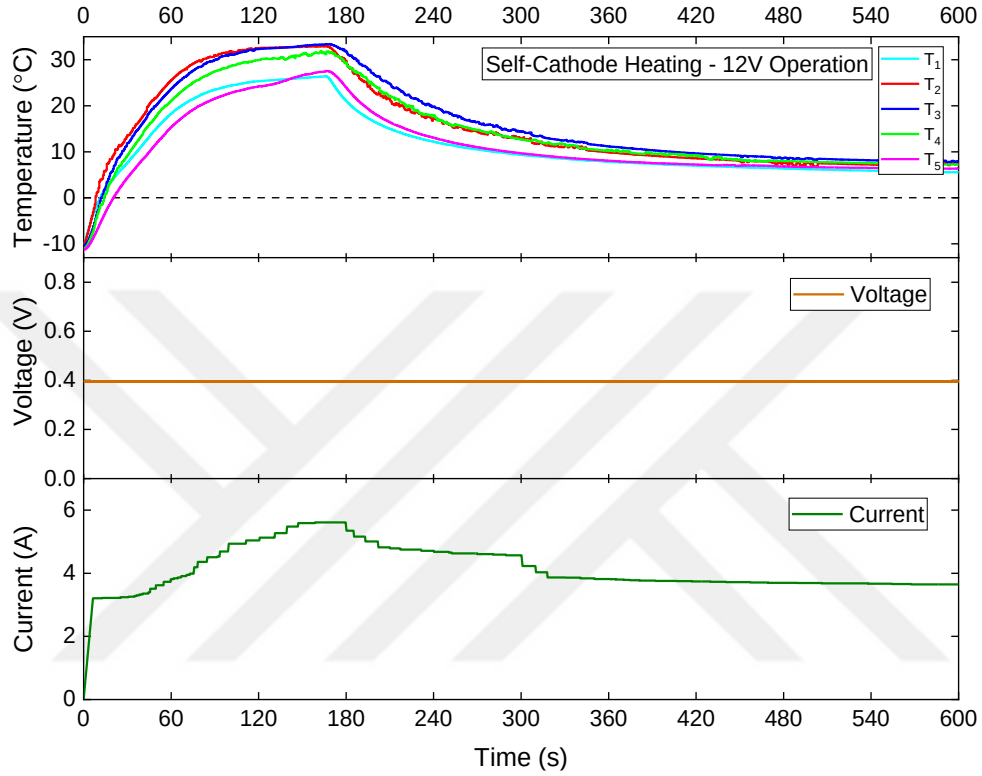

Figure 5.12. Temperature-Voltage-Current vs. Time graphs of the self-cathode heating strategy with 12VDC pump operation

The self-cathode heating method is more successful than the self-anode approach in every aspect. The approach ensured a fast warm-up and improved current. Besides, the temperature profiles confirmed the cold start capability of the self-cathode heating way. In this context, it should be considered that the generated heat by the cell contributed to the instant temperature increase at the cathode side. The combined effect of the heat sources accelerated both the temperature rise and the current generation development. On the contrary, lack of the powerful heat flow density led to cold start failure for the self-anode heating process. In addition, direct

application of the abrupt coolant cycle to the cathode side (since the temperature follows was provided by this side) facilitated the heat transfer in this section.

5.8.3. Double-Side Heating Strategy

The temperature, voltage, and current profiles regarding double-side heating with 12VDC pump operation were presented in Figure 5.13. A highly smooth temperature profile was obtained with the double-side operation as seen in Figure 10. The temperature increased above zero in only 13.3 seconds (T_3 point), and the stack arrived at 30.8 ºC maximum temperature and kept its status at 13 ºC to the end of the test. The temperature heating profile of the double-side heating method has similar trends compared to the 9VDC pump operated self-heating approach. However, temperature lines after the pump shutdown are better than the whole other operations. The cell kept its temperature at 13 ºC levels in this section. This value is pretty well according to the self-anode and the self-cathode heating methods. The time to above zero is lower than the self-cathode method. Therefore, the importance of beginning with the self-cathode approach is evidenced to obtain rapid temperature increase.

The current increased to 4A levels and maintained its position until the end of the test. When analysing the current profile, it was remarked that the current has an increasing tendency. The current level is not increased as became in the self-cathode method. However, the smooth passage of current could be contributed to the temperature increase in this method. This means that the current increased instantaneously to 6A levels in the self-cathode method. Then, decreased to 4A levels and maintained its decreased position to the end of the test. Similarly, a sharp drop was experienced in the temperature profile in parallel with pump shutdown and current decreases. And, this decremental position continued to the end as in the current profile.

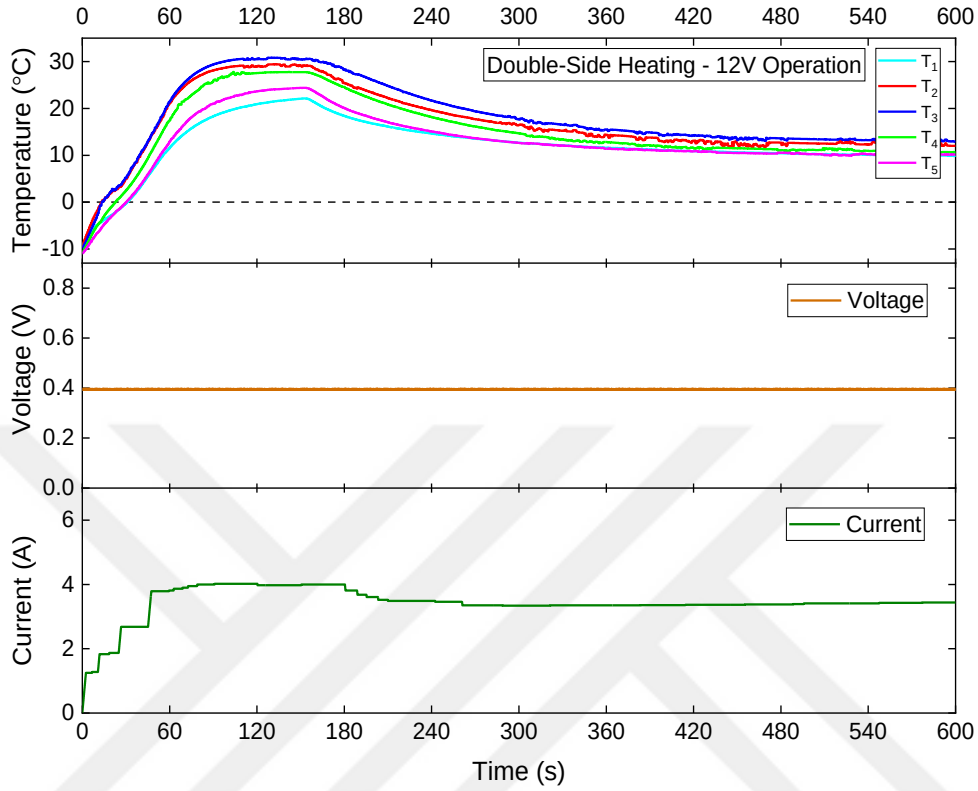

Figure 5.13. Temperature-Voltage-Current vs. Time graphs of the double-side heating strategy with 12V pump operation

On the other hand, a sharp decrease is not performed with the double-side heating strategy as seen in Figure 5.13. The current level kept its position during the test. At this point, the protection of the current level may be promoted to the temperature preservation in the cell as different from the self-cathode heating method. The temperature difference at the maximum and the end of the test is determined as 25.4 ºC for the self-cathode method. The same difference is found as 17.8 ºC for the double-side heating method. Therefore, the success of this method is certified by this calculation. Moreover, the importance of the current level of temperature maintenance in the cell is highlighted. The pre-test results of this section were published in a conference paper (Topcu et al., 2021c).

5.9. Effect of Heater Operation Duration

5.9.1. Case #1 – 10 s Heater, 150 s Pump Operation

Temperature distribution, voltage, and current following graphs were presented in Figure 5.14. In the first case, the heater and the pump were operated for 10 and 150 seconds, respectively. The cell generated electricity and the current was drawn successfully. The cell temperature increased above zero within ~18 seconds and reached ~18 °C maximum temperature. The cell temperature gradually decreased after the pump shutdown and maintained its position at 8-9 °C levels until the test was completed. The voltage stayed in a stable position at 0.3 V and the current increased to 3.3 A maximum and continued at 3 A levels.

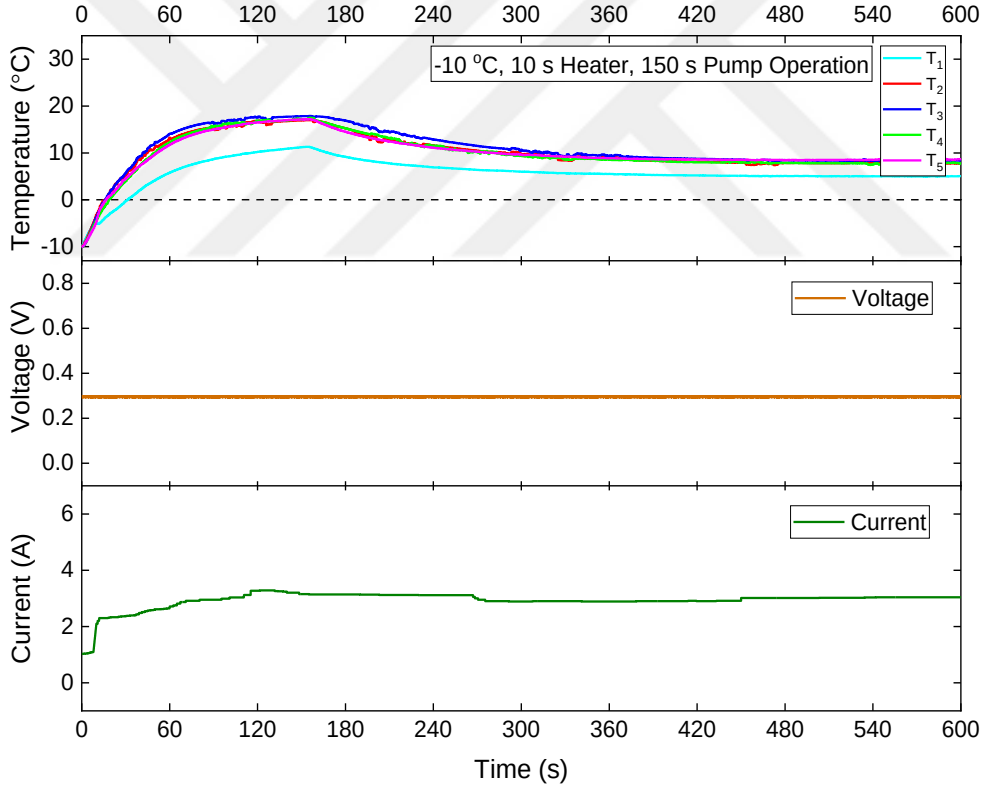

Figure 5.14. Temperature-Voltage-Current vs. Time graphs of the Case #1 (-10 °C)

5.9.2. Case #2 – 15 s Heater, 150 s Pump Operation

The heater was operated for 5 seconds more than Case #1 as a different in this case study. The positive effect of the heater operation duration is reflected in the temperature and current magnitudes. The cell reached zero within 18 seconds and a maximum 21 °C temperature was experienced as seen in Figure 5.15.

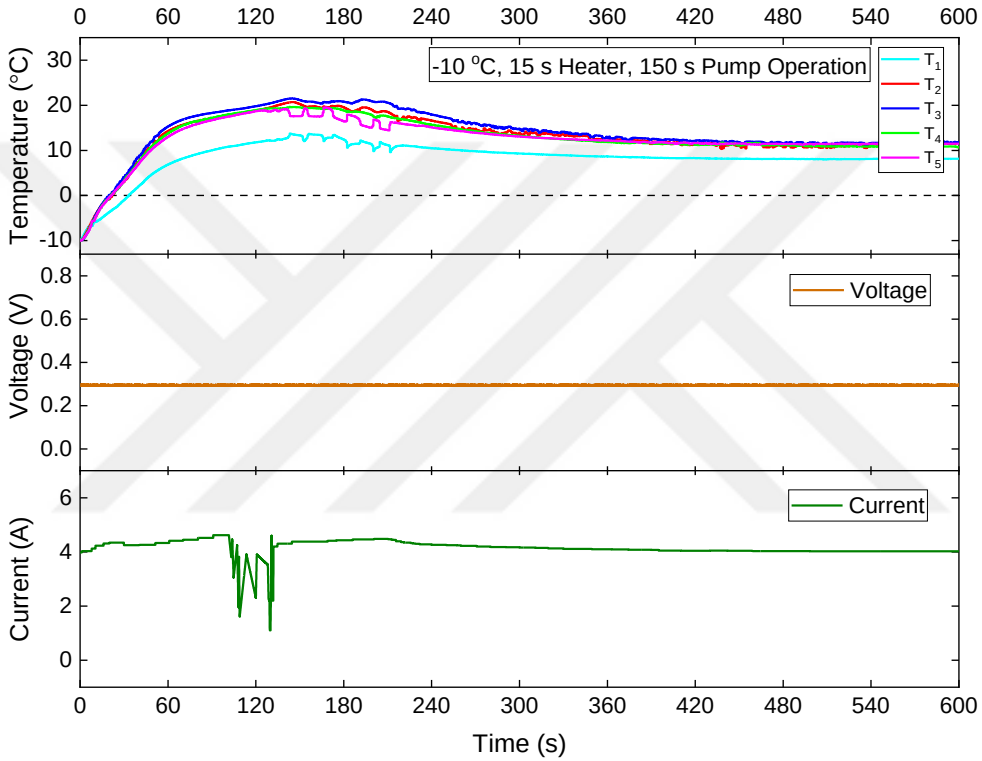

Figure 5.15. Temperature-Voltage-Current vs. Time graphs of Case #2 (-10 °C)

The current protected its situation at 4 A levels even though it fluctuates between 100-132 seconds. The cell temperature was measured at an average of 11-12 °C after the pump was shutdown and the temperature reached a stable position. The positive impact of the heater operation duration increase is exposed in this case study.

5.9.3. Case #3 – 20 s Heater, 150 s Pump Operation

The heater operated for 20 s and the ethanol was circulated for 150 s in this case study. As given in Figure 5.16, the cell generated current and the current increased fractionally and reached 4 A levels.

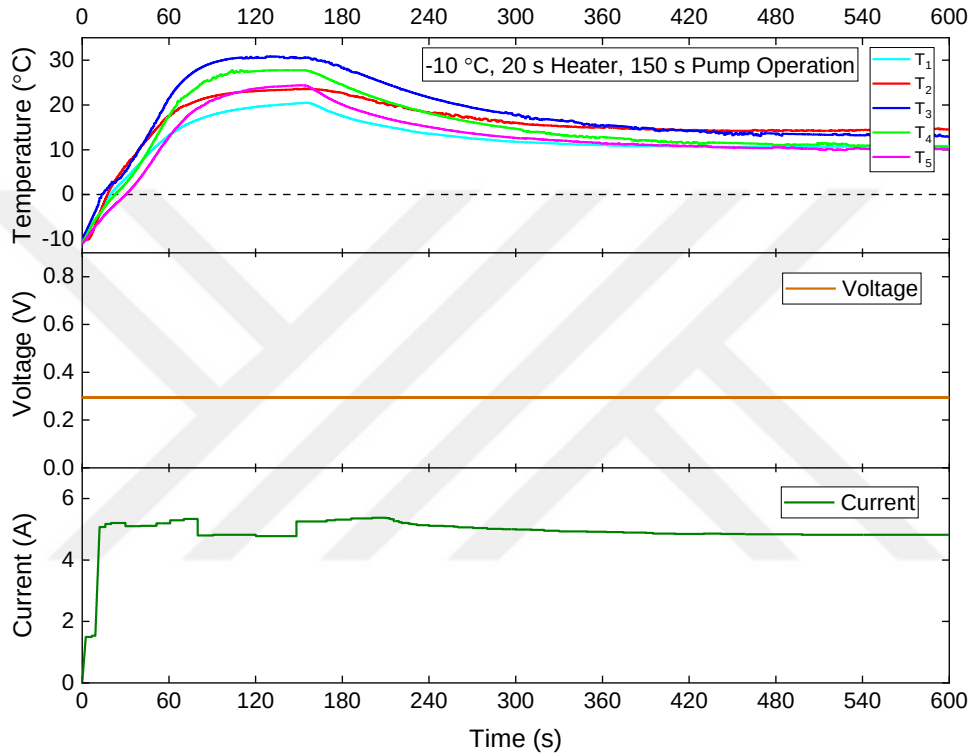

Figure 5.16. Temperature-Voltage-Current vs. Time graphs of Case #3 (-10 °C)

The temperature reached above zero within 15 seconds (at mid-sections of the cell) and increased to 30 °C levels. After the pump was shutdown, the temperature gradually decreased and kept its position at 12-13 °C around. The warmer temperature profile was achieved by a long heater operation duration, as expected. And, the highest temperature difference was experienced in this case study considering the pump shutdown and the temperature stabilization range. Another affirmative feature of this case study is the climbing tendency of the current. The current slightly increased after the temperature stabilization was supplied in the cell.

This tendency provided promising insight into the temperature and current profile in the continuation of the test.

5.9.4. Case #4 – 15 s Heater, 262.5 s Pump Operation

The last case study was performed to manifest the advantage of heater operation or pump operation, experimentally. The pump power is 80 W and the heater power is 1800 W. Therefore, 1 s operation of the heater corresponds to 22.5 s operation of the pump in terms of energy consumption. Temperature-voltage-current following the test is demonstrated in Figure 5.17. The temperature increased to zero within 16 s and climbed to 22 °C at maximum until the pump was shutdown. The temperature slightly decreased after the shutdown and completed the test at 12-13 °C levels. A similar temperature profile was obtained compared to Case #3, especially at the end of the test. The cell reached peak temperature in Case #3, whereas a more homogeneous temperature distribution was obtained in Case# 4. In the meantime, the cell generated a 4 A current for both cases. Therefore, a significant performance difference was not observed when comparing Cases #3 and #4.

In a conclusion, the cell was operated in all cases successfully. The cell temperature increased above zero between 15-20 seconds and the voltage drop was not experienced in all cases. The longer the heater operation, the higher rate of heat transfer and the warmer the temperature profile. However, the longer heater operation consumes higher energy. Therefore, the longer heater operation is redundant at -10 °C temperature. The pre-test results of this section were published in a conference paper (Topcu et al., 2021a).

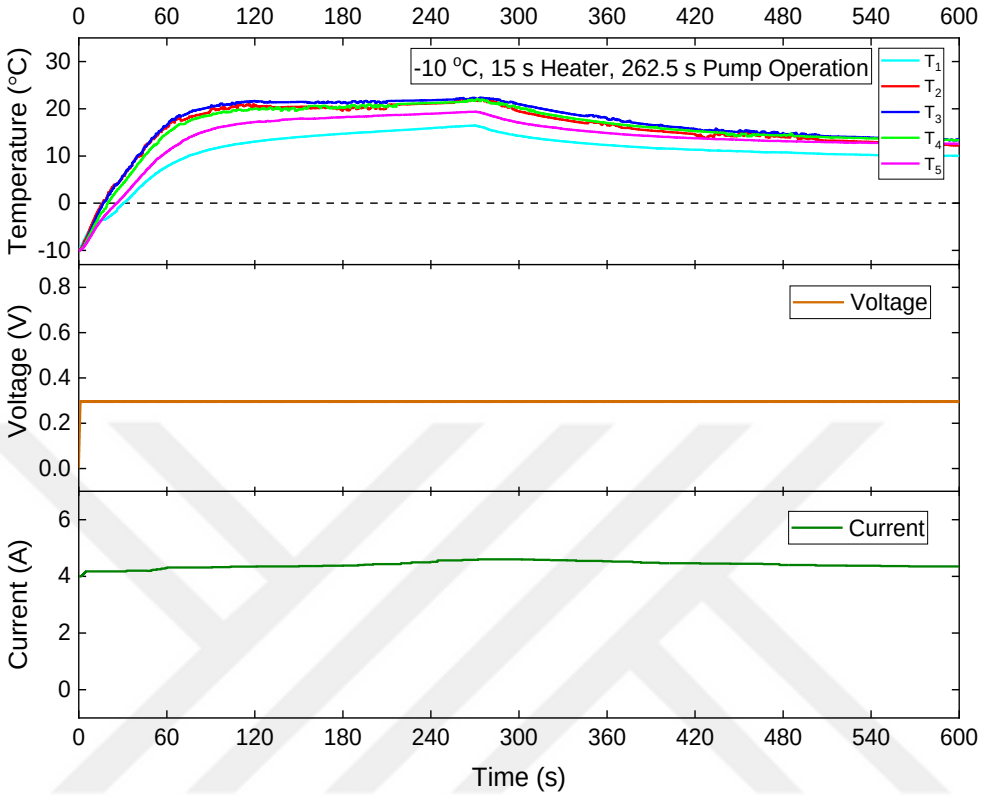

Figure 5.17. Temperature-Voltage-Current vs. Time graphs of Case #4 (-10 °C)

5.10. Case Studies at -15 °C

The proposed assisted heating method ensured successful cold start operations at -10 °C as presented in the previous section. Therefore, the established system was subjected to extreme conditions below -10 °C. Herein, the effect of two significant parameters which are the most energy-consuming components was revealed: the heater and the pump comparison. The test results of this section were published in a SCI-indexed journal (Topcu et al., 2022).

5.10.1. Case #1- 20 s Heater, 150 s Pump Operation

Temperature distribution, voltage, and current following graphs were depicted in Figure 5.18. The temperature was raised to zero within 26 seconds and reached 15.7 °C at maximum temperature. After the peak point, the temperature

gradually decreased and maintained its position at 5-6 °C levels. The cell produced electricity throughout the test and the current improved for 300 seconds. A maximum of 6.68 A current was achieved and the current completed the test above 6 A.

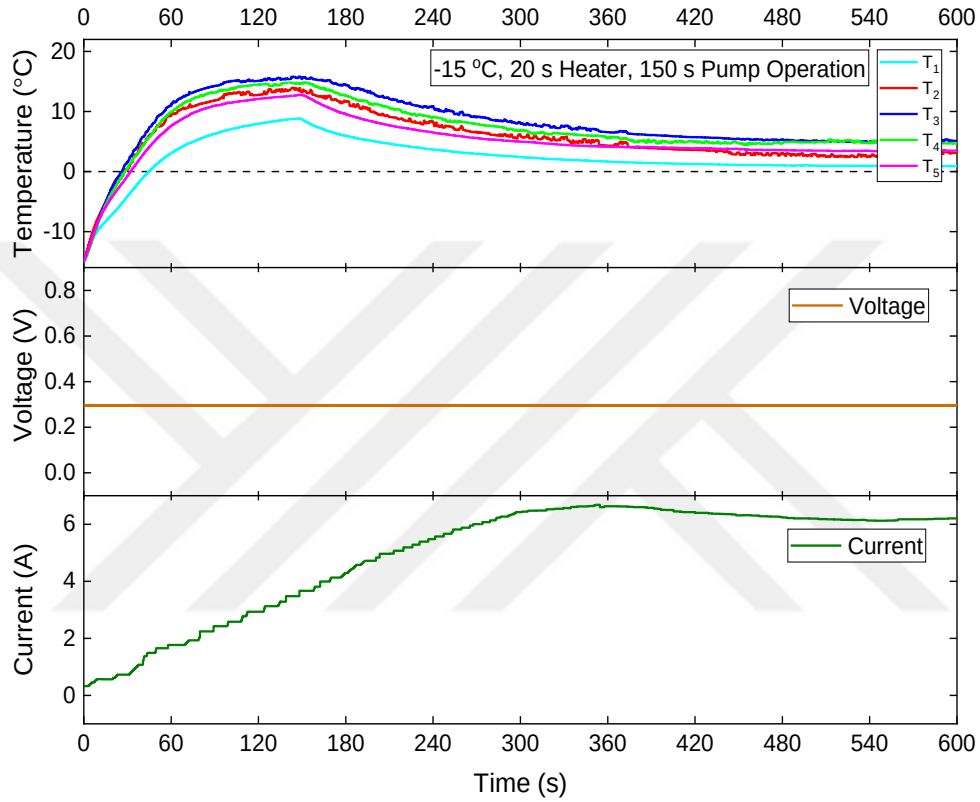

Figure 5.18. Temperature-Voltage-Current vs. Time graphs of Case #1 (-15 °C)

5.10.2. Case #2 – 15 s Heater, 262.5 s Pump Operation

Similar current and temperature profiles were achieved in Case #2 when compared to Case #1 at -15 °C. Current ramped to 6.66 A within 143 s and maintained its position at 6.2 levels towards to end of the test (Figure 5.19). A more stable temperature profile was achieved according to the previous case, and 18.5 °C of maximum temperature was reached at the mid-section of the stack.

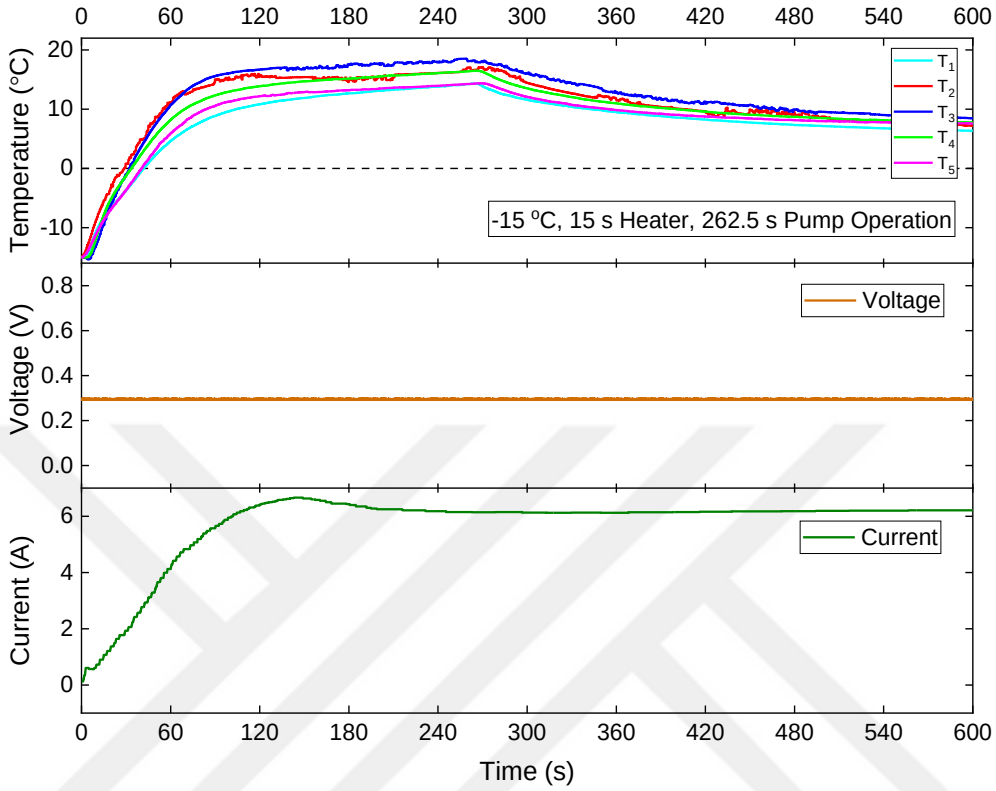

Figure 5.19. Temperature-Voltage-Current vs. Time graphs of Case #2 (-15 °C)

The temperature climbed during the pump operation and gradually decreased after the shutdown. The test was completed at 7-8 °C levels. This case can be highlighted compared to the previous one owing to the homogeneous and relatively higher temperature profile. At this point, a visualization study was performed to enable an understanding of the difference between the temperature profiles of the case studies. An image is provided in Figure 5.20 to show the get the image using the MATLAB code. The experimentally obtained temperature data of each test is transferred to the Excel spreadsheet software, separately. Then, the Excel worksheet is imported using the MATLAB code, and the images were obtained for each second of the test. That means the visualization process may be provided for each second. However, the images were recorded and compared every 100 seconds toward to end of the test.

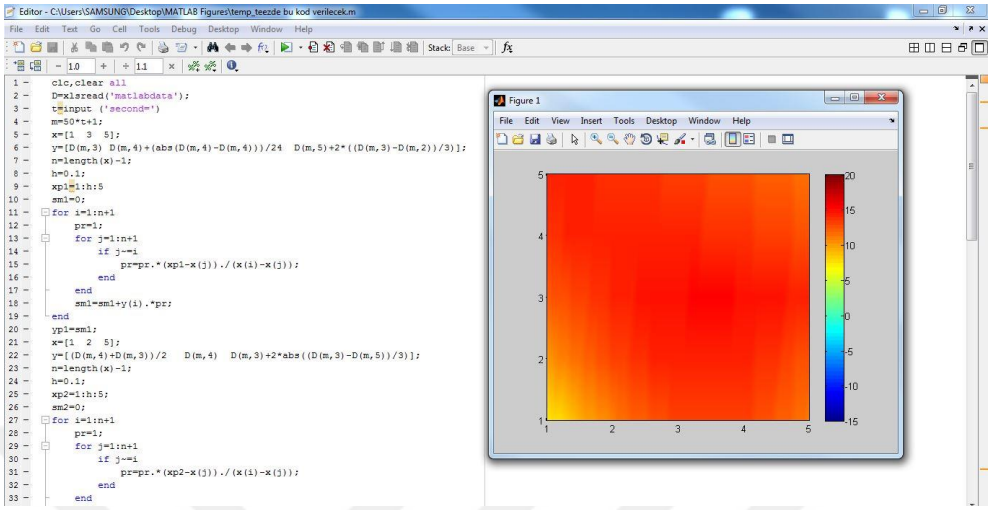

Figure 5.20. MATLAB code and visualization process using the experimental data

The temperature profile comparison of the Case #1 and Case #2 is presented in Figure 5.21 with images taken every 100 seconds. The colour bar was set to the lowest operating temperature (-15 ℃) and 20 ℃ as the highest temperature. The blue colour denotes the cold region, and the red colour indicates the hot region, as understood from the figure. The colormap is blue at the initial stage of the test, naturally. Then, it turned red during the warm-up process and the temperature decreased again after the pump was shutdown. The temperature difference between the case studies is revealed thanks to the providing colormap image, clearly. Quick warm-up and quick temperature decrease were experienced with the long heater operation and short pump operation (Case #1). On the other hand, the temperature was maintained at higher temperatures in Case #2 than in Case #1. The image at 300 s of the Case #1 is very similar to the image at 600 s of Case #2. It is proven the importance of long pump operations to obtain a more homogeneous temperature distribution. In addition, it is seen in the figure that the mid-sections are warmer than the sides. The bottom sides got colder early than the middle and top sides, especially. Of course, the contribution of the electrochemical reactions at the mid-region should not be forgotten.

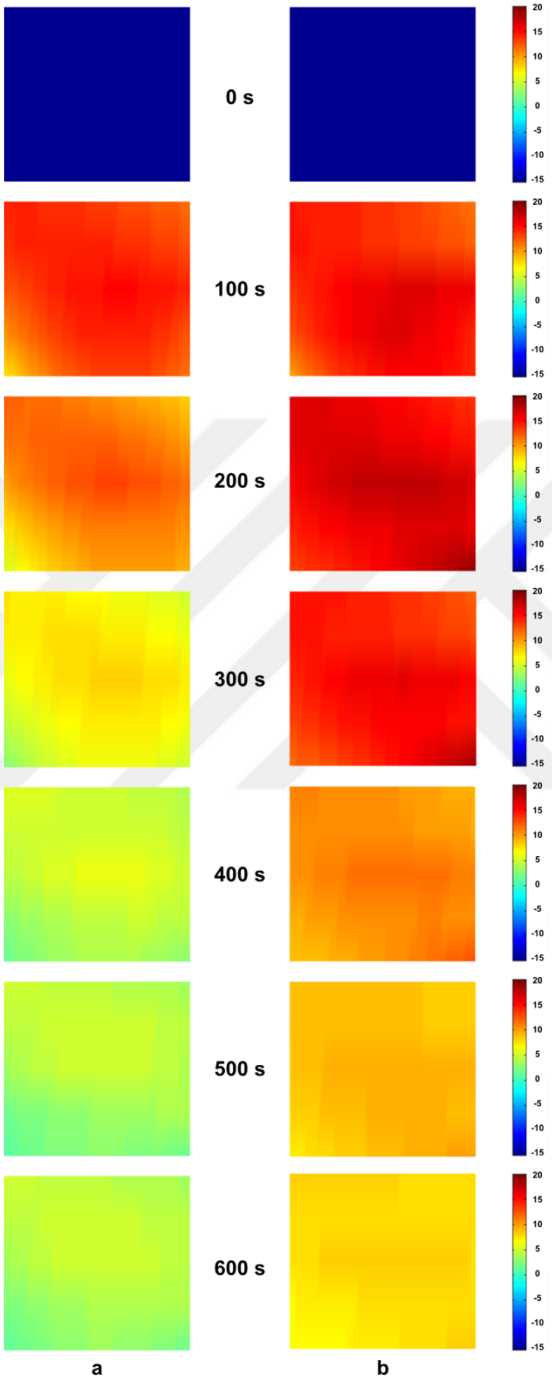

Figure 5.21. Temperature visualization of the case studies at -15 °C operation; a) Case #1, b) Case #2

5.11. Case Studies at -20 °C

5.11.1. Case #1 – 20 s Heater, 150 s Pump Operation

Temperature-voltage-current vs. time graph of Case#1 at -20 °C was illustrated in Figure 5.22. With the decrease in cold start temperature, the achieved maximum temperature level decreases.

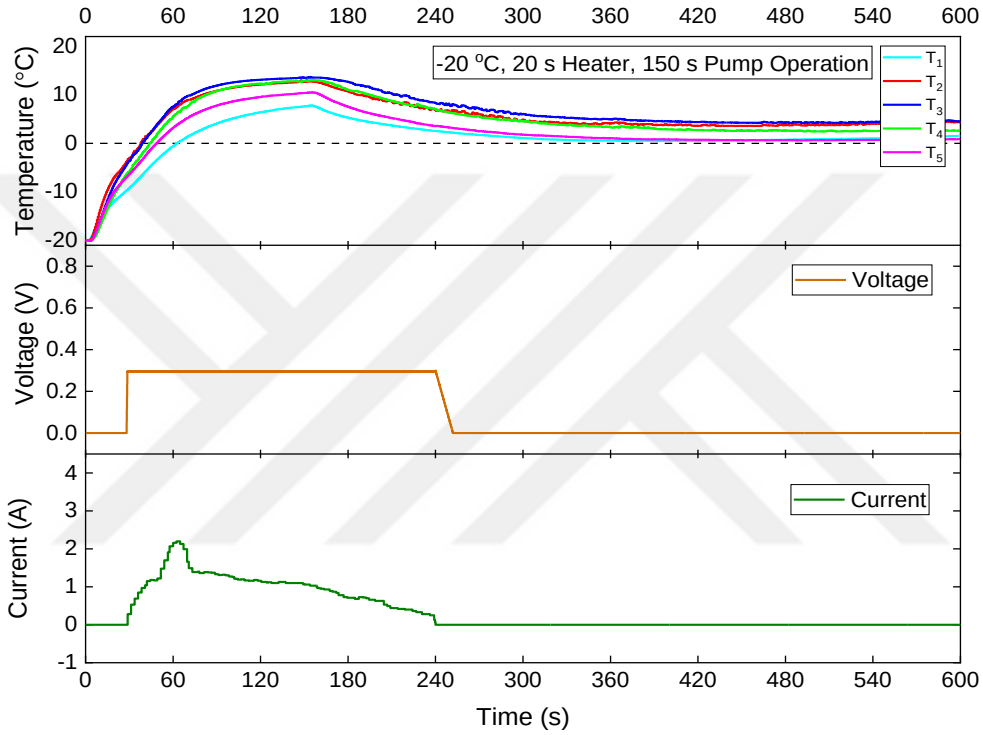

Figure 5.22. Temperature-Voltage-Current vs. Time graphs of Case #1 (-20 °C)

The cell did not generate current at the initial stage of the test as seen in the figure. The cell produced electricity after 28 s, and the current increased to 2.2 A levels. However, the cell did not maintain its position stable, and the current decreased continuously. Finally current and voltage reached zero at 240 s and then did not increase again. The cell temperature increased with the pump operation and decreased after the shutdown. The effect of heat supply by the cell on the overall stack temperature is limited due to the low chemical reactions. Therefore, this case

failed. At this point, it is thought that the instant decrease in temperature after the pump shutdown led to instability in the voltage and current of the cell.

5.11.2. Case #2 – 15 s Heater, 262.5 s Pump Operation

In the second case, the heater duration decreased, and the pump duration increased as in previous comparisons. A successful cold start was ensured, and the cell generated current throughout the test.

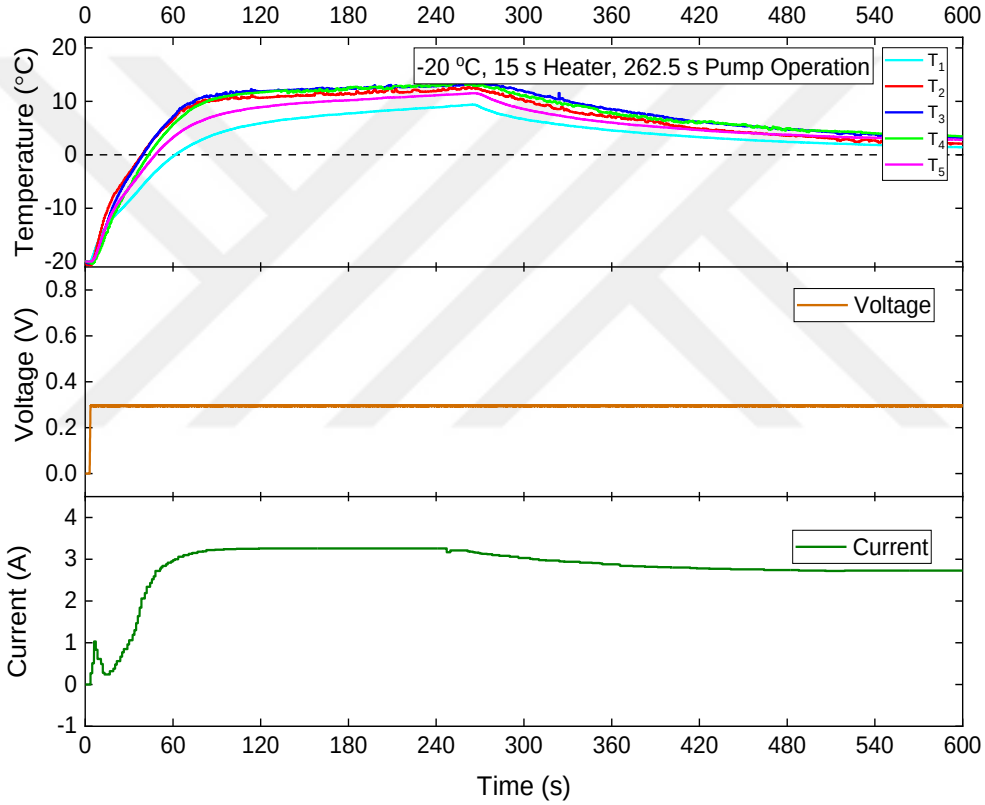

Figure 5.23. Temperature-Voltage-Current vs. Time graphs of Case #2 (-20 °C)

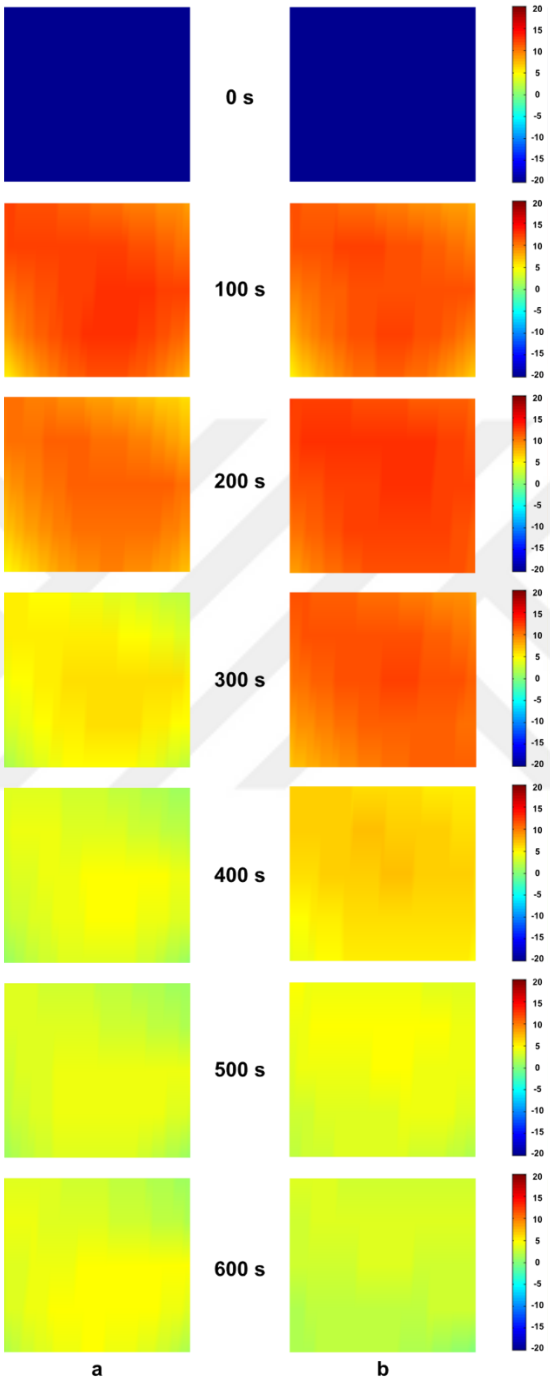

Figure 5.24. Temperature visualization of the case studies at -20 °C operation; a) Case #1, b) Case #2

A maximum of 3.26 A current was achieved and the test was completed with 2.73 A levels (Figure 5.23). The cell temperature reached zero within 39 seconds. The required time to achieve zero is increased with a decrease in cold start temperature, as experienced. The temperature level of the mid-section of the cell (T_2-T_3-T_4) is higher than the sides (T_1-T_5). A maximum 13.3 °C temperature was achieved, and the test was completed at 3 °C levels.

The temperature profile comparison of the case studies at -20 °C is depicted by the visualized image in Figure 5.24. The colour bar was scaled in the range of -20 and 20 °C. A colder temperature profile was experienced when compared to the previous (-15 °C operation) section. The reason for this is the decreased cold start temperature, of course. It should be considered that the colour bar can be updated according to the direction of the user. The effect of the long pump operation was sensed in Case #2 during the first 300 seconds. Then, the temperature decreased rapidly, and similar temperature profiles were achieved for both cases at the end of the test. It is seen that the temperature is around zero toward the end of the test. In addition, it is seen apparently from the colormap that the heater was not warmed the coolant at the level of previous section.

5.12. Case Studies at -25 °C

5.12.1. Case #1 – 20 s Heater, 150 s Pump Operation

The cell warm-up profile and current following were presented in Figure 5.25. The current increased to 8.81 A at maximum and maintained its position at 7.5 ~ 8 A levels until 480 seconds. After this threshold, the current and voltage decreased to zero instantly, and the cell did not generate electricity for the rest of the test. The stack temperature at the mid-section increased above zero within 44.5 seconds, and the other locations arrived above zero later. The temperature reached 10.7 °C at maximum and then gradually decreased.

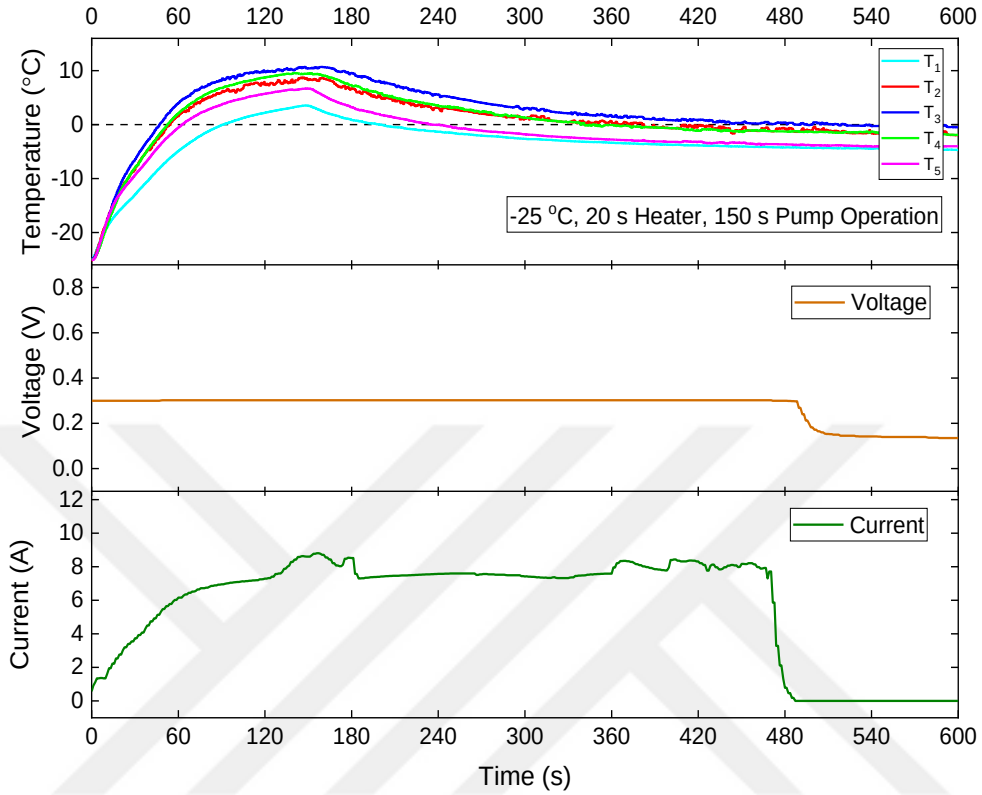

Figure 5.25. Temperature-Voltage-Current vs. Time graphs of Case #1 (-25 °C)

Although the heater was operated for 20 seconds and the cell temperature increased above zero completely, the lower and the upper side temperatures decreased below zero after 199 and 235 seconds, respectively. Similarly, the mid-section temperatures dropped below zero later in the test. Although the cold start test began and was maintained successfully, the case study failed toward the end of the test.

5.12.2. Case #2 – 15 s Heater, 262.5 s Pump Operation

A successful cold start was achieved in this case study. The cell generated current throughout the test as seen in Figure 5.26. The current increased to 11.5 A at maximum and after a threshold, it decreased gradually. This current value is the highest magnitude among all case studies. Undoubtedly, the higher the current

values, the higher the heat generation. The maximum stack temperature reached 10.4 °C with the combined effect of the heat generated by the cell and heat supplied by the external loop. The effect of the higher pump operation played an important role in reaching this temperature.

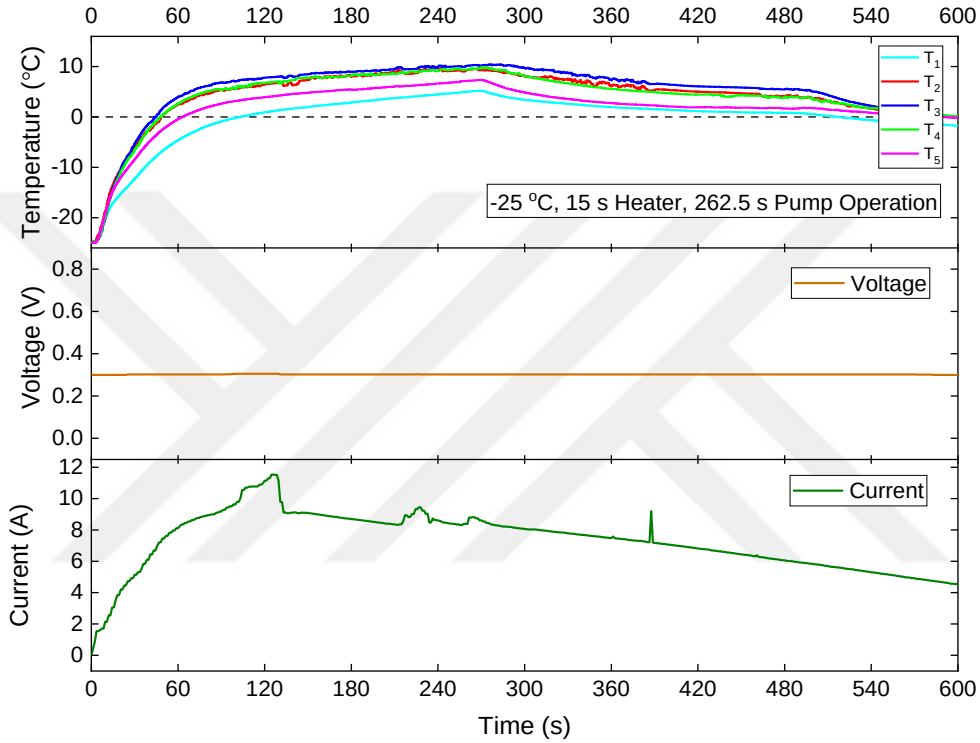

Figure 5.26. Temperature-Voltage-Current vs. Time graphs of Case #2 (-25 °C)

However, the temperature decreased and dropped below zero after the pump shutdown. It is obvious that this case study is more promising than the previous one. Nevertheless, it is clear that the test is unsustainable, too. Although the stack temperature decreased below zero, the cell generated current successfully throughout the test. But, the downward tendency in the current level provides negative estimates on the continuation of the test (after 600 s).

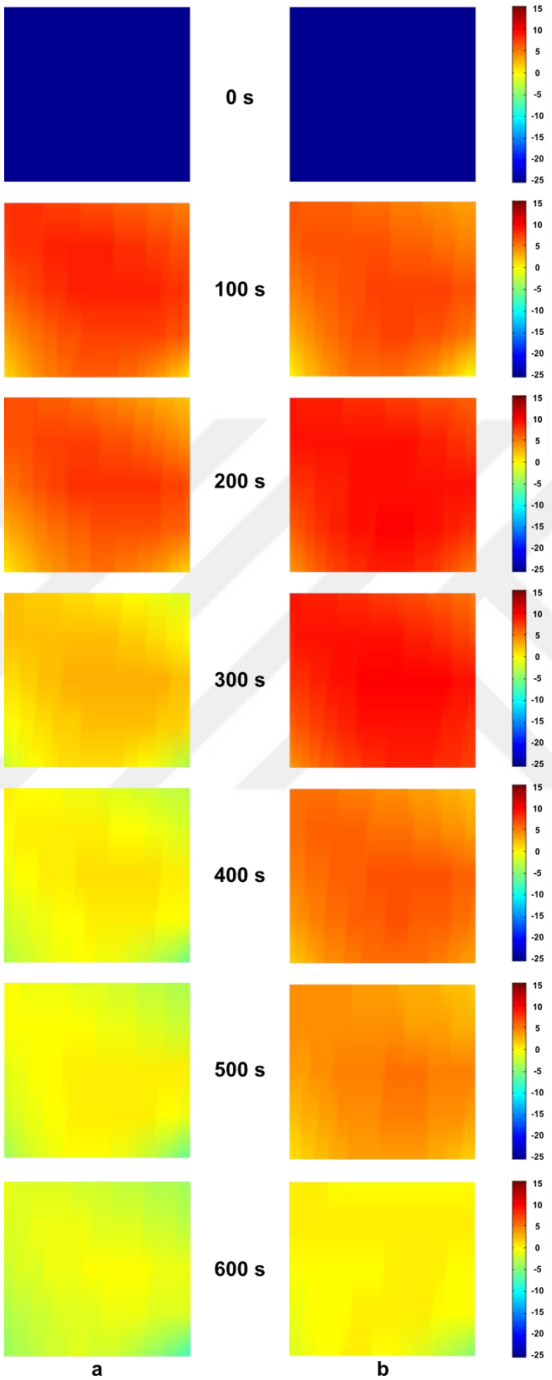

Figure 5.27. Temperature visualization of the case studies at -25 °C operation; a) Case #1, b) Case #2

The current and voltage values will be reached zero because the novel water particles will be frozen. A second sharp decrease in temperature was experienced at ~500 seconds as seen in Figure 5.26. This tendency proves the explanations above.

The temperature profile comparison of the case studies at -25 °C is illustrated by the performed image visualization study in Figure 5.27. The colour bar was scaled in the range of -25 and 15 °C. Therefore, the total temperature difference (40 °C) was kept constant as in the previous section (-20 °C). Indeed, a similar temperature profile was experienced when compared to the previous (-20 °C operation) section. The reason for this is the constant colour bar scale. If the highest point of the colour bar could be set to 20 °C, it would be seen the colder temperature profile.

A warmer temperature profile was obtained with the long pump operation (Case #2), as expected. Yellow and green colours indicated zero points and below as a different from the previous sections. It is seen from the colour map that the temperature is around or below zero in both cases at the end of the test. It can be referred from the temperature profile that the temperature tendency goes below zero continuously. Even if the cell generated electricity during the test (for 600 seconds), with the continuation of the test (after 600 seconds) it will decrease and reach zero, probably. For this reason, an extra operation of the heater or pump may be required to inhibit a performance output loss.

5.13. Case Studies at -30 °C

20 s heater – 150 s pump operation vs. 15 s heater – 262.5 s pump operation cases were compared in the previous sections. Successful cold start operations were achieved thanks to this employment. Heater and pump durations were found adequate for warmer cold start temperatures (-10, -15 °C). With the decreasing cold start temperature, the cell struggled to keep its temperature above zero. Further, the cell temperature dropped again below zero with -25 °C operations. Although the cell produced electricity, it is predicted the run out with the continuation of the test. Since

a similar challenge will be observed at -30 °C operation, the heater and the pump operation durations were extended. The lowest cold start temperature was assigned as -30 °C, in this study. An initial test was conducted to see the effectiveness and sufficiency of the heater and the pump. Then, case studies were performed under the same energy consumption level.

5.13.1. Initial Test – 30 s Heater, 210 s Pump Operation

The voltage, current, and temperature following of the initial test with 30 s heater and 210 s pump operation at -30 °C were demonstrated in Figure 5.28.

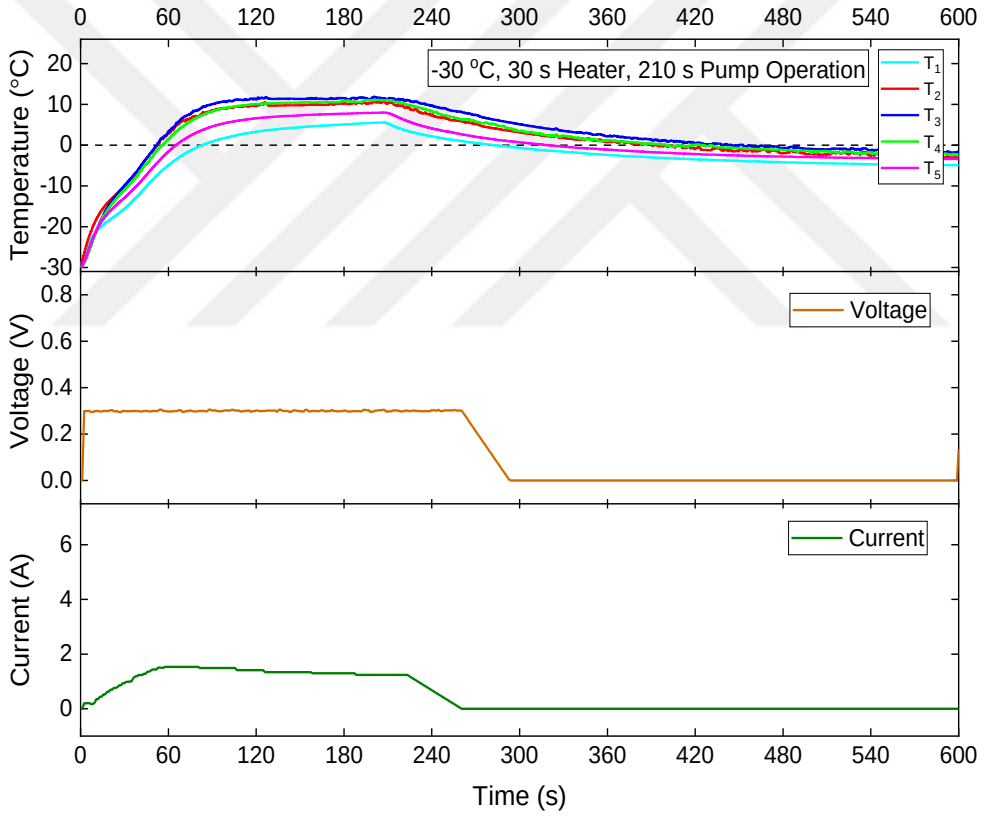

Figure 5.28. Temperature-Voltage-Current vs. Time graphs of the initial test (-30 °C)

At the initial stage, the current raised to 1.53 A maximum level. The current was maintained at mentioned levels between 54-223 seconds, and then gradually

decreased and dropped to zero after 260 seconds. The voltage, on the other hand, dropped gradually to zero with the decrease of the current to zero. The voltage and the current never increased again during the rest of the test. The temperature at the mid-section of the stack increased above zero after 54 seconds from the start. The upper and the lower side temperatures raised to zero after 65 and 83 seconds, respectively. The cell temperature was kept stable between 75-240 seconds at 10-11 °C levels with the effect of pump operation and heat generation in the cell. After the pump shutdown, the produced heat by the cell did not sufficient to keep the stack above zero. Firstly, the temperatures at the sides of the cell dropped below zero, and then mid-sections, too. It is understood that the heater and the pump operation durations are still inadequate to achieve a successful cold start at -30 °C.

5.13.2. Case #1 – 50 s Heater, 200 s Pump Operation

After the failed start operation in the initial test with 30 s heater operation, the heater operation duration was increased to 50 seconds. The temperature profile is presented in Figure 5.29 and the effect of the long heater duration is seen clearly. The cell generated current throughout the test and the current was maintained at ~2.6 A levels. The temperature at the mid-sections of the cell increased above zero within 53 seconds.

After the heater shutdown, the temperature increased to 23.7 °C maximum levels, and the stack temperature was kept at these levels until the pump shutdown. Then, the temperature gradually decreased and was close to zero at the end of the test. Achieved high temperature levels helped to keep the stack above zero and produce electricity throughout the test. A highly stable current profile was achieved with this case study. Although the temperature decreased after the pump shutdown, the heat generation in the cell kept to stack temperature above zero. This proved a successful cold start at -30 °C.

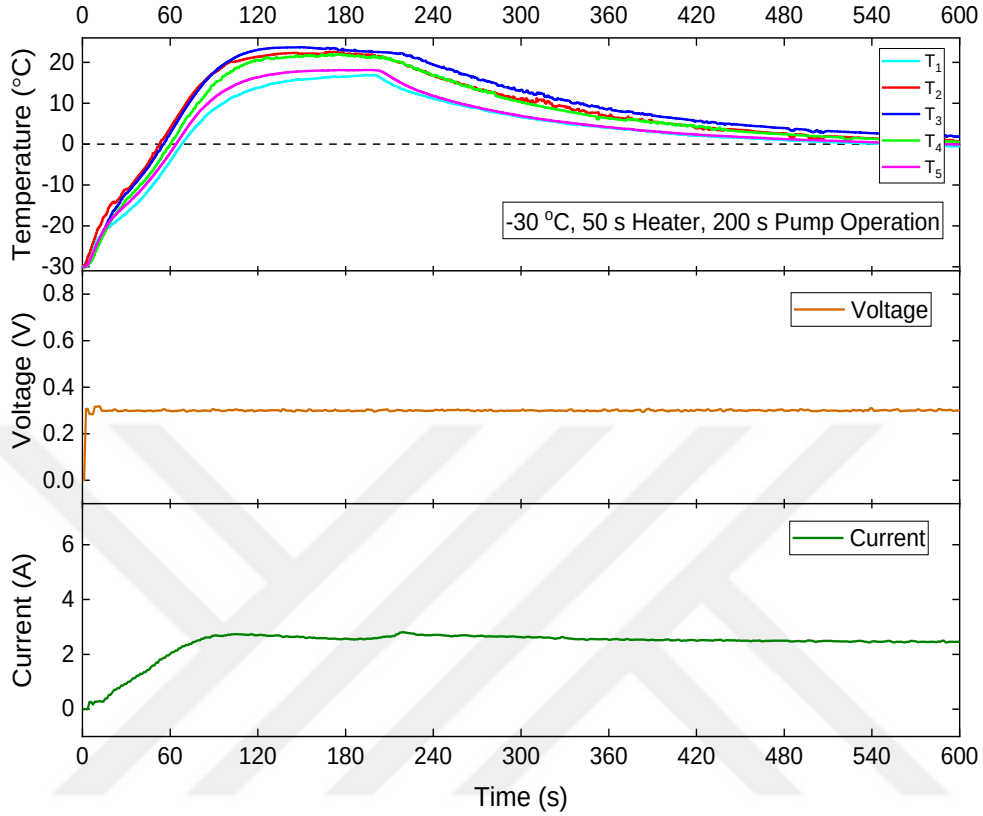

Figure 5.29. Temperature-Voltage-Current vs. Time graphs of Case #1 (-30 °C)

5.13.3. Case #2 – 45 s Heater, 312.5 s Pump Operation

The last case study of this research is completed with the 45 s heater and 312.5 s pump operation case. The current, voltage, and temperature profile of the case is illustrated in Figure 5.30. Highly stable and homogeneous temperature and current profiles were ensured as seen in the figure. The current climbed to 6.5 A levels and was maintained at 5.5 A levels towards the end of the test. The temperature reached above zero within 53 seconds at the mid-section of the cell. The upper and the lower side temperatures raised to zero after 61 and 70 seconds, respectively. The cell temperature was kept stable between 100-350 seconds at 18-19 °C levels with the effect of pump operation and heat generation in the cell. After the pump

shutdown, the temperature slowly decreased, and the temperature was at 5-6 °C levels at the end of the test.

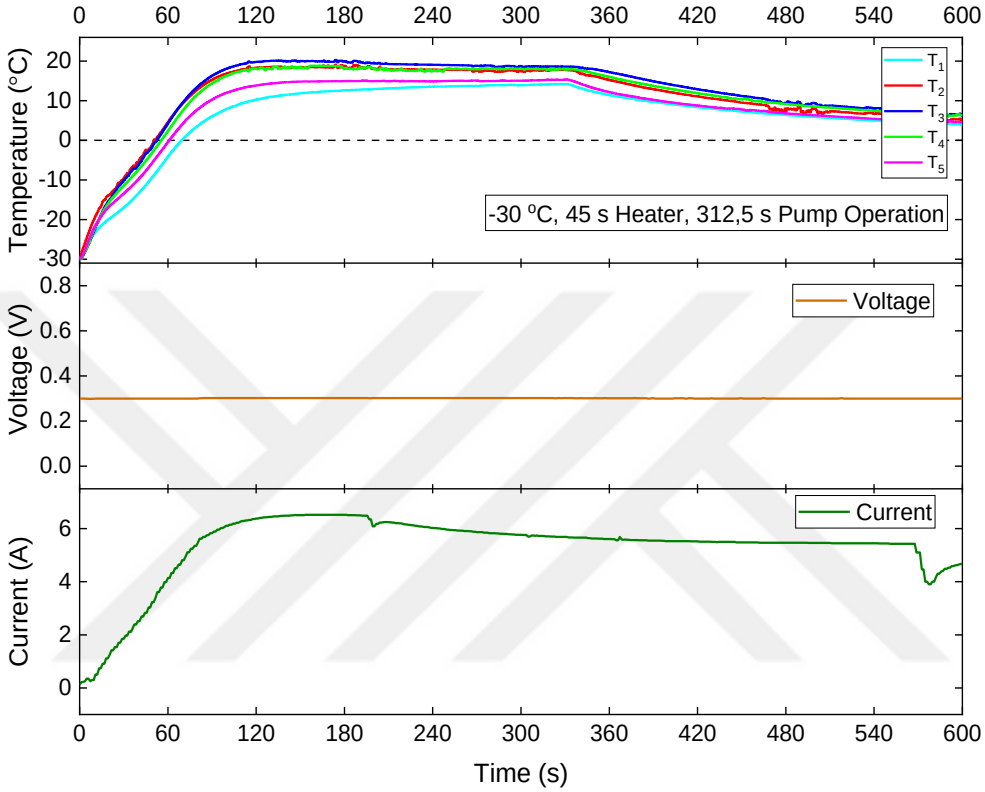

Figure 5.30. Temperature-Voltage-Current vs. Time graphs of Case #2 (-30 °C)

It is proved a successful operation at -30 °C and is better than the previous one. A cold start with a long pump operation was found more successful rather than a long heater operation duration. Although instant heating and high temperature levels were supplied with long heater durations, it is understood that the instant temperature decreases after long heater operation and low pump operation cases dragged to cell instability. These unstable circumstances lead to a drop in voltage and current of the cell usually.

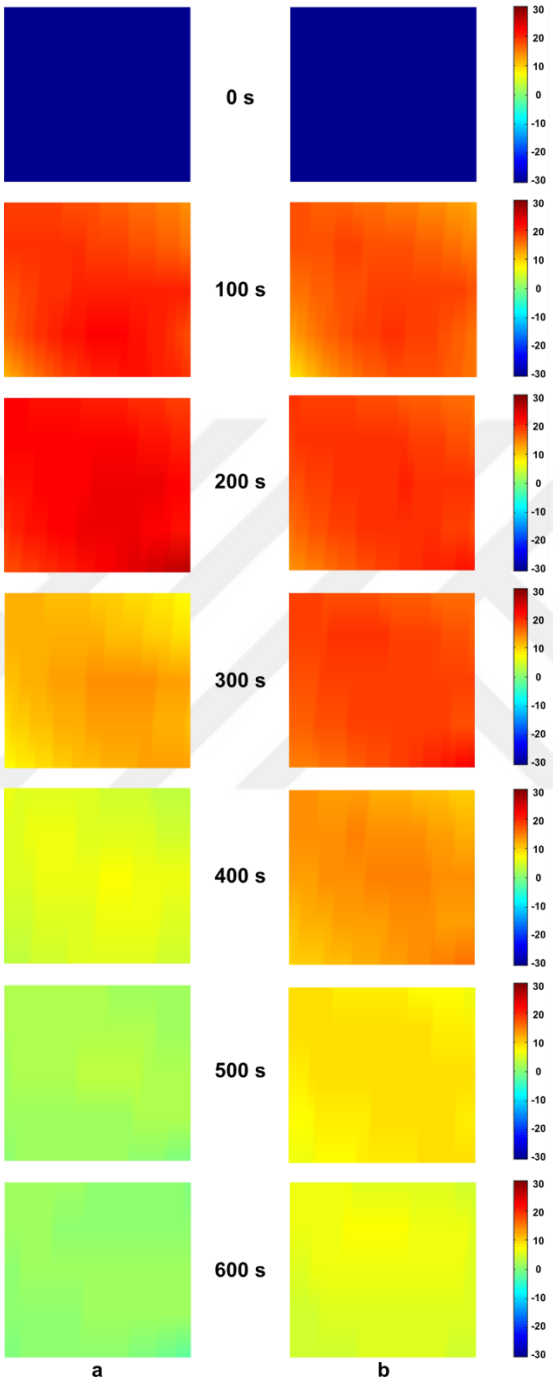

Figure 5.31. Temperature visualization of the case studies at -30 °C operation; a) Case #1, b) Case #2

The temperature profile comparison of the case studies at -30 °C is presented by the performed image visualization study in Figure 5.31. The colour bar was scaled in the range of -30 and 30 °C. Therefore, the highest temperature range was ensured with the -30 °C cold start operation. A warmer temperature profile was obtained with the long pump operation (Case #2). It is shown that the temperature was about 10 °C in Case #2 while it was zero levels in Case #1. Although the temperature was raised above 20 °C for both cases, it can be referred from the temperature profile that the temperature tendency goes below zero. Extra operation duration of the heater and pump is useful to keep the stack above zero.

It should be considered that the energy consumption level increased to heat the stack for lower cold start temperatures like -30 °C. It is obvious that much energy needs to heat and keep the stack above zero. DOE aimed for a successful cold start within 30 seconds from -20 °C and a maximum of 5 MJ energy consumption (Website, 2021). Therefore, more energy can be consumed than 5 MJ for operations at below -20 °C. Obtained all experimental data is presented in Table 5.5.

In most cases, the mid-section temperatures were found higher than the sides after the temperature stability. Occurred exothermic reactions and the direction of the heat transfer triggered this raise. The stack was placed into the environmental chamber vertically and the temperature was followed symmetrically starting from the lower side to the upper side of the cell as seen in Figure 3.16. The lower measurement point (T_1) temperature decreases when compared to the upper measurement point (T_5) after a time test began. Since the direction of heat transfer is upwards, the supplied heat by the cell and external cycle flows upward. Therefore, T_2, T_3, T_4, and T_5 temperatures are relatively higher in comparison to T_1. A similar circumstance was recorded by Zhan et al. (2018) and the coolant outlet temperature was warmer than the inlet one in the case of heating end plates by air.

Table 5.5. Temperature and current data of the case studies

Test Temp. (ºC)	Heater Duration (s)	Pump Duration (s)	Fail/ Successful	Time to Achieve Zero (ºC)	Reached Max. Temp. (ºC)	Cell Temp. at Test End (mid-point, ºC)	Max. Current (A)	Current at Test End (A)
-10 (self-oper.)	-	-	Fail	-	-7.5	-8	1.64	-
-10	10	150	Successful	18	18	8.4	3.3	3
-10	15	150	Successful	18	21.3	11.9	4.5	4
-10	20	150	Successful	14.5	30.7	13	4	3.4
-10	15	262.5	Successful	16.4	22.3	13.5	4.6	4.4
-15	20	150	Successful	26.3	15.7	5.1	6.7	6.2
-15	15	262.5	Successful	32	18.5	8.5	6.7	6.2
-20	20	150	Fail	38.5	13.7	4.5	2.2	-
-20	15	262.5	Successful	39.2	13.2	3.2	3.3	2.7
-25	20	150	Fail	44.5	10.7	-0.5	8.8	-
-25	15	262.5	Successful	44.9	10.4	0	11.5	4.5
-30	50	200	Successful	53	23.7	1.8	2.8	2.5
-30	45	312.5	Successful	53	20.2	6.2	6.5	4.7

5.14. EIS Measurements

EIS measurement results of the initial (even after the activation of the MEA), after the 10th, 20th, and 30th cold start tests are illustrated in Figures 5.32, 5.33, 5.34, and 5.35, respectively. The coolant heating method is not detrimental effect on the MEA aforementioned. Nevertheless, freeze/thaw cycles bring about a degradation with time. As seen in all EIS measurement figures, the cell maintained its position after cold start cycles with low resistance characteristics. It is proved that the preferred heating mechanism is reliable and has no significant negative effect on MEA degradation. However, low resistance increases were experienced with the increase of the cold start cycle.

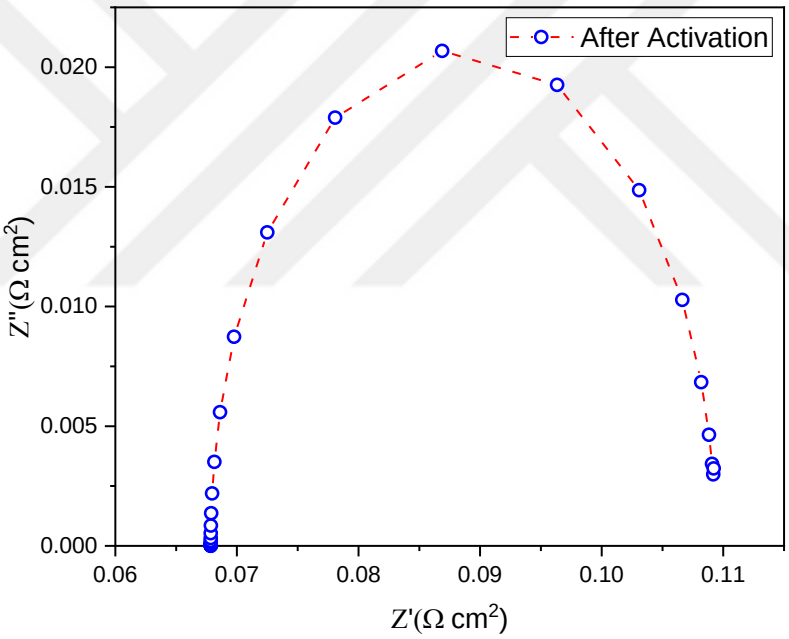

Figure 5.32. EIS measurement of the MEA even after the activation process

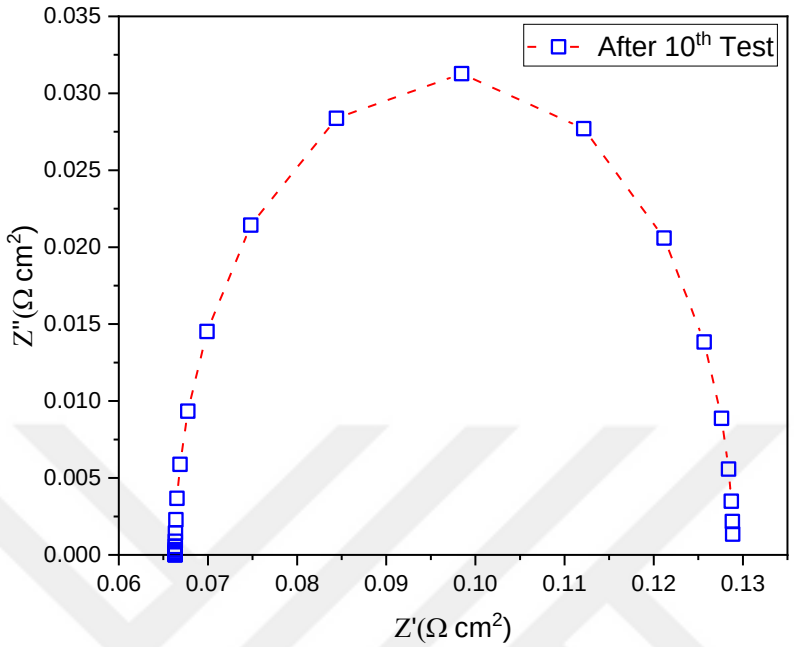

Figure 5.33. EIS measurement of the MEA after 10 cold start tests

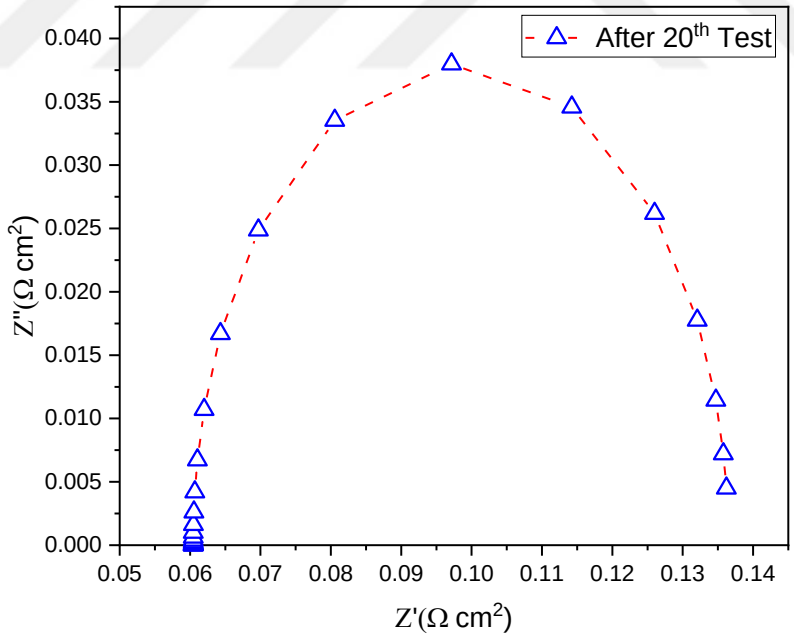

Figure 5.34. EIS measurement of the MEA after 20 cold start tests

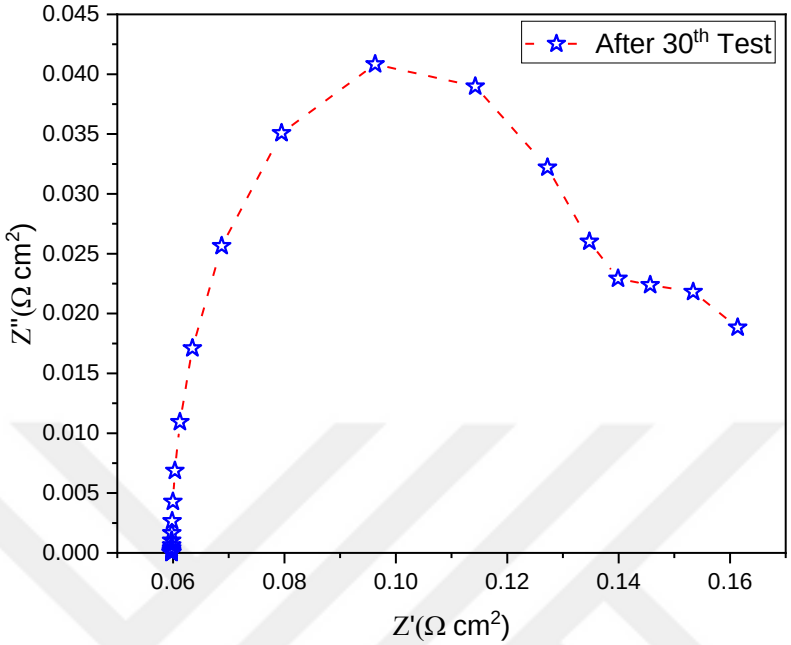

Figure 5.35. EIS measurement of the MEA after 30 cold start tests

In the experimental section of another research, the outlet temperature of the coolant outdistanced the inlet temperature even after the start of the test (Wei et al., 2019). The dry cell should be used to achieve a successful cold start at the beginning of the operation. This is proved by the author, and it is noted that the existing ice accumulates blocked gas distribution throughout the cell when the cold start began. Nevertheless, the H_2 gas may be delivered to the anode side if not close to the entire region of the anode completely. In this case, novel water droplets turn into ice structures and blockage the gas transmission ways. It is demonstrated with voltage drop or operating of back pressure on the fuel cell test station. However, all these challenges were eliminated by using a dry membrane for each case study. Otherwise, it leads to cold start failure in some cases. The occurred ice accumulates after some cold start tests are shown in Figure 5.36. It is obvious that the droplets inhibit the gas transfer to the AA by covering the flow channels as well as the MEA surface.

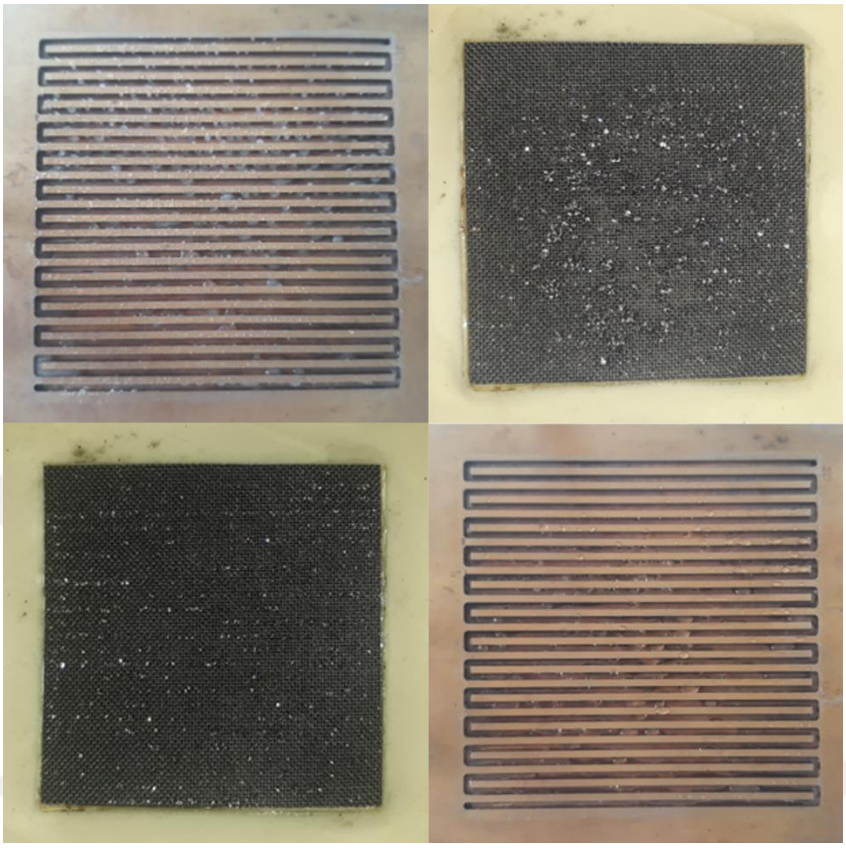

Figure 5.36. Occurred ice accumulates after the cold start tests

The existence of ice accumulations proves the cell temperature decreased below zero even though the cell was operated successfully. In addition, the cell performance will be influenced negatively due to the blocked catalyst surface and flow channels by ice. It can be referred easily that the current generation will be dropped to zero at the continuation of the tests (after 600 s).

The lowest cold start temperatures (-20, -25, and -30 °C) are required extra heating support by the external circuit. Even, the cell temperature increased and decreased again below zero with the classical operating conditions at the initial -30 °C case. It confirmed the requirement for more energy for the stack at the deepest cold start temperatures. Nevertheless, the cell was operated successfully thanks to

the proposed heating mechanism at these temperatures. The detrimental effect of the instant temperature decrease was revealed with -20 and -25 °C operations. It is reported that the rapid temperature fluctuations lead to unstable behavior in the MEA and concentration loss, and therefore cold start failure. On the contrary, a slow and smooth temperature transition is the key to a successful cold start operation. The heater operation is crucial to provide heat fatefully. However, a smooth and homogeneous temperature profile may be achieved by the long pump operation. Even though the powerful features of the coolant-assisted technique were unveiled at the single-cell level in the present study, the method may be implemented at large-scale stacks. Large energy scales can be transferred in this way safely for all stack levels. Inner and outer compartments are operated synchronically but separately in this approach, and it increases the reliability and applicability of the method. Furthermore, the MEA degradation is minimized since the application is not charged to MEA under the thaw/freeze cycles.

5.15. Fluid Flow Analysis

With the connection of the fluid cycle hoses to the inlet points of the stack, the flow rate is decreased due to the pressure drop effect occurring in the flow channels. For instance, the mass flow rate was measured as $\dot{m} = 0.0383333\ kg/s$ before the coolant hoses were not connected to the inlet points of both sides of the stack. This mass flow rate includes the sum of the mass flow rates of both sides and is recorded with the 12V operation of the pump. But, half of the sum $\dot{m} = 0.01916667\ kg/s$ was considered for the analysis since the flow was separated in two ways which are anode and cathode compartments. Thus, only cathode side calculation was conducted because the experimental temperature data is available in this section. The diameter of the connection hoses is $D = 0.04\ m$. Therefore, the average velocity of the ethanol can be calculated using Equation 4.1.

$$\dot{m} = \rho V_{avg} A_c$$

$$\dot{m} = 0.01916667\ kg/s$$

$$\rho = 786.6\ kg/m^3$$

$$A_c = \frac{\pi D^2}{4} = \frac{\pi 0.04^2}{4} = 0.00125664\ m^2$$

$$V_{avg} = 0.01939\ m/s$$

Therefore, V_{avg} is determined as $0.01939\ m/s$ based on the calculation above. It should be noted that the specified mean velocity is idle operation (no-load) of the pump and may be varied throughout the pipe due to the losses in the piping system.

However, this average velocity can not be used for further calculations. The mean velocity should increase after connection since the cross-sectional area narrowed to provide the pressure balance between the inlet and outlet points. Herein, fluid flow analysis was carried out to reveal pump specifications and required pumping power to overcome pressure losses. The pump was operated at 3, 6, 9, and 12 VDC as presented in Section 5.7. As expected, the mass flow rate of the working fluid increases with the increase of the operating voltage of the pump.

The first analysis was conducted with a 12 VDC pump operation. The characteristic length (hydraulic diameter) is the side length of the square duct, $D_h = a = 1\ mm\ (0.001\ m)$. The mass flow rate was measured experimentally and presented in Table 4.2, previously. For the 12 VDC pump operation, the mass flow rate is determined as $\dot{m} = 0.01083333\ kg/s$, experimentally. However, it is the sum of the mass flow rates of the anode and cathode sections. For this reason, it is divided into two and the novel mass flow rate is $\dot{m} = 0.00541667\ kg/s$ for the cathode section only. The same equations were solved for the novel values at the inlet point of the flow channel.

$$\dot{m} = \rho V_{avg} A_c$$

$$\dot{m} = 0.00541667\ kg/s$$

$$\rho = 786.6\ kg/m^3$$

$$A_c = a^2 = 0.001^2 = 1x10^{-6}\ m^2$$

$$V_{avg} = 6.886\ m/s$$

$$\dot{V} = V_{avg} A_c = 6.886x1x10^{-6} = 6.886x10^{-6}\ m^3/s$$

That is the V_{avg} is calculated as $6.886\ m/s$ for the 12 VDC pump operation in the flow channels. In addition, the volume flow rate (Equation 4.11) $\dot{V}$ is determined as $6.886x10^{-6}\ m^3/s$ depends on the cross-sectional duct area.

The Reynolds number can be calculated with the help of Equation 4.2. The kinematic viscosity of the ethanol can be used directly since it is determined in Section 5.2 and presented in Table 5.2 (v =1.207x10^{-6} m^2/s).

$$Re = \frac{V_{avg} D_h}{v} = \frac{6.886\ m/s\ x\ 0.001\ m}{1.207x10^{-6}\ m^2/s} = 5705$$

The Reynolds number is calculated as 5705 for the 12 VDC pump operation in the flow channels. It is obvious that the $Re \gtrsim 4000$ and therefore, the flow in the turbulent region. Therefore, the entrance region may be determined by the turbulent region relations provided in Equation 4.5.

$$\frac{L_{h,turbulent}}{D} \cong 1.359\ Re^{1/4}$$

$$L_{h,turbulent} \cong 1.359\ x\ 5705^{1/4}\ x\ 0.001 = \ 0.0118\ m = 1.18\ cm$$

The entry length is determined as 1.18 cm and the length was found much shorter than the laminar flow section. Therefore, the flow can be considered in the hydrodynamically fully developed region. Herein, it is proved that the flow is steady and incompressible.

In the next step, the pressure drop throughout the channels was determined. Minor and major losses comprise the head loss and can be calculated with the help of Equation 4.8.

$$h_{L,total} = \left(f\frac{L}{D} + \sum K_L\right)\frac{V^2}{2g}$$

Darcy friction factor f is determined depending on the Reynolds number. As seen, the Reynolds number is 5705 and relative roughness (ε/D) is 0.002 due to the characteristic length being $D = 1\,mm.$ The intersection point of the relative roughness and the Reynolds number was calculated from the Moody Chart and the Darcy friction factor is specified as $f = 0.0385$. Herein, an observation error by the user should not be forgotten and the f value can be considered as different from the current value with small changes.

The other loss coefficient (for minor losses) is the loss coefficient, K_L, is assumed as 1.1 for the 90º miter bend. Flow channels include 48 turns with 90º miter bend and 2 turns with 90º miter bend at the inlet and outlet points. Therefore, 50 turns with 90º miter bend ($K_L = 1.1$) is considered throughout the active area in the minor losses calculations. $L\ (m)$ denotes the total length of the channel. A channel length is 50 mm and there are 25 channels in the flow area. In addition, there is a 1 mm space after each 90º miter bend (24 spaces in total). Consequently, a 1.274 m total channel length (L) is considered.

The head loss (the sum of the major and minor losses) for the 12 VDC pump operation is calculated as below:

$$h_{L,total} = \left(0.0385\frac{1.274}{0.001} + \sum 1.1x50\right)\frac{6.886^2}{2x9.81} = 251.46\,m$$

The total head loss is calculated as 251.46 m. The head loss can be presented with a *Pa* unit with the help of Equation 4.9. The density ρ of the ethanol is determined as $786.6\ kg/m^3$ experimentally in Section 5.3.

$$\Delta P_L = h_L \rho g = 251.46\,m\ x\ 786.6\ kg/m^3 x\ 9.81\ m/s^2 = 1.94\ MPa$$

1.94 MPa head pressure drop is determined throughout the channels. Thereby, the required pumping power can be calculated with the help of Equation 4.10 using the head pressure drop and volume flow rate values.

$$\dot{W}_{pump} = \dot{V}\Delta P_L = 6.886x10^{-6}\ m^3/s\ x\ 1.94\ MPa = 13.36\ W$$

The pumping power is determined as 13.36 W. The total energy consumption of the pump is 80 W with 12 VDC operation as presented in Table 4.2. The proportion of the pumping power to the overall energy consumption gives the energy ratio to overcome pressure losses through the channels.

$$13.36/80 = 0.167 = 16.7\%$$

The pump consumed 16.7% of its energy to overcome pressure losses. A similar calculation is performed using the efficiency equation (4.12):

$$\eta_{pump} = \frac{\rho g \dot{V} H}{bhp}$$

$$= \frac{786.6\ kg/m^3\ x\ 9.81\ m/s^2 x\ 1.589x10^{-6}\ m^3/s\ x\ 251.46\,m}{80\ W}$$

$$= 16.7\%$$

Equation 4.12 was solved for the 12VDC operation above. The pumping power and efficiency calculations were matched one by one. Therefore, the theoretical analysis was validated using experimental data. The same calculations were repeated by following the same solution steps for the 9, 6, and 3 VDC pump operating voltages. All results are presented in Table 5.6.

The mean velocity, Reynolds number, Darcy friction factor, head loss, pressure loss, the required pumping power, and the pump efficiency values were calculated for each corresponding operating voltage of the pump and presented in Table 5.6. The average velocity and Reynolds number decreased with the decreasing of operating voltage. All corresponding Reynolds numbers were found in the turbulent region without 3VDC operation. Therefore, the calculations were performed considering the laminar conditions and equations for the 3V pump operation. The entrance length is very long for 3VDC operation as seen in the table. The main reason for this is the region of flow which is laminar conditions. Nevertheless, the pump consumed only 17.58% part of the energy to overcome pressure losses under the mentioned conditions. Head loss and head pressure values of all conditions seem to be high. It is derived from the microchannel structure of the geometry and long circulation distance. Because the channels have only a 1-mm-width and the circulation distance is 1274 mm against this. The considered structure leads to pressure increase and load on pumping power, at the same time. Therefore, there is no doubt in the calculations and even it is proved with the pumping power requirements. Besides, the matching of the pumping power and the pump efficiency is validated by the used experimental data. Darcy friction factor, *f*, increased with the lowering of the pump operation voltage. As expected, the frictional forces increased with decreasing the mass flow rate. Correlatively, the Darcy factor increased with the increase of contact and friction points of the fluid throughout the circulation. Another important note can be reported by the loss coefficient (K_L).

Table 5.6. Fluid flow properties of the pump at different operating voltages

Mass Flow Rate, $\dot{m}$ (kg/s)	Mean Velocity, V_{avg} (m/s)	Reynolds Number	Entrance Length, L_h (m)	Darcy Friction Factor, f	Head Loss, h_L (m)	Head Pressure, ΔP_L (MPa)	Pumping Power (W)	Pumping Power Ratio (%)	Pump Efficiency η (%)
0.00125	1.589	1316	65.8	0.048632	15.05	0.116	0.185	17.58	17.58
0.00291667	3.70794	3072	0.01012	0.045	78.7	0.617	2.252	21.45	21.45
0.00433333	5.50894	4564	0.01117	0.041	165.87	1.28	7.05	17.63	17.63
0.00541667	6.886	5705	0.0118	0.0385	251.46	1.94	13.36	16.7	16.7

Operating Voltage (V)	**3**	**6**	**9**	**12**

The loss coefficient was assigned as 1.1 aforementioned. It is added from the pressure losses section of the Fluid Mechanics book (Çengel and Cimbala, 2020), naturally. However, it is the peak point of the loss (90º elbow). That is the calculated head losses and head pressures correspond to the highest value. Any changes in the loss coefficient affect the loss level, and consequently power and efficiency calculations.

5.16. Heat Transfer Analysis

A heat transfer analysis was performed for the pump operation voltage, initially. The ethanol was heated to 40 ℃ and then sent to the anode and cathode sides of the stack as presented in Section 5.7. The heated ethanol was circulated with a different operating voltage of the pump which was 3, 6, 9, and 12 VDC. The n coefficient of the Prandtl number was considered as 0.4 for the heating process. The other specifications of the ethanol were assigned corresponding operation temperatures.

The thermal conductivity, k, and the specific heat capacity, c_p of the ethanol at 40 ℃ is $0.164\,W/m.K$ and $2574\,J/kg.K$, respectively. The first analysis was conducted for the 12 VDC operation of the pump. The Reynolds number calculated in the previous section is 5705 and is in the turbulent region. The hydraulic diameter of the square duct is equal to a side length which 0.001 m. The heat transfer coefficient, h can be calculated by solving Equation 4.20 using the initial parameters.

$$Nu = \frac{hD_h}{k} = 0.023Re^{0.8}Pr^{0.4} = 0.023x5705^{0.8}x12.6316^{0.4} = 64.17$$

$$h = \frac{k}{D_h} Nu = \frac{0.164\ W/m.K}{0.001\ m} 64.17 = 10523.48\ W/m^2.K$$

The heat transfer coefficient, h is calculated as $10523.48\ W/m^2.K$ for the 12 VDC pump operation. The exit temperature of the ethanol can be calculated with the help of Equation 4.16 using the known initial values.

$$T_e = T_s - (T_s - T_i)\ exp(-hA_s/\dot{m}c_p)$$

Herein, A_s is the cross-sectional heat transfer area and is calculated as below and the exit temperature of the coolant, is then, determined. T_s denotes the constant surface temperature and equal to -10 ℃, T_i denotes the inlet temperature of the ethanol and is equal to 40 ℃.

$$A_s = pL = 4aL = 4\ x\ 0.001\ m\ x\ 1.274\ m = 0.005096\ m^2$$

$$T_e = -10 - (-10 - 40) \exp\left(\frac{-10523.48\ W/m^2.K\ x\ 0.005096\ m^2}{0.00541667\ kg/s\ x\ 2574\ J/kg.K}\right)$$

$$T_e = -8.93\ ℃$$

Therefore, the heat transfer ratio can be specified with the help of Equation 4.17. Herein, the bulk mean fluid temperature specifications were calculated using the specific heat value of the ethanol according to ~16 ℃ ($(T_b = (T_i + T_e)/2) = (40 - 8.93)/2 = \sim 16$ ℃).

$$\dot{Q} = \dot{m}c_p(T_e - T_i)$$

$$= 0.00541667\ kg/s\ x\ 2368\ J/kg.K\ x\ (-8.93℃ - 40℃) = -627.61\ W$$

However, the heat transfer ratio can be calculated with the help of Equation 4.18 considering the log mean temperature difference.

$$\Delta T_{lm} = \frac{T_i - T_e}{\ln[(T_s - T_e)/(T_s - T_i)]}$$

$$= \frac{40℃ - (-8.93℃)}{\ln[(-10℃ + 8.93℃)/(-10℃ - 40℃)]} = -12.73℃$$

$$\dot{Q} = hA_s\Delta T_{lm}$$

$$= 10523.48\, W/m^2.K\ x\ 0.005096\, m^2\ x\ (-12.73℃) = -682.56\, W$$

The heat transfer ratio from the warmed ethanol is calculated in two ways. The findings are matched as seen from the calculations. Nevertheless, the heat transfer findings with the log mean temperature difference method is close to real conditions due to the logarithmic temperature values were considered instead of mean temperature values. In addition, the used Prandtl number, the specific heat capacity of the fluid, and the other magnitudes used in the calculations affect the result, directly. Thereby, small errors can be derived by the sensitivity level of the used values.

Herein, an extra calculation was provided with NTU evaluation which is a measure of heat transfer area and effectiveness of a system. NTU of the 12 VDC pump operation is determined with the help of Equation 4.21.

$$NTU = hA_s/\dot{m}c_p = \frac{-10523.48\, W/m^2.K\ x\ 0.005096\, m^2}{0.00541667\, kg/s\ x\ 2574\, J/kg.K} = 3.84$$

If the NTU is near 5 or lower than this, heat transfer is possible still. Whereas higher than this value is pointed out that the heat transfer does not continue no matter how much we extend the length of the duct. Herein, the found NTU is proved that the possible heat transfer seems in the system. The same calculations were performed

for the 9, 6, and 3VDC operation of the pump using the same equations and techniques. The Reynolds number of the 3VDC operation is 1316 and is in the laminar region. Therefore, the heat transfer characteristics of the 3VDC operation are determined considering the laminar conditions.

Table 5.7. Heat transfer characteristics of the pump at different operating voltages

Nusselt Number, Nu	**Heat Transfer Coefficient, h (W/m.K)**	**Reynolds Number**	**Exit Temperature, T_e (ºC)**	**Heat Transfer Ratio, $\dot{Q}_1$ (W)**	**Log Mean Temperature Difference, ΔT_{lm} (ºC)**	**Heat Transfer Ratio, $\dot{Q}_2$ (W)**	**NTU**
4.35	714.1	1316	6.13	-103.26	-29.93	-108.95	1.13
39.1	6413.5	3072	-9.36	-340.89	-11.33	-370.15	4.35
53.68	8802.9	4564	-9.1	-503.87	-12.22	-548.27	4.02
64.17	10823.48	5705	-8.93	-621.61	-12.73	682.56	3.84

Operating Voltage (V)	3	6	9	12

All calculations are presented in Table 5.7. The Nusselt numbers, heat transfer coefficients and ratios, exit temperatures, and NTU values of the corresponding operation voltage are given, separately. The higher the mass flow rate, the higher the heat transfer. With the increase in the operating voltage of the pump, the heat transfer ratio is increased, as seen. The heat transfer ratios were presented using minus (-) sign due to the heat extracted from the coolant. The heat transfer coefficients were found pretty high without 3VDC operation. Herein, some troubles can be originated from the 3V operation calculations. The determined specifications were found by the following laminar conditions due to the assigned Reynolds number. The other findings (6, 9, and 12VDC operations) depend on the turbulent flow regions and showed similar characteristics. The ethanol is lost its energy when circulating throughout the flow channels. Herein, the heat and pressure losses through the connection pipes were neglected. In addition, the heat transfer ratio can be increased with the decreasing of pumping requirements, initially. Then, coolant with an appropriate heat transfer capacity rather than ethanol may contribute to heat transfer.

Another heat transfer analysis was performed related to cases and comparison studies. These analyses were time-depended and include the warm-up profile of the coolant throughout the heater operation. In the previous sections, the stack and the external heating mechanism were operated synchronously. The temperature profiles of the 20 s heater, 150 s pump operation, and 15 s heater, 262.5 s pump operation cases were evaluated and compared, in general. At this point, a heat transfer analysis is required to understand the effectiveness and limitations of the compared cases.

The temperature increase of the ethanol by the effect of heater operation can be determined easily. Herein, the pump was operated at full power (12V) and the c_p value of the ethanol was considered at -10 ℃ which is $2192\ J/kg.K$. In addition, the volume of the ethanol was kept for all cases at 0.5 liters. In heat transfer calculations, the volume of the ethanol should be converted to the kg unit.

$$\dot{Q} = \dot{m}c_p(T_e - T_i)$$

Equation 4.14 above should be solved to calculate the temperature difference at the end of the warming process by the heater. $\dot{Q}$ is a time-independent heat transfer ratio, but Q is a time-dependent heat transfer ratio and is dependent on the operation duration of the heater. Considering case #1, the heater was operated for 20 seconds. Therefore 1800 W (heater power) heater was operated for 20 seconds and it consumed 36000 Joule energy as calculated below.

$$Q = 1800\ W\ x\ 20\ s = 36000\ J = 36\ kJ = mc_p(T_e - T_i)$$

Hence, the mass of the ethanol can be found by conversion of liter to kg. The c_p value of the ethanol is taken to be $2192\ J/kg.K$ considering the operation temperature of the ethanol (-10 ℃). In addition, the density of the ethanol is evaluated as $816\ kg/m^3$ corresponding to the operating temperature.

$$m = 0.5\ L\ x\ 0.816\ kg/L = 0.408\ kg$$

$$Q = 36000\ J = 0.408\ kg\ x\ 2192\ J/kg.K\ x\ \Delta T$$

$$\Delta T = 40.25\ ℃$$

The temperature difference is calculated as 40.25℃ for the -10 ℃ condition. Actually, similar results will be obtained at lower cold start temperatures with small differences. This difference originated from the change in the specific heat value of

the ethanol at lower temperatures. In the second case, the heater was operated for 15 seconds. With the same calculations:

$$Q = 1800\,W\ x\ 15\,s = 27000\,J = 27\,kJ = mc_p(T_e - T_i)$$

$$Q = 27000\,J = 0.408\,kg\ x\ 2192\,J/kg.K\ x\ \Delta T$$

$$\Delta T = 30.19\,℃$$

Surely, the higher the operation duration of the heater, the higher the heat transfer and the higher the temperature increase. In the second case, the temperature increase is calculated as 30.19 ℃, theoretically. There is a 10 ℃ difference between the cases, approximately. That is the temperature can increase to ~30 and ~20 ℃ for the 20 and 15 s heater operation at -10 ℃ cold start tests (with ethanol cycles). It is proved by the findings at -10 ℃ cold start operation with ethanol as presented in Figure 5.4, Figure 5.13, and Figure 5.17. The temperature increased to ~30 ℃ levels at the maximum in which the heater was operated for 20 s in both figures. Similarly, the temperature increased to ~22 ℃ levels at the maximum in which the heater was operated for 15 s when investigated in Figure 5.18. Herein, the theoretical calculations were validated using experimental data. Low differences between the temperature values can be seen between the theoretical and experimental-based data. It should be noted that the calculations do not include the operation of the single-cell stack. Because the cell is generated heat throughout the operation and contributes to temperature increase in the cell. It should be remembered that a ~2.5 ℃ temperature increase was achieved by the self-operation of the stack at 1.5 A current level approximately as shown in Figure 5.2. At the same time, continuous heat loss is experienced in the environment throughout all cold start tests. The calculations should be balanced with the heat gains and losses. However, we reached exact temperature values with the help of temperature following the tests. Therefore, it enables comparison between experimental and theoretical calculations.

6. CONCLUSION AND FUTURE WORKS

The sub-zero operation of the PEM fuel cell depends on both operation parameters and fuel cell specifications. An optimization can be provided by controlling these parameters. In this thesis study, the coolant heating method which raises the temperature of the single-cell stack from sub-zero temperatures by heating coolant using an electrical heater is implemented. The main advantages of this method can be highlighted as providing a fairly homogeneous temperature profile and not causing any stress in the cell. Thanks to the established experimental setup, the constant mass working fluid (mostly ethanol) was kept in an instant electric heater and upon the start of the cold start test; on the one hand, it was heated by an electric heater, on the other hand, it was circulated bilaterally through the channels machined to the backside of the bipolar plates to warm-up the single-cell stack. At the same time, the reactions occurring in the cell by sending gas to the cell also contributed to the increase in temperature. Cold start tests were carried out at temperatures of -10, -15, -20, -25, and -30 ℃ by keeping the whole system in a conditioning cabinet, and the effects of some operating parameters were investigated and compared. The main findings may be listed below:

- In the initial stage, it was proved with the two initial cold start tests that the cell may not be survived without any assistance. Then, it is approved that the anode and the cathode compartments are heated equally. This validation has important to evaluate case studies accurately.
- The aqueous solutions (20:80% in wt.) of the ethanol, methanol, ethylene glycol, and propylene glycol fluid were evaluated to specify the best coolant which provides the most efficient, rapid, and homogeneous temperature distribution. The ethanol solution is the most attractive and appropriate working fluid to provide enhanced cold start operation. On the other hand, it was reported that the aqueous solutions

of ethylene glycol and propylene glycol are not satisfied the required viscosity and heat transfer coefficient.

- Although no significant difference is not recorded between the cases, the 12VDC pump operation is provided the most effective heating way, as expected. High coolant flow rates ensure high and fast heat transfer. 6VDC pump operating voltage may be preferred around the -10 ºC cold start temperatures. Nevertheless, full pump power (12VDC) may be interiorized at harsh conditions (-20, -30 ºC) to provide rapid warm-up.
- A highly smooth temperature and current profile were obtained with the double-side heating strategy. The temperature increased above zero in 13.3 seconds (T_3 point), and the stack arrived at 30.8 ºC maximum temperature and kept its status at 13 ºC to the end of the test.
- The first failed case was experienced with the 20 s heater and 150 s pump operation at the -20 °C test and the second failed case was experienced with the 20 s heater and 150 s pump operation at the -25 °C test.
- A highly stable and homogeneous temperature profile was ensured by the long pump operation. Therefore, a cold start with a long pump operation was found more successful rather than a long heater operation duration under the same energy consumption levels.

Although instant heating and high temperature levels were supplied with long heater durations, it is understood that the instant temperature decreases after long heater operation, and low pump operation cases are dragged to cell instability. In light of the experimental observations, the direction of the future works, and possible and appropriate improvements can be referred to as given below:

- Undoubtfully, the coolant heating approach is a very strong and effective way to deliver fresh heat to the cell rapidly and homogeneously. The positive sides and drawbacks of heating equipment were specified in this thesis study. However, the effectiveness of the equipment should be tested at stack-level experiments. Because the heat generation and correlatively survivability level of the stacks are higher than the single-cell option. Thus, the importance of the self-stack operation (thanks to generated heat by the stack) can be highlighted. In this study, it was reported that the cell can increase the whole stack temperature ~2.5 ℃ at maximum. It is obvious that a higher temperature increase will be provided by stack-level experiments.
- Another further improvement can be achieved by testing the system at the ultimate assisted-cold start temperature (-40 ℃). The cold start tests were conducted at -30 ℃ as the lowest starter temperature due to the limitation of the environmental chamber operating temperature (between -30 and 165 ℃). The author believes that a successful cold start may be managed thanks to the established setup (the operating temperature range of the auxiliary heating mechanism equipment should be considered).
- The antifreeze agent application during the start-up may be an alternative solution in addition to the current method. The stack was warmed-up by the heating of coolant (mostly ethanol) in the experiments of this thesis study. An exothermic reaction of two or more substances can be considered an alternative solution method. Thereby, the heat will be used to heat stack instead of coolant energy.

REFERENCES

Abe, H., Asano, Y., Kai, M., 2004. Start Control Device for Fuel Cell System, U.S. Patent, Nov. 9, US 6 815 103 B2.

Amamou, A., Kandidayeni, M., Boulon, L., Kelouwani, S., 2018. Real Time Adaptive Efficient Cold Start Strategy for Proton Exchange Membrane Fuel Cells. Applied Energy, 216:21-30.

Amamou, A.A., Kelouwani, S., Boulon, L., Agbossou, K., 2016. A comprehensive Review of Solutions and Strategies for Cold Start of Automotive Proton Exchange Membrane Fuel Cells. IEEE Access, 4:4989-5002.

Appleby, A.J., Electrochemical Energy – Progress Towards a Cleaner Future: Lead/Acid Batteries and the Competition. Journal of Power Sources, 53, 187-197.

Assarabowski, R.J., Unkert, W.T., Bach, L.A., Grasso, A.P., Olsommer, B.C., 2004. Method and Apparatus for Preventing Water in Fuel Cell Power Plants from Freezing During Storage. US Patent, Sep. 28, US 6 797 421 B2.

Barbir, F., 2005. PEM Fuel Cells, Theory and Practice. Academic Press, Elsevier, p. 433.

Bargal, M.H.S., Abdelkareem, M.A.A., Tao, Q., Li, J., Shi, J., Wang, Y., 2020. Liquid Cooling Techniques in Proton Exchange Membrane Fuel Cell Stacks: A Detailed Survey. Alexandria Engineering Journal, 59:635-655.

Biesdorf, J., Stahl, P., Siegwart, M., Schmidt, T.J., Boillat, P., 2015. When Size Matters: Active Area Dependence of PEFC Cold Start Capability. Journal of The Electrochemical Society, 162(10):F1231-F1235.

Birk, W., 2004. Fuel Cell System and Method for Starting a Fuel Cell System. US Patent, Jun. 29, US 6 756 143 B2.

Bradean, R.P., Haas, H.R., Richards, C.J., Adam, D.D.L., 2006. Shutdown Methods and Designs for Fuel Cell Stacks. US Patent, Sep. 21, US 2006/0210856 A1.

Breault, R.D., Hagans, P.L., 2006. Method of Operating a Fuel Cell System Under Freezing Conditions. US Patent, May. 23, US 7 049 018 B2.

Burden, R.L., Faires, J.D., 2010. Numerical Analysis, 9th Ed., Brooks/Cole Cengage Learning, Boston, USA, p. 895.

Cao, Y., Li, Y., Zhang, G., Jermsittiparsert, K., Razmjooy, N., 2019. Experimental Modeling of PEM Fuel Cells Using a New Improved Seagull Optimization Algorithm. Energy Reports, 5:1616-1625.

Çengel, Y.A., Cimbala, J.M., 2020. Fluid Mechanics: Fundamentals and Applications. McGraw-Hill Education, 4th Edition, p. 1024.

Çengel, Y.A., Ghajar, A.J., 2020. Heat and Mass Transfer: Fundamentals and Applications. McGraw-Hill Education, 6th Edition, p. 1018.

Chen, H., Song, Z., Zhao, X., Zhang, T., Pei, P., Liang, C., 2018. A Review of Durability Test Protocols of the Proton Exchange Membrane Fuel Cells for Vehicle. Applied Energy, 224:289-299.

Chen, H., Zhao, X., Zhang, T., Pei, P., 2019. The Reactant Starvation of the Proton Exchange Membrane Fuel Cells for Vehicular Applications: A Review. Energy Conversion and Management, 182:282-298.

Chen, Q., Zhang, G., Zhang, X., Sun, C., Jiao, K., Wang, Y., 2021. Thermal Management of Polymer Electrolyte Membrane Fuel Cells: A Review of Cooling Methods, Material Properties, and Durability. Applied Energy, 286:116496.

Chippar, P., Ju, H., 2012. Evaluating Cold-Start Behaviors of End and Intermediate Cells in a Polymer Electrolyte Fuel Cell (PEFC) Stack, Solid State Ionics, 225:85-91.

Cho, EA., Ko, J-J., Ha, H.Y., Hong, S-A., Lee, K-Y., Lim, T-W., Oh, I-H., 2004. Effects of Water Removal on the Performance Degradation of PEMFCs Repetitively Brought to <0°C. Journal of The Electrochemical Society, 151(5):A661-A665.

Colbow, K.M., van der Geest, M., Longley, C.J., Müller, J., Roberts, J., St-Pierre, J., Urban, P., Wezel, R., Wilkinson, D.P., Zhang, J., 2002. Method and Apparatus for Operating an Electrochemical Fuel Cell with Periodic Reactant Starvation. US Patent, Oct. 29, US 6 472 090 B1.

Couch, H.T., Sribnik, F., 2004. Configuration Enabling Rapid Fuel Cell Power From Sub-Freezing Initial Condition. US Patent, Aug. 10, 6 773 840 B2.

Dafalla, A.M., Jiang, F., 2018. Stresses and Their Impacts on Proton Exchange Membrane Fuel Cells: A review. International Journal of Hydrogen Energy, 43:2327-2348.

Darıcık, F., Topcu, A., Tüccar, G., Aydın, K., 2019. Effects of Fibre Orientations and Flow Channel Patterns on the Durability of Composite Bipolar Plates Used in PEMFCs. IEEE, 8th International Conference on Modeling, Simulation and Applied Optimization, April 15-17, Bahrain.

Docter, A., Frank, G., Konrad, G., Lamm, A., Mueller, J.T., 2003. Fuel Cell and Method for Cold-Starting such a Fuel Cell. US Patent, Oct. 9, 2003/0190507 A1.

Docter, A., Frank, G., Konrad, G., Lamm, A., Mueller, J.T., 2008. Fuel Cell and Method for Cold-Starting such a Fuel Cell. US Patent, May 1, US 2008/0102327 A1.

Du, Q., Jia, B., Luo, Y., Chen, J., Zhou, Y., Jiao, K., 2014. Maximum Power Cold Start Mode of Proton Exchange Membrane Fuel Cell. International Journal of Hydrogen Energy, 39(16):8390-8400.

Dursch, T.J., Trigub, G.J., Liu, J.F., Radke, C.J., Weber, A.Z., 2013. Non-isothermal melting of ice in the gas-diffusion layer of a proton-exchange-membrane fuel cell. International Journal of Heat and Mass Transfer, 67:896-901.

Elhamid, MHA., Mikhail, Y.M., Blunk, R.H., Lisi, D.J., 2004. Inexpensive Dielectric Coolant for Fuel Cell Stacks, US Patent, May 25, US 6 740 440 B2.

Ertürk, A.T., Ergin, U., Kadıoglu, T., Türkmen, A.C., Çelik, C., 2022. Metal Foams as a Gas Diffusion Layer in Direct Borohydride Fuel Cells. International Journal of Hydrogen Energy, 47(55):23373-23380.

Evangelisti, S., Tagliaferri, C., Brett, D.J.L., Lettieri, P., 2017. Life Cycle Assessment of a Polymer Electrolyte Membrane Fuel Cell System for Passenger Vehicles. Journal of Cleaner Production, 142:4339-4355.

Fuller, T.F., Wheeler, D.J. 2000. Start Up of Cold Fuel Cell. US Patent, May 30, US 6 068 941.

Fuller, T.F., Wheeler, D.J., 2000. Start Up of Frozen Fuel Cell. US Patent, Aug. 15, 6 103 410.

Gebhardt, U., Mund, K., Waidhas, M., 2003. Method for Cold Starting Fuel Cells of a Fuel Cell Facility, and Corresponding Fuel Cell Facility, US Patent, May 15, US 2003/0091875 A1.

Gencoglu, M.T., Ural, Z., 2009. Design of a PEM Fuel Cell System Residential Application. International Journal of Hydrogen Energy, 34:5242-5248.

Ghadimi, M., Momenifar, M., Barzegari, M.M., Mohammadi, K., 2022. Mechanical and Chemical Characteristics of PEM Fuel Cell Sealants in a Simulated Environment. Iranian Journal of Hydrogen & Fuel Cell, 2:163-178.

Gomez, A., Sasmito, A.P., Shamim, T., 2015. Investigation of the Purging Effect on a Dead-end Anode PEM Fuel Cell-powered Vehicle During Segments of a European Driving Cycle. Energy Conversion and Management, 106:951-957.

Gong, A., Verstraete, D., 2017. Fuel Cell Propulsion in Small Fixed-Wing Unmanned Aerial Vehicles: Current Status and Research Needs. International Journal of Hydrogen Energy, 42:21311-21333.

Guo, H., Sun, S., Yu, H., Lu, L., Xu, H., Shao, Z., 2019. Proton Exchange Membrane Fuel Cell Subzero Start-Up with Hydrogen Catalytic Reaction Assistance. Journal of Power Sources, 429:180-187.

Guo, X., Peng, X., Xu, S., 2017. Numerical Models for PEMFC Cold Tart: A Review. SAE International Journal of Alternative Powertrains, 6(1), 151-164.

Gwak, G., Ju, H., A Rapid Start-Up Strategy for Polymer Electrolyte Fuel Cells at Subzero Temperatures Based on Control of the Operating Current Density. International Journal of Hydrogen Energy, 40:11989-11997.

Gwak, G., Ko, J., Ju, H., 2014. Numerical Investigation of Cold-Start Behavior of Polymer-Electrolyte Fuel-Cells from Subzero to Normal Operating Temperatures – Effects of Cell Boundary and Operating Conditions, International Journal of Hydrogen Energy. 39:21927-21937.

Han, K., Hong, B.K., Kim, S.H., Ahn, B.K., Lim, T.W., 2011. Influence of Anisotropic Bending Stiffness of Gas Diffusion Layers on the Degradation Behavior of Polymer Electrolyte Membrane Fuel Cells under Freezing Conditions. International Journal of Hydrogen Energy, 36:12452-12464.

Hayashi, K., Inai, S., Kato, H., Jimba, R., Mohri, M., Morikawa, H., Yoshida, H., 2009. Method of Starting Up Operation of Fuel Cell at Low Temperature, US Patent, Sep. 15, US 7 588 844 B2.

Henao, N., Kelouwani, S., Agbossou, K., Dubé, Y., 2012. Proton Exchange Membrane Fuel Cells Cold Startup Global Strategy for Fuel Cell Plug-In Hybrid Electric Vehicle. Journal of Power Sources, 220:31-41.

Hirakata, S., Mochizuki, T., Uchida, M., Uchida, H., Watanabe, M., 2013. Investigation of the Effect of Pore Diameter of Gas Diffusion Layers on Cold Start Behavior and Cell Performance of Polymer Electrolyte Membrane Fuel Cells. Electrochimica Acta, 108:304-312.

Huo, S., Cooper, N.J., Smith, T.L., Park, J.W., Jiao, K., 2017. Experimental Investigation on PEM Fuel Cell Cold Start Behavior Containing Porous Metal Foam as Cathode Flow Distributor. Applied Energy, 203:101-114.

Huo, S., Jiao, K., Park, J.W., 2019. On the Water Transport Behavior and Phase Transition Mechanisms in Cold Start Operation of PEM Fuel Cell. Applied Energy, 233-234:776-788.

Incropera, F.P., DeWitt, D.P., Bergman, T.L., Lavine, A.S., 2006. Introduction to Heat Transfer, Wiley, 5th Ed., p. 912.

Irshad, M., Siraj, K., Raza, R., Ali, A., Tiwari, P., Zhu, B., Rafique, A., Ali, A., Ullah, M.K., Usman, A., 2016. A Brief Description of High Temperature Solid Oxide Fuel Cell's Operation, Materials, Design, Fabrication Technologies and Performance. Applied Sciences, 6(75):2-23.

Jałowiecka, M., Bojarska, Z., Małolepszy, A., Makowski, Ł., 2023. Mass Transport Enhancement in Direct Formic Acid Fuel Cell with a Novel Channel Design. Chemical Engineering Journal, 451(1):138474.

Jiang, F., Wang, C-Y., Chen, K-S., 2010. Current Ramping: A Strategy for Rapid Start-Up of PEMFCs From Sunfreezing Environment. Journal of The Electrochemical Society, 157(3):B342-B347.

Jiao, K., Li, X., 2011. Water Transport in Polymer Electrolyte Membrane Fuel Cells. Progress in Energy and Combustion Science, 37:221-291.

Jo, A., Le, S., Kim, W., Ko, J., Ju, H., 2015. Large-Scale Cold-Start Simulations for Automotive Fuel Cells. International Journal of Hydrogen Energy, 40:1305-1315.

Kahraman, H., Çevik, İ., 2014., PEM Yakıt Hücrelerindeki Akış Kanal Tasarımlarının İncelenmesi. Tukish Journal of Nature and Science, 3(2):27-36.

Kandlikar, S.G., Lu, Z., 2009. Fundamental Research Needs in Combined Water and Thermal Management within a Proton Exchange Membrane Fuel Cell Stack under Normal and Cold-Start Conditions. Journal of Fuel Cell Science and Technology, 6(4), 044001:1-13.

Khandelwal, M., Lee, S., Mench, M.M., 2007. One-Dimensional Thermal Model of Cold-Start in a Polymer Electrolyte Fuel Cell Stack. Journal of Power Sources, 172:816-830.

Knorr, F., Sanchez, D.G., Schirmer, J., Gazdzicki, P., Friedrich, K.A., 2019. Methanol as Antifreeze Agent for Cold Start of Automotive Polymer Electrolyte Membrane Fuel Cells. Applied Energy, 238:1-10.

Ko, J., Kim, W., Hong, T., Kim, D., Ju, H., 2012. Impact of Metallic Bipolar Plates on Cold-Start Behaviors of Polymer Electrolyte Fuel Cells (PEFCs). Solid State Ionics, 225:260-267.

Koçak, N.F., Topcu, A., Aydın, K., Çelik, S., Topcu, M. Experimental Studies on Flow Fields of Bipolar Plate. Academic Perspective Procedia, 2019, 2(3):730-739.

Korytnikov, K., 2012. Method and Apparatus for PEM Fuel Cell Freezing Protection. US Patent, Apr. 3, US 8 148 024 B2.

Korytnikov, K., Novak, P., 2005. Method and Apparatus for Cold-Starting A PEM Fuel Cell (PEMFC), and PEM Fuel Cell System. US Patent, Oct. 13, US 2005/0227126 A1.

Kumar, A., Reddy, R.G., 2004. Materials and Design Development for Bipolar/end Plates in Fuel Cells. Journal of Power Sources, 129:62-67.

Leo, T.J., Durango, J.A., Navarro, E., 2010. Exergy Analysis of PEM Fuel Cells for Marine Applications. Energy, 35:1164-1171.

Li, C., Si, D., Liu, Y., Zhang, J., Liu, Y., 2021a. Water Management Characteristics of Electrospun Micro-Porous Layer in PEMFC under Normal Temperature and Cold Start Conditions. International Journal of Hydrogen Energy, 46:11150-11159.

Li, L., Wang, S., Wang, G., Yue, L., Takuto, A., 2019a. Effect of Clamping Stress on Cold Start Performance of PEMFC. Energy Procedia, 158:1744-1749.

Li, L., Wang, S., Yue, L., Wang, G., 2019. Cold-Start Icing Characteristics of Proton-Exchange Membrane Fuel Cells. International Journal of Hydrogen Energy, 44:12033-12042.

Li, L., Wang, S., Yue, L., Wang, G., 2019b. Cold-Start Method for Proton-Exchange Membrane Fuel Cells Based on Locally Heating the Cathode. Applied Energy, 254:113716.

Li, Q., Liu, Z., Sun, Y., Yang, S., Deng, C., 2021b. A Review on Temperature Control of Proton Exchange Membrane Fuel Cells. Processes, 9, 235:1-22.

Li, X., Sabir, I., 2005. Review of Bipolar Plates in PEM Fuel Cells: Flow-Field Designs. International Journal of Hydrogen Energy, 30:359-371.

Li, Y., Xu, S., Yang, Z., Li, Y., 2011. Experiment and simulation study on cold start of automotive PEMFC. IEEE, International Conference on Electric Information and Control Engineering, April 15-17, Wuhan, China.

Limbergen, T.V., Bonné, R., Hustings, J., Valcke, R., Thijs, S., Vangronsveld, J., Manca, J.V., 2022. Plant Microbial Fuel Cells from the Perspective of Photovoltaics: Efficiency, Power, and Applications. Renewable and Sustainable Energy Reviews, 169:112953.

Lin, B., 2006. Thermal Control of Fuel Cell for Improved Cold Start. US Patent, Dec. 28, US 2006/0292406 A1.

Lin, B., 2009. Thermal Control of Fuel Cell for Improved Cold Start. US Patent, May 19, 7 534 511 B2.

Lin, R., 2021. Experimental Validation for Enhancement of PEMFC Cold Start Performance: Based on the Optimization of Micro Porous Layer. Applied Energy, 300:117306.

Liu, H., Si, D., Ding, H., Wang, S., Zhang, J., Liu, Y., 2021a. Cold Start Capability and Durability of Electrospun Catalyst Layer for Proton Exchange Membrane Fuel Cell, International Journal of Hydrogen Energy, 46:11140-11149.

Liu, J., Ciu, H., Gao, L., Wang, J., Wang, M., Li, F., 2021b. Research Status of Thermal Management of Hydrogen Energy Proton Exchange Membrane Fuel Cell. Journal of Physics: Conference Series, 2108, 012093:1-7.

Liu, J., Laghrouche, S., Ahmed, F-S., Wack, M., 2014. PEM Fuel Cell Air-Feed System Observer Design for Automotive Applications: An Adaptive Numerical Differentiation Approach. International Journal of Hydrogen Energy, 39:17210-17221.

Liu, P., Xu, S., 2020. A Progress Review on Heating Methods and Influence Factors of Cold Start for Automotive PEMFC System. SAE Technical Paper, 2020-01-0852.

Luo, M., Zhang, J., Zhang, C., Chin, C.S., Ran, H., Fan, M., Du, K., Shuai, Q., 2022. Cold Start Investigation of Fuel Cell Vehicles with Coolant Preheating Strategy. Applied Thermal Engineering, 201:e117816.

Luo, Y., Jiao, K., 2018. Cold Start of Proton Exchange Membrane Fuel Cell. Progress in Energy and Combustion Science, 64:29-61.

Ma, J., Zhang, C., Xi, F., Chen, W., Jiao, K., Du, Q., Bai, F., Liu, Z., 2023. Experimental Study on the Influence of Environment Conditions on the Performance of Paper-based Microfluidic Fuel Cell. Applied Thermal Engineering, 219(B):119487.

Madheswaran, D.K., Jayakumar, A., Varuvel, E.G., 2022. Recent Advancement on Thermal Management Strategies in PEM Fuel Cell Stack: A Technical Assessment from the Context of Fuel Cell Electric Vehicle Application. Energy Sources, Part A: Recovery, Utilization, and Environmental Effects, 44(2):3100-3125.

Maes, J-P., Lievens, S., 2007. Methods for Fuel Cell Coolant Systems. US Patent, Apr. 10, US 7 201 982 B2.

Matsuoka, N., 2006. Warm-up of Fuel Cell Power Plant. US Patent, Sep. 19, US 7 108 928 B2.

Mench, M.M., 2008. Fuel Cell Engines. John Wiley & Sons, Inc., Hoboken, New Jersey, p.285.

Meng, H., 2008. Numerical Studies of Cold-Start Phenomenon in PEM Fuel Cells. Electrochimica Acta, 53:6521-6529.

Meng, H., Ruan, B., 2011. Numerical Studies of Cold-Start Phenomena in PEM Fuel Cells: A Review. International Journal of Energy Research, 35:2-14.

Miao, Z., Yu, H., Song, W., Hao, L., Shao, Z., Shen, Q., Hou, J., Yi, B., 2010. Characteristics of Proton Exchange Membrane Fuel Cells Cold Start With Silica in Cathode Catalyst Layers. International Journal of Hydrogen Energy, 35:5552-5557.

Mohamed, A.B., 2013. A Review of Experiments on Cold Start of PEM Fuel Cells. Applied Mechanics And Materials, 315:851-855.

Mohamed, W.A.N.W., Haziq, M., Kamil, M., 2016. Hydrogen Preheating Through Waste Heat Recovery of an Open-Cathode PEM Fuel Cell Leading to Power Output Improvement. Energy Conversion and Management, 124:543-555.

Mohapatra, S.C., 2006. Fuel Cell and Fuel Cell Coolant Compositions. US Patent, Nov. 21, US 7 138 199 B2.

Nandjou, F., Poirot-Crouvezier, J.-P., Chandesris, M., Rosini, S., Hussey, D.S., Jacobson, D.L., LaManna, J.M., Morin, A, Bultel, Y., 2016. A Pseudo-3D Model to Investigate Heat and Water Transport in Large Area PEM Fuel Cells – Part 2: Application on an Automotive Driving Cycle. International Journal of Hydrogen Energy, 41:15573-15584.

Nandy, A., Jiang, F., Ge, S., Wang, C-Y., Chen, K.S., 2010. Effect of Cathode Pore Volume on PEM Fuel Cell Cold Start. Journal of The Electrochemical Society, 157(5):B726-B736.

Öner, E., Öztürk, A., Yurtcan, A.B., 2020. Utilization of the Graphene Aerogel as PEM Fuel Cell Catalyst Support: Effect of Polypyrrole (PPy) and Polydimethylsiloxane (PDMS) Addition. International Journal of Hydrogen Energy, 45(60):34818-34836.

Oszcipok, M., Zedda, M., Hesselmann, J., Huppmann, M., Wodrich, M., Junghardt, M., Hebling, C., 2006a. Portable Proton Exchange Membrane Fuel-Cell Systems for Outdoor Applications. Journal of Power Sources, 157:666-673.

Ozden, A., Shahgaldi, S., Li, X., Hamdullahpur, F., 2019. A Review of Gas Diffusion Layers for Proton Exchange Membrane Fuel Cells - With a Focus on Characteristics, Characterization Techniques, Materials and Designs. Progress in Energy and Combustion Science, 74:50-102.

Öztürk, A., Fıçıcılar, B., Eroğlu, İ., Yurtcan, A.B., 2017. Facilitation of Water Management in Low Pt Loaded PEM Fuel Cell by Creating Hydrophobic Microporous Layer with PTFE, FEP and PDMS Polymers: Effect of Polymer and Carbon Amounts. International Journal of Hydrogen Energy, 42:21226-21249.

Öztürk, B., Topcu, A., Öztürk, S., Cora, Ö.N., 2018. Oxidation, Electrical and Mechanical Properties of Crofer®22 Solid Oxide Fuel Cell Metallic Interconnects Manufactured through Powder Metallurgy. International Journal of Hydrogen Energy, 43:10822-10833.

Pan, M., Pan, C., Li, C., Zhao, J., 2021. A Review of Membranes in Proton Exchange Membrane Fuel Cells: Transport Phenomena, Performance And Durability. Renewable and Sustainable Energy Reviews, 141, 110771:1-28.

Pan, W., Li, P., Gan, Q., Chen, X., Wang, F., Dai, G., 2020. Thermal Stability Analysis of Cold Start Processes in PEM Fuel Cells. Applied Energy, 261:114430.

Paul, B., Andrews, J., 2017. PEM Unitised Reversible/Regenerative Hydrogen Fuel Cell Systems: State of the Art and Technical Challenges. Renewable and Sustainable Energy Reviews, 79:585-599.

Penner, S.S., Appleby, A.J., Baker, B.S., Bates, J.L., Buss, L.B., Dollard, W.J., Fartis, P.J., Gillis, E.A., Gunsher, J.A., Khandkar, A., Krumpelt, M., O'Sullivan, J.B., Runte, G., Savinell, R.F., Selman, J.R., Shores, D.A., Tarman, P., 1995. Commercialization of fuel cells. Energy, 20(5):331-470.

Pesaran, A.A., Kim, G-H, Gonder, J.D., 2005. PEM Fuel Cell Freeze and Rapid Startup Investigation. National Renewable Energy Laboratory, U.S. Department of Energy.

Pistono, A.O., Rice, C.A., 2020. Automotive Subzero Cold-Start Quasi-Adiabatic Proton Exchange Membrane Fuel Cell Fixture: Design and Validation. Molecules, 25(6):1410.

Qian, Z., Fan, Y., Yue, L., Zhu, Y., Wang, S., Miyazawa, A., Ozaki, S., 2023. Performance of Proton Exchange Membrane Fuel Cells with Microporous Layer Hydrophobized by Polyphenylene Sulfide at Conventional Temperature and Cold Start. International Journal of Hydrogen Energy, In Press. https://doi.org/10.1016/j.ijhydene.2022.11.021.

Qiu, D., Peng, L., Lai, X., Ni, M., Lehnert, W., 2019. Mechanical Failure and Mitigation Strategies for the Membrane in a Proton Exchange Membrane Fuel Cell. Renewable and Sustainable Energy Reviews, 113, 109289.

Quoc, H., Nguyen, Shabani, B., 2020. Proton Exchange Membrane Fuel Cells Heat Recovery Opportunities for Combined Heating/Cooling and Power Applications. Energy Conversion and Management, 204:112328.

Rajaei, V., Rashtchi, H., Raeissi, K., Shamanian, M., 2017. The Study of Ni-based Nano-crystalline and Amorphous Alloy Coatings on AISI 304 Stainless Steel for PEM Fuel Cell Bipolar Plate Application. International Journal of Hydrogen Energy, 42(20):14264-14278.

Rajbongshi, B.M., Shaneeth, M., Verma, A., 2020. Investigation on Sub-Zero Start-up of Polymer Electrolyte Membrane Fuel Cell using Un-Assisted Cold Start Strategy. International Journal of Hydrogen Energy, 45:34048-34057.

Ramezanizadeh, M., Nazari, M.A., Ahmadi, M.H., Chen, L., 2019. A Review on the Approaches for Cooling Fuel Cells. International Journal of Heat and Mass Transfer, 139:517-525.

Reiser, C.A., 2004. Battery-Boosted, Rapid Startup of Frozen Fuel Cell. U.S. Patent, Aug. 17, US 6 777 115 B2.

Ren, P., Pei, P., Li, Y., Wu, Z., Chen, D., Huang, S., 2020. Degredation Mechanisms of Proton Exchange Membrane Fuel Cell Under Typical Automotive Operating Conditions. Progress in Energy and Combustion Science, 80:100859.

Resnick, G., Reiser, C.A., Popovich, N.A., Yi, J.S., Hagans, P.L., 2004. Maintaining PEM Fuel Cell Performance with Sub-Freezing Boot Strap Starts, US Patent, Dec. 16, WO 2004/109822 A2.

Rice, C.A., 2021. Review – Subzero Automotive Fuel Cells: Water Fill Tests vs Cold-Starts. Journal of The Electrochemical Society, 168(4), 044513:1-13.

Richards, C.J., Lin, B., 2007. Method of Commencing Operation of an Electrochemical Fuel Cell Stack from Freeze-Start Conditions. US Patent, Oct. 18, US 2007/0243428 A1.

Rivaloro, M., Rattazzi, D., Lamberti, T., Magistri, L., 2020. Clean Energy Production by PEM Fuel Cells on Tourist Ships: A Time-Dependent Analysis. International Journal of Hydrogen Energy, 45(47):25747-25757.

Roberts, J., van der Geest, M., St-Pierre, J., Wilkinson, D.P., Lee, A., Moroz, S. 2001. Method and Apparatus for Increasing the Temperature of a Fuel Cell. US Patent, Dec. 11, US 6 329 089 B1.

Roberts, J.A., St.-Pierre, J., van der Geest, M.E., Atbi, A., Fletcher, N.J., 2009. Apparatus for Improving the Cold Starting Capability of an Electrochemical Fuel Cell, U.S. Patent, Jan. 27, US 7 482 085 B2.

Roberts, J.A., St-Pierre, J., van der Geest, M.E., Atbi, A., Fletcher, N.J., 2009. Apparatus for Improving the Cold Starting Capability of an Electrochemical Fuel Cell. US Patent, Jan. 27, US 7 482 085 B2.

Rock, J.A., Plant, L.B., 2002. Cold Start-Up of a PEM Fuel Cell, US Patent, Mar. 19, 6 358 638 B1.

Rock, J.A., Plant, L.B., 2004. Method of Cold Start-Up of a PEM Fuel Cell, European Patent, Apr. 28, EP 1 113 516 B1.

Rock, J.A., Plant, L.B., 2004. Method of Cold Start-Up of a PEM Fuel Cell. European Patent Office, April 28, EP 1 113 516 B1.

Ryu, S.P., Park, S.S., Lee, N.W., Kwon, S.U., Choi, S.H., Kim, D.W., 2012. Current Collector of End Plate for Fuel Cell and Method for Controlling the Same. US Patent, May 15, US 8 178 253 B2.

Sankar, K., Jana, A.K., 2018. Nonlinear Multivariable Sliding Mode Control of a Reversible PEM Fuel Cell Integrated System. Energy Conversion and Management, 171:541-565.

Santamaria, A.D., Bachman, J., Park, J.W., 2013. Cold-start of Parallel and Interdigitated Flow-Field Polymer Electrolyte Membrane Fuel Cell. Electrochimica Acta, 107:327-338.

Sasmito, A.P., Shamim, T., Mujumdar, A.S., 2013. Passive Thermal Management for PEM Fuel Cell Stack Under Cold Weather Condition Using Phase Change Materials (PCM). Applied Thermal Engineering, 58:615-625.

Singh, B.K., Mahapatra, S.S., 2023. Performance Study of Palladium Modified Platinum Anode in Direct Ethanol Fuel Cells: A Green Power Source. Journal of the Indian Chemical Society, 100(2):100876.

Skiba, T., 2006. Vacuum Assisted Startup of a Fuel Cell at Sub-Freezing Temperature. US Patent, Sep. 26, 7 112 379 B2.

Song, W.J., Chen, H., Guo, H., Ye, F., Li, J.R., Research progress of proton exchange membrane fuel cells utilizing in high altitude environments. International Journal of Hydrogen Energy, 2022, 47(59):24945-24962.

Sørensen, B., 2012. Hydrogen and Fuel Cells, Emerging Technologies and Applications. Academic Press, Elsevier, p. 497.

St-Pierre, J., Roberts, J., Colbow, K., Campbell, S., Nelson, A., 2005. PEMFC Operational and Design Strategies for Sub Zero Environments. Journal of New Materials for Electrochemical Systems, 8:163-176.

Sulaiman, M.S., Singh, B., Mohamed, W.A.N.W., 2019. Experimental and Theoretical Study of Thermoelectric Generator Waste Heat Recovery Model

for an Ultra-Low Temperature PEM Fuel Cell Powered Vehicle. Energy, 179:628-646.

Sun, S., Yu, H., Huo, J., Shao, Z., Yi, B., Ming, P., Hou, Z., 2008. Catalytic Hydrogen/Oxygen Reaction Assisted the Proton Exchange Membrane Fuel Cell (PEMFC) Startup at Subzero Temperature. Journal of Power Sources, 177:137-141.

Sundaresan, M., Moore, R. M., 2005a. PEM Fuel Cell Stack Cold Start Thermal Model. Fuel Cells, 4:476-485.

Sundaresan, M., Moore, R. M., 2005b. Polymer Electrolyte Fuel Cell Stack Thermal Model to Evaluate Sub-Freezing Startup. Journal of Power Sources, 145:534-545.

Taghiabadi, M.M., Zhiani, M., Silva, V., 2019. Effect of MEA Activation Method on the Long-Term Performance of PEM Fuel Cell. Applied Energy, 242:602-611.

Tang, T., Heinke, S., Thüring, A., Tegethoff, W., Köhler, J., 2017. A Spatially Resolved Fuel Cell Stack Model with Gas-Liquid Slip Phenomena for Cold Start Simulations. International Journal of Hydrogen Energy, 42:15328-15346.

Thompson, E.L., Fuss, R.L., Keeler, T.J., Lee, J.H., Raiser, S., 2005. Self-Thawing Fuel Cell. US Patent, Mar. 17, US 2005/0058865 A1.

Thompson, E.L., Jorne, J., Gu, W., Gasteiger, H.A., 2008. PEM Fuel Cell Operation at −20°C. I. Electrode and Membrane Water (Charge) Storage. Journal of The Electrochemical Society, 155(6):B625-B634.

Topcu, A., Aydın, K., Çelik, S., 2020. Experimental Investigation on the Cold Start Performance of PEM Fuel Cell. International Conference on Energy, Environment and Storage of Energy (ICEESEN), November 19-21, 26-30, Kayseri, Turkey.

Topcu, A., Aydın, K., Çelik, S., 2021a. Effect of External Heater Operating Duration on Cold Start Performance of PEM Fuel Cell. 5th International Hydrogen

Technologies Congress (IHTEC-2021), May 26-28, 252-254, Niğde, Turkey.

Topcu, A., Aydın, K., Çelik, S., 2022. The Effect of the Heater Operation Duration on the Cold Start Performance of the Coolant Heating Assisted PEM Fuel Cell Application. International Journal of Energy Research, 46(15):23939-23962.

Topcu, A., Aydın, K., Çelik, S., Yağız, M., 2021b. Coolant Selection for the Enhanced Cold Start Capability of PEM Fuel Cell. 5th International Hydrogen Technologies Congress (IHTEC-2021), May 26-28, 335-337, Niğde, Turkey.

Topcu, A., Darıcık, F., Tüccar, G., 2018. A Review on Composite Materials Usage in Bipolar Plates of Proton Exchange Membrane Fuel Cells (PEMFCs). 3rd International Conference on Vocational and Technical Sciences (UMTEB-3), June 21-22, 2999-3005, Gaziantep, Turkey.

Topcu, A., Kocamanoğlu, A.Ö., Aydın, K., Çelik, S., 2021c. Optimum Heating Method for the Assisted Cold Start Technique Of PEM Fuel Cell. 5th International Hydrogen Technologies Congress (IHTEC-2021), May 26-28, 257-259, Niğde, Turkey.

Topcu, M., Topcu, A., Aydın, K., Çelik, S., Koçak, N.F., 2019. Traditional and Innovative Manufacturing Techniques of Bipolar Plates Used in PEM Fuel Cell. Academic Perspective Procedia, 2(3):720-729.

Veser, G., 2001. Experimental and Theoretical Investigation of H_2 Oxidation in a High-Temperature Catalytic Microreactor. Chemical Engineering Science, 56:1265-1273.

Wan, Z., Chang, H., Shu, S., Wang, Y., Tang, H., 2014. A Review on Cold Start of Proton Exchange Membrane Fuel Cells. Energies, 7:3179-3203.

Wang, G., Utaka, Y., Wang, S., 2019. Planar-Distributed Wettability of Microporous Layer of Polymer Electrolyte Fuel Cell to Improve Cold Start Performance. Journal of Power Sources, 437:226930.

Wang, G.,Yu, Y., Liu, H., Gong, C., Wen, S., Wang, X., Tu, Z., 2018. Progress on Design and Development of Polymer Electrolyte Membrane Fuel Cell Systems for Vehicle Applications: A Review. Fuel Processing Technology, 179:203-228.

Wang, J., Wang, B., Tongsh, C., Miao, T., Cheng, P., Wang, Z., Du, Q., Jiao, K., 2022. Combining Proton and Anion Exchange Membrane Fuel Cells for Enhancing the Overall Performance and Self-humidification. Chemical Engineering Journal, 428:131969.

Wang, Y., Diaz, D.F.R. Chen, K.S., Wang, Z., Adroher, X.C., 2020a. Materials, Technological Status, and Fundamentals of PEM Fuel Cells – A Review. Materials Today, 32:178-203.

Wang, Y., Seo, B., Wang, B., Zamel, N., Jiao, K., Adroher, X.C., 2020b. Fundamentals, Materials, and Machine Learning of Polymer Electrolyte Membrane Fuel Cell Technology. Energy ad AI, 1:100014.

Wang, Y., Yuan, H., Martinez, A., Hong, P., Xu, H., Bockmiller, F.R., 2021. Polymer Electrolyte Membrane Fuel Cell and Hydrogen Station Networks for Automobiles: Status, Technology, and Perspectives. Advances in Applied Energy, 2, 100011:1-22.

Website, 2005. DOE 2005 Technical Team Roadmap. https://www.hydrogen.energy.gov/pdfs/progress05/vii_j_1_pivovar.pdf. [Accessed on January 14, 2023].

Website, 2010. New Energy and Industrial Technology Development Organization (NEDO), Japan. https://www.nedo.go.jp/content/100079670.pdf. [Accessed on January 14, 2023].

Website, 2014. Fuel Cell 2013 Technical Team Roadmap. https://www.energy.gov/sites/prod/files/2014/02/f8/fctt_roadmap_june2013.pdf. [Accessed on January 14, 2023].

Website, 2016a. Manufacturing cost analysis of PEM fuel cell systems for 5- and 10-kW backup power applications.

https://www.energy.gov/sites/prod/files/2016/12/f34/fcto_cost_analysis_pem_fc_5-10kw_backup_power_0.pdf. [Accessed on January 14, 2023].

Website, 2016b. MOST, China FCV Technical Roadmap. https://static1.squarespace.com/static/5b7d93fe0dbda3ea011485b9/t/5d93c88ef490cb28e94bd655/1569966226975/FCV+Tech+Roadmap_China.pdf. [Accessed on January 14, 2023].

Website, 2017. Fuel Cell 2017 Technical Team Roadmap. https://www.energy.gov/sites/prod/files/2017/11/f46/FCTT_Roadmap_Nov_2017_FINAL.pdf. [Accessed on January 14, 2023].

Website, 2021. DOE, Fuel Cell Cold Start Targets. https://www.energy.gov/eere/fuelcells/doe-technical-targets-fuel-cell-systems-and-stacks-transportation-applications. [Accessed on January 14, 2023].

Website, 2022. European Fuel Cell and Hydrogen Technology Platform (FCH JU). https://www.fch.europa.eu/sites/default/files/EGAA19001ENN_002_ONLINE%20VERSION%20%28ID%207214731%29_0.pdf. [Accessed on January 14, 2023].

Website, 2023a. Hydrogen Fuel-Cell Vehicles: Everything You Need to Know. https://www.caranddriver.com/features/a41103863/hydrogen-cars-fcev/. [Accessed on January 14, 2023].

Website, 2023b. Compare Fuel Cell Vehicles. https://www.fueleconomy.gov/feg/fcv_sbs.shtml. [Accessed on January 14, 2023].

Website, 2023c. Hydrogen Air MEA. https://www.fuelcellstore.com/fuel-cell-components/membrane-electrode-assembly/hydrogen-air-mea. [Accessed on January 14, 2023].

Website, 2023d. Physical Specifications of Ethanol. https://www.sigmaaldrich.com/TR/tr/sds/sigald/493546. [Accessed on January 25, 2023].

Website, 2023e. Physical Specifications of Methanol. https://www.sigmaaldrich.com/TR/tr/sds/mm/1.06009. [Accessed on January 25, 2023].

Website, 2023f. Physical Specifications of Ethylene Glycol. https://www.sigmaaldrich.com/TR/tr/sds/sial/85978. [Accessed on January 25, 2023].

Website, 2023g. Physical Specifications of Propylene Glycol. https://www.sigmaaldrich.com/TR/tr/sds/usp/1576708. [Accessed on January 25, 2023].

Website, 2023h. Ethanol – Water Solution Specifications. https://www.engineeringtoolbox.com/ethanol-water-d_989.html. [Accessed on January 26, 2023].

Website, 2023i. Methanol – Water Solution Specifications. https://www.engineeringtoolbox.com/methanol-water-d_987.html. [Accessed on January 26, 2023].

Website, 2023j. Ethylene Glycol – Water Solution Specifications. https://www.engineeringtoolbox.com/ethylene-glycol-d_146.html. [Accessed on January 26, 2023].

Website, 2023k. Propylene Glycol – Water Solution Specifications. https://www.engineeringtoolbox.com/propylene-glycol-d_363.html. [Accessed on January 26, 2023].

Wei, L., Liao, Z., Suo, Z., Chen, X., Jiang, F., 2019. Numerical Study of Cold Start Performance of Proton Exchange Membrane Fuel Cell With Coolant Circulation. International Journal of Hydrogen Energy, 44:22160-22172.

Wheat, W.S., Meltser, M.A., Masten, D.A., 2004. Fuel Cell Energy Management System for Cold Environments. US Patent, Apr. 27, US 6 727 013 B2.

Wilkinson, D.P., St.-Pierre, J., Roberts, J.A., Campbell, S.A., 2001. Method of Reducing Fuel Cell Performance Degradation of an Electrode Comprising Porous Components, U.S. Patent, Oct. 23, US 6 306 536 B1.

Xie, X., Wang, R., Jiao, K., Zhang, G., Zhou, J., Du, Q., 2018. Investigation of the Effect of Micro-Porous Layer on PEM Fuel Cell Cold Start Operation. Renewable Energy, 117:125-134.

Xu, J., Zhang, C., Wan, Z., Chen, X., Chan, S.H., Tu, Z., 2022. Progress and Perspectives of Integrated Thermal Management Systems in PEM Fuel Cell Vehicles: A Review. Renewable and Sustainable Energy Reviews, 155, 111908:1-23.

Xu, P., Xu, S., 2018. A Progress Review on Gas Purge for Enhancing Cold Start Performance in PEM Fuel Cell. SAE Technical Paper, 1-17.

Yang, Y., Ma, T., Du, B., Lin, W., Yao, N., 2021. Investigation on the Operating Conditions of Proton Exchange Membrane Fuel Cell Based on Constant Voltage Cold Start Mode. Energies, 14, 660.

Yang, Z., Jiao, K., Wu, K., Shi, W., Jiang, S., Zhang, L., Du, Q., 2021. Numerical Investigations of Assisted Heating Cold Start Strategies for Proton Exchange Membrane Fuel Cell Systems. Energy, 222:e119910.

Yue, L., Wang, S., Zhu, Y., Fan, Y., 2022. Experimental Study on Cold Start Performance of PEMFC Based on Parallel Flow Channels. International Journal of Hydrogen Energy, 47:540-550.

Zakaria, I., Michael, Z., Mohamed, W.A.N.W., Mamat, A.M.I., Azmi, W.H., Mamat, R., Saidur, R., 2015. A Review of Nanofluid Adoption in Polymer Electrolyte Membrane (PEM) Fuel Cells as an Alternative Coolant. Journal of Mechanical Engineering and Sciences, 8:1351-1366.

Zhan, Z., Yuan, C., Hu, Z., Wang, H., Sui, P.C., Djilali, N., Pan, M., 2018. Experimental Study on Different Preheating Methods for the Cold-Start of PEMFC Stacks. Energy, 162:1029-1040.

Zhang, G., Kandlikar, S.G., 2012. A Critical Review of Cooling Techniques in Proton Exchange Membrane Fuel Cell Stacks. International Journal of Hydrogen Energy, 37:2412-2429.

Zhong, D., Rui, L., Han, L., Xu, J., Wang, H., Liu, S., Ji, W., Cai, X., 2021. Mechanism Analysis of the Effect of Different Gas Manifold Positions on Proton Exchange Membrane Fuel Cell Cold Start Performance. International Journal of Energy Research, 45(9):13429-13441.

Zhou, Y., Luo, Y., Yu, S., Jiao, K., 2014. Modeling of Cold Start Processes and Performance Optimization for Proton Exchange Membrane Fuel Cell Stacks. Journal of Power Sources, 247:738-748.

Zhu, M., Xie, X., Wu, K. Najmi, A-U-H., Jiao, K., 2019a. Experimental Investigation of the Effect of Membrane Water Content on PEM Fuel Cell Cold Start. Energy Procedia, 158:1724-1729.

Zhu, Y., Lin, R., Han, L., Jiang, Z., Zhong, D., 2021. Investigation on Cold Start of Polymer Electrolyte Membrane Fuel Cells Stacks with Diverse Cathode Flow Fields. International Journal of Hydrogen Energy, 46:5580-5592.

Zhu, Y., Lin, R., Jiang, Z., Zhong, D., Wang, B., Shangguan, W., Han, L., 2019b. Investigation on Cold Start of Polymer Electrolyte Membrane Fuel Cells with Different Cathode Serpentine Flow Fields. International Journal of Hydrogen Energy, 44:7505-7517.

CURRICULUM VITAE

Alparslan Topcu.. He received his BSc. degree from the Mechanical Engineering Department of Hitit University in 2014, and his MSc. Degree from Karadeniz Technical University in 2017, respectively. His main interest areas are PEM fuel cells, solid oxide fuel cells, and additive manufacturing (AM) technologies. His special research areas are also heat transfer, cold start techniques for PEM fuel cells, interconnect manufacturing techniques for SOFCs, performance evaluations for fuel cells, powder metallurgy (P/M), and plastic, polymer, and metal-based AM fabrication methods. He worked as a research assistant in the Mechanical Engineering Department of the Adana Alparslan Türkeş Science and Technology University between 2017-2021 years. He has been working as an instructor (lecturer) in the Mechanical Engineering Department of Alanya Alaaddin Keykubat University. He is married and has two children.

APPENDIX

A.1. MATLAB CODE FOR THE VISUALIZATION

```
clc,clear all
D=xlsread('matlabdata');
t=input ('second=')
m=50*t+1;
x=[1  3  5];
y=[D(m,3)                    D(m,4)+(abs(D(m,4)-D(m,4)))/24
D(m,5)+2*((D(m,3)-D(m,2))/3)];
n=length(x)-1;
h=0.1;
xp1=1:h:5
sm1=0;
for i=1:n+1
    pr=1;
    for j=1:n+1
        if j~=i
            pr=pr.*(xp1-x(j))./(x(i)-x(j));
        end
    end
    sm1=sm1+y(i).*pr;
end
yp1=sm1;
x=[1  2  5];
y=[(D(m,4)+D(m,3))/2      D(m,4)    D(m,3)+2*abs((D(m,3)-
D(m,5))/3)];
n=length(x)-1;
h=0.1;
xp2=1:h:5;
sm2=0;
```

```
for i=1:n+1
    pr=1;
    for j=1:n+1
        if j~=i
            pr=pr.*(xp2-x(j))./(x(i)-x(j));
        end
    end
    sm2=sm2+y(i).*pr;
end
yp2=sm2;
x=[1  3  5];
y=[(D(m,3)+D(m,4)+D(m,5)+D(m,6))/4                D(m,5)
(D(m,4)+D(m,5))/2];
n=length(x)-1;
h=0.1;
xp3=1:h:5;
sm3=0;
for i=1:n+1
    pr=1;
    for j=1:n+1
        if j~=i
            pr=pr.*(xp3-x(j))./(x(i)-x(j));
        end
    end
    sm3=sm3+y(i).*pr;
end
yp3=sm3;
x=[1  4  5];
y=[(D(m,4)+D(m,5)+D(m,6))/3  D(m,6)  (D(m,6)+D(m,7))/2];
```

```
n=length(x)-1;
h=0.1;
xp4=1:h:5;
sm4=0;
for i=1:n+1
    pr=1;
    for j=1:n+1
        if j~=i
            pr=pr.*(xp4-x(j))./(x(i)-x(j));
        end
    end
    sm4=sm4+y(i).*pr;
end
yp4=sm4;
x=[1  3  5];
y=[(D(m,5)+D(m,6))/2  (D(m,7)+D(m,5))/2  D(m,7)];
n=length(x)-1;
h=0.1;
xp5=1:h:5;
sm5=0;
for i=1:n+1
    pr=1;
    for j=1:n+1
        if j~=i
            pr=pr.*(xp5-x(j))./(x(i)-x(j));
        end
    end
    sm5=sm5+y(i).*pr;
end
```

```
yp5=sm5;
xboy=1:5;
yboy=linspace(1,5,41);
sm=[sm1;sm2;sm3;sm4;sm5];
subplot(1,1,1),pcolor(yboy,xboy,sm),shading
interp,colorbar,caxis([-30 30]);
colormap(jet)
set(gca, 'YTick', 0:5)
set(gca, 'XTick', 0:5)
```

A.2. PUBLISHED ARTICLES IN SCI JOURNALS

Topcu, A., Aydın, K., Çelik, S., 2022. The Effect of the Heater Operation Duration on the Cold Start Performance of the Coolant Heating Assisted PEM Fuel Cell Application. International Journal of Energy Research, 46(15), 23939-23962. http://doi.org/10.1002/er.8692 .

Darıcık, F., Topcu, A., Aydın, K., Çelik, S., 2023. Carbon Nanotube (CNT) Modified Carbon Fiber/Epoxy Composite Plates for the PEM Fuel Cell Bipolar Plate Application. International Journal of Hydrogen Energy, 48(3), 1090-1106. https://doi.org/10.1016/j.ijhydene.2022.09.297.

Topcu, A., Aydın, K., Çelik, S., Kocamanoğlu, A.Ö., Experimental Investigation on the Heating Mechanism of the PEM Fuel Cell Assisted Cold Start Method. *Fuel Cells, Under Review*.

Topcu, A., Aydın, K., Çelik, S., Yağız, M., Optimum Coolant Selection for the Rapid Cold Start of PEM Fuel Cells. *Preparing for Publication*.

Topcu, A., Aydın, K., Çelik, S., Alternating Improvements for the Cold Start Capability of the PEM Fuel Cells: Experimental Investigation on the Start-up of the Frozen MEA. *Preparing for Publication*.

Topcu, A., Aydın, K., Çelik, S., The Effect of Starter Modes on the Cold Start Performance of the Coolant Heating Assisted PEMFC Operation. *Preparing for Publication*.

Topcu, A., Aydın, K., Çelik, S. Experimental Investigation Techniques on Cold Start of PEM Fuel Cells: A Review. *Renewable & Sustainable Energy Reviews, Under Review*.

A.3. INTERNATIONAL CONFERENCE PAPERS

Topcu, A., Aydın, K., Çelik, S., 2021. Harici Isıtma Sistemi Sıcaklığının PEM Yakıt Pili Soğuk Çalıştırma Performansına Etkisi. *6th International Mediterranean Science and Engineering Congress* (IMSEC 2021), October 25-27, 217, Alanya, Antalya, Turkey.

Topcu, A., Aydın, K., Çelik, S., 2021. PEM Yakıt Pili Soğuk Çalıştırma Prosesi için Yardımlı ve Yardımsız Başlatma Teknikleri. *6th International Mediterranean Science and Engineering Congress* (IMSEC 2021), October 25-27, 287, Alanya, Antalya, Turkey.

Topcu, A., Kocamanoğlu, A.Ö., Aydın, K., Çelik, S., 2021. Optimum Heating Method for the Assisted Cold Start Technique of PEM Fuel Cell. *5th International Hydrogen Technologies Congress* (IHTEC-2021), May 26-28, 257-259, Niğde, Turkey.

Topcu, A., Aydın, K., Çelik, S., 2021. Effect of External Heater Operating Duration on Cold Start Performance of PEM Fuel Cell. *5th International Hydrogen Technologies Congress* (IHTEC-2021), May 26-28, 252-254, Niğde, Turkey.

Topcu, A., Aydın, K., Çelik, S., Yağız, M., 2021. Coolant Selection for the Enhanced Cold Start Capability of PEM Fuel Cell. *5th International Hydrogen Technologies Congress* (IHTEC-2021), May 26-28, 335-337, Niğde, Turkey.

Topcu, A., Darıcık, F., Aydın, K., Çelik, S., 2021. Electrical Properties of the Carbon Nanotube (CNT) Reinforced Composite Plates for the PEM Fuel Cell Bipolar Plate Application. *5th International Hydrogen Technologies Congress* (IHTEC-2021), May 26-28, 221-223, Niğde, Turkey.

Topcu, A., Aydın, K., Çelik, S., 2020. Experimental Investigation on the Cold Start Performance of PEM Fuel Cell. *International Conference on Energy,*

Environment and Storage of Energy (ICEESEN), November 19-21, 26-30, Kayseri, Turkey.

Koçak, N.F., Topcu, A., Aydın, K., Çelik, S., Topcu, M., 2019. Bipolar Plaka Akış Alanları Üzerine Deneysel Çalışmalar. *7th International Symposium on Innovative Technologies in Engineering and Science* (ISITES2019), November 22-24, Şanlıurfa, Turkey.

Topcu, M., Topcu, A., Aydın, K., Çelik, S., Koçak, N.F., 2019. PEM Yakıt Pili Bipolar Plakalarının Geleneksel ve Yenilikçi Üretim Teknikleri. *7th International Symposium on Innovative Technologies in Engineering and Science* (ISITES2019), November 22-24, Şanlıurfa, Turkey.

Darıcık, F., Topcu, A., Tüccar, G., Aydın, K., 2019. Effects of Fibre Orientations and Flow Channel Patterns on the Durability of Composite Bipolar Plates Used in PEMFCs. *The 8th International Conference on Modeling, Simulation and Applied Optimization* (ICMSAO'2019), April 15-17, 1-5, Manama, Bahrain.

Topcu, A., Aydın, K., Çelik, S., 2019. Evaluation of Methanol at Start-Up for the PEMFC Cold Start Process. *4th International Hydrogen Technologies Congress* (IHTEC2019), June 20-23, 40-41, Edirne, Turkey.

Topcu, A., Darıcık, F., Tüccar, G., 2018. A Review on Composite Materials Usage in Bipolar Plates of Proton Exchange Membrane Fuel Cells (PEMFCs). *3rd International Congress on Vocational and Technical Sciences* (UMTEB-3), June 21-22, 2999-3005, Gaziantep, Turkey.

Topcu, A., Darıcık, F., Tüccar, G., Aydın, K., 2018. Numerical Study on Improvement of Parallel (Straight) Flow Field Used in Fuel Cells. *3rd International Congress on Vocational and Technical Sciences* (UMTEB-3), June 21-22, 2018, 2993-2998, Gaziantep, Turkey.